Characterization of physico-chemical environment of Co-based multilayer mirrors working in the soft x-ray and EUV ranges

Yanyan Yuan

To cite this version:

Yanyan Yuan. Characterization of physico-chemical environment of Co-based multilayer mirrors working in the soft x-ray and EUV ranges. Chemical Physics [physics.chem-ph]. Université Pierre et Marie Curie - Paris VI, 2014. English. NNT : 2014PA066444 . tel-01080753v2

HAL Id: tel-01080753
https://theses.hal.science/tel-01080753v2

Submitted on 7 Mar 2015

Université Pierre et Marie Curie

Ecole doctorale 388

Laboratoire de Chimie-Physique-Matière et Rayonnement

Characterization of physico-chemical environment of Co-based multilayer mirrors working in the soft x-ray and EUV ranges

Par Yanyan YUAN

Thèse de doctorat de Chimie Physique et Chimie Analytique

Dirigée par Philippe Jonnard

Présentée et soutenue publiquement le 02 octobre 2014

Devant un jury composé de :

Dr. Franck Delmotte	**Rapporteur**
Pr. Wanqi Jie	**Rapporteur**
Pr. Jean-Michel Mariot	**Examinateur**
Dr. Claude Merlet	**Examinateur**
Dr. Emmanuel Nolot	**Examinateur**

Dr. Philippe Jonnard (director of thesis)

Acknowledgements

Time always goes by so fast. Three years have passed since I came to Paris. I am very grateful to many peoples who helped me a lot during my doctoral research life and who made pleasant my stay in Paris.

I firstly would like to give my sincere thanks to Alain Dubois, director of our lab LCPMR (Laboratoire de Chimie Physique - Matière et Rayonnement), who accepted me warmly in the laboratory. I am also very grateful for his help in my daily life.

I am very thankful to my supervisor Philippe Jonnard who helped me many things not only in research but also in my daily life. His patience and encouragement always give me confidence during my work. He always corrects very carefully and efficiently everything I wrote during my Ph.D. work, gives advices and makes useful comments. He taught me the ability to do independent the research. I am very happy and lucky to work with him not only for his kind teaching but also for his wide range of knowledge. I give him all my deepest respect and gratitude.

I would particularly like to give my gratitude to Karine Le Guen, my other supervisor, who gave me great help for treating data and who corrects carefully the manuscript. Her kindness and seriousness at work affect me a lot.

I would particularly like to thank Jean-Michel André who made me a lot of useful suggestions. His encouragement and humor always convey me the message that nothing is difficult.

I would like to thank all the people who collaborate with our team. Without them I could not able to obtain so fruitful results and finish my thesis on time. I thank warmly Zhanshan Wang and Jingtao Zhu, the IPOE (Institute of Precision Optical Engineering, Tongji Univeristy, China) for the samples and the important suggestions for the study of Co-based multilayers.

I would like to express my thanks to Christian Mény, from the IPCMS (Institut de Physique et Chimie des Matériaux de Strasbourg), who helped us to do the NMR experiments. He made many useful suggestions and interesting discussion. I also give my special thanks to Corinne Ulhaq, from the IPMCS, for her help doing the TEM experiments and for useful and fruitful discussions.

I would like to thank Imène Esteve, from the IMPMC (Insitut de Minéralogie et de Physique des Milieux Condensés, UPMC), who helped us to prepare many FIB samples.

I would like to thank Angelo Giglia, Nicola Mahne and Stefano Nannarone, from the

BEAR beamline at the ELETTRA synchrotron radiation facility (Trieste Italy) for the help doing the experiments and the data analysis, and for the useful discussions.

I am grateful to my previous supervisor Wanqi Jie, from the Northwest Polytechinical University in China, who recommended me to the LCPMR. This opportunity is an important turning point in my life. I also would like to thank him for accepting my PhD work report.

I would like to give my thanks to all the members of the committee for the critical reading of manuscript. M. Claude Merlet, M. Emmanuel Nolot, M. Franck Delmotte, M. Jean-Michel Mariot.

Thanks also to all the members of our Lab, LCPMR who give the friendly study environment. I specially thank: Anzar, Ahmed, Bharati, Cédric, Grégory, Jonathan, Nicolas, Rajash, Selma, Tatiana, Yuchun, ... All of them gave me great help in my life and make me have colorful life in Paris.

I give my great thanks to my family, especially my parents who always give me great supports and confidence. I also thank my husband Shaofeng Zhang who gives me all his love.

Contents

Chapter 1 Multilayer mirrors in the soft x-ray and extreme ultraviolet ranges

Multilayer mirrors consisting of two materials with high and low atomic numbers are studied since a long time. They are used in space telescopes, x-ray microscopes, extreme ultraviolet (EUV) photolithography, synchrotron radiation beamlines, electron microprobes and so on. The physico-chemical environment of the multilayer interfaces plays an important role in the optical applications. Interdiffusion and formation of compounds at the interfaces could degrade the optical performance of multilayer mirrors. Therefore in this thesis we study the optical performance and interface properties of Co-based multilayers upon annealing by combining non-destructive and destructive methods.

1.1 Soft x-ray and extreme ultraviolet light

X-rays are invisible by human eyes and have shorter wavelength (higher energy) than visible light. Figure 1.1 shows the portion of the electromagnetic spectrum extending from the infrared to the x-ray region. The EUV extends from the photon energy of about 30 eV to about 250 eV; the soft x-rays range extends from the about 250 to several keV. These spectral regions cover the main atomic absorption edges of some low and intermediate atomic number elements. For example, the C K, O K, Co L, Si K edges are located in the EUV and soft x-ray ranges. This makes the x-rays a sensitive tool for elemental and chemical identification.

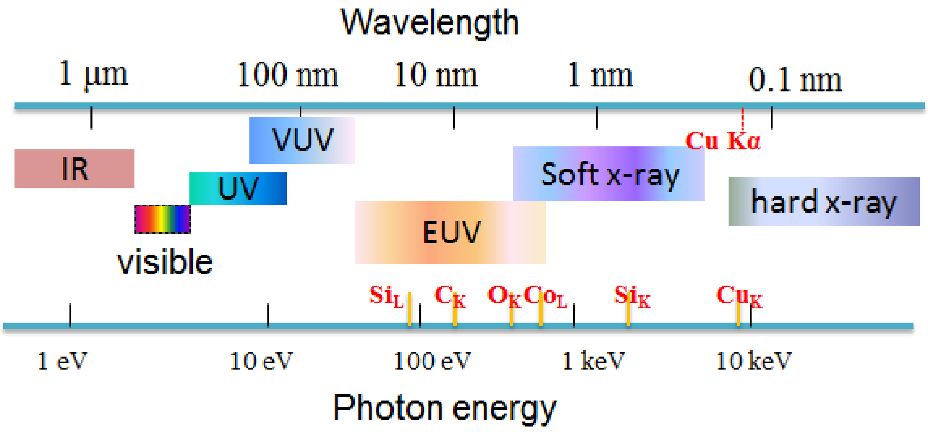

Figure 1.1 Electromagnetic spectrum from the infrared to the x-ray region.

Soft x-ray and EUV rays, owing to their short wavelength, can be used to see small structures as in optical microscopy and also to write smaller patterns as in photolithography. Light sources such as synchrotron radiation facilities and free electron lasers are high brightness source. However this in turn requires high quality optics to develop their beamlines.

1.2 Multilayer mirrors

In the soft x-ray and EUV ranges, the refractive index of all the materials is close to one; all the materials have very low reflectivity excepting at very grazing angle (total external reflection). For example, at the wavelength of 30 nm the reflectivity of a single layer at normal incidence is the order of 10^{-2} and it decreases rapidly at shorter wavelengths. In order to manipulate soft x-ray and EUV light, we need to use special optical elements. Conventional optical elements, such as lenses or single thin layer coated mirrors (single reflection), cannot meet the requirement of the high reflectivity at normal incidence. An exception for achieving high reflectivity is the total external reflection of the x-rays at very grazing incident angle. But the shortcoming of these optics is their low luminosity. Otherwise their application is limited in the range of short wavelengths.

A multilayer mirror can provide high reflectivity based on the diffraction principle. It can be described as an analogy of single crystal. The multilayer mirror can meet the requirements of some application wavelength in the soft x-ray and EUV ranges by adjusting the period thickness. Figure 1.2 shows a scheme of a multilayer mirror. It is a periodic stack of layers consisting of at least two alternating materials, in which one material has a high atomic number as an absorber and the other has low atomic number as a spacer. Multilayer mirror reflectivity derives from the interference of x-rays coherently scattered from the interfaces between the constituent materials. In this structure, the incident beam is reflected at interface, while the rest penetrates deeper into the stack and is partly reflected at other interfaces. All partly reflected coherent beams interfere with each other. If for example at normal incidence the optical thickness (the product of the refractive index and the geometrical thickness) of all the layers, when not taking into account the absorption, is exactly equal to a quarter of the wavelength of the incoming light ("quarter-wave stack"), all the beams add up constructively and a high reflectivity can be obtained.

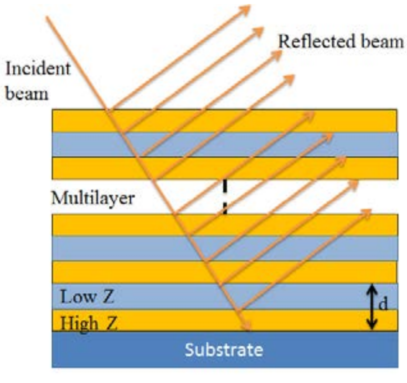

Figure 1.2 Scheme of a multilayer mirror.

1.2.1 Theory and principle of multilayer mirrors

In our research we used the IMD computer software to simulate the reflectivity [1]. This computer program is based on the Fresnel equations for calculating the optical functions of a multilayer film. It can be used for modelling the optical properties (reflectivity, transmittance, absorptance and electric field intensities, etc.) of multilayer films.

Firstly we take an idealized interface as an example, *i.e.*, the interface between two semi-infinite media is abrupt, as shown in Figure 1.3. An electromagnetic plane wave propagates at this idealized interface. The complex refraction index $\boldsymbol{n} = n - ik$ (where n is the refractive index and k is the absorption component) is given in the two regions as $\boldsymbol{n}_i$ and $\boldsymbol{n}_j$. The incident wave vector $\overrightarrow{k_i}$, with electric field amplitude $\mathbf{E}_i$, makes an angle θ_i with respect to the sample surface. The amplitude of the reflected and transmitted electric fields, $\boldsymbol{E}_i^r$ and $\boldsymbol{E}_j^t$, respectively, are given by the Fresnel equations giving r_{ij} and t_{ij} the Fresnel reflection and transmission coefficients respectivley:

$$\frac{|\boldsymbol{E}_i^r|}{|\boldsymbol{E}_i|} = \frac{\boldsymbol{n}_i \sin\theta_i - \boldsymbol{n}_i \cos\theta_j^t}{\boldsymbol{n}_i \sin\theta_i + \boldsymbol{n}_j \cos\theta_j^t} = r_{ij}^s, \tag{1.1a}$$

and

$$\frac{|\boldsymbol{E}_j^t|}{|\boldsymbol{E}_i|} = \frac{2\boldsymbol{n}_i \sin\theta_i}{\boldsymbol{n}_i \sin\theta_i + \boldsymbol{n}_j \cos\theta_j^t} = t_{ij}^s, \tag{1.1b}$$

for *s*-polarization where electric field E is perpendicular to the plane of incidence;

$$\frac{|\boldsymbol{E}_i^r|}{|\boldsymbol{E}_i|} = \frac{\boldsymbol{n}_i \cos\theta_j^t - \boldsymbol{n}_j \sin\theta_i}{\boldsymbol{n}_i \cos\theta_j^t + \boldsymbol{n}_j \sin\theta_i} = r_{ij}^p, \tag{1.2a}$$

and

$$\frac{|\boldsymbol{E}_j^t|}{|\boldsymbol{E}_i|} = \frac{2\boldsymbol{n}_i \sin\theta_i}{\boldsymbol{n}_i \cos\theta_j^t + \boldsymbol{n}_j \sin\theta_i} = t_{ij}^p, \tag{1.2b}$$

for *p*-polarization where electric field E is parallel to the plane of incidence.

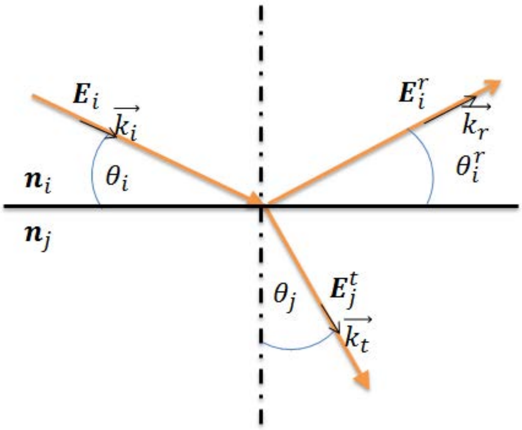

Figure 1.3 Diagram of a plane wave incident at the interface between two materials with different refractive indices.

We now consider a plane wave incident on a multilayer stack with a period thickness of *d*. There is a series of *N* layers (*N*+1 interfaces), where the *i*th layer has thickness d_i, optical constant $\boldsymbol{n}_i$, as shown in Figure 1.4. The vacuum and the substrate have the optical constants $\boldsymbol{n}_a$ and $\boldsymbol{n}_s$, respectively.

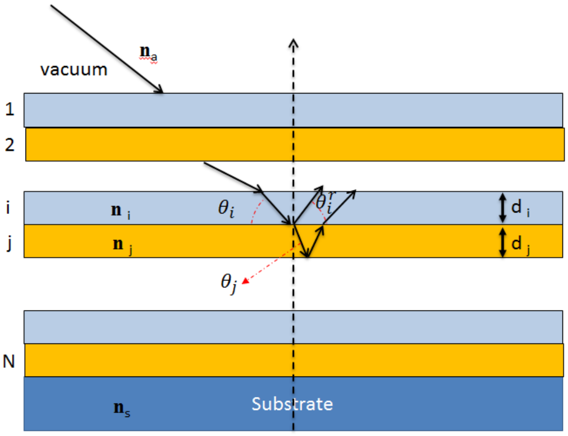

Figure 1.4 Diagram of a multilayer stack with period thickness of d containing N layers, where the optical constants, the thickness and the propagation angles of the ith layer are $\boldsymbol{n_i}$, $\boldsymbol{d_i}$, and $\boldsymbol{\theta_i}$, respectively. The ambient (*i.e.*, the region above the film) has optical constants $\boldsymbol{n_a}$ and the substrate has optical constants $\boldsymbol{n_s}$.

The net reflection r_i and transmission coefficient t_i of the *i*th layer are given by:

$$r_i = \frac{r_{ij}+r_j e^{2i\beta_i}}{1+r_{ij}r_j e^{2i\beta_i}}, \tag{1.3a}$$

$$t_i = \frac{t_{ij}t_j\, e^{2i\beta_i}}{1+r_{ij}r_j e^{2i\beta_i}}, \tag{1.3b}$$

where $\beta_i = 2\pi d_i \boldsymbol{n}_i \sin\theta_i / \lambda$, and r_{ij} and t_{ij} are given by the equations (1.1) and (1.2). Thus, the procedure to compute the net reflection (r) and transmission (t) coefficients for the multilayer stack is to use equations (1.3) recursively, starting at the bottom-most layer, *i.e.*, i=N, j=s. The reflectivity R for the whole multilayer structure is given by:

$$R = |r_1|^2 \tag{1.4}$$

In the simulation, interface imperfections (interdiffusion and interface roughness) can be taken into account. Interface quality of multilayers is an important factor for the optical performance of multilayer mirrors.

Here we give one example: the reflectivity of a Co/Mo_2C multilayer with 30 bilayers of 4.10 nm period thickness, which will be studied in this thesis. We suppose that the interfaces between layers are ideal, *i.e.* no interdiffusion and interlayers. The roughness of the substrate is assumed to be 0.50 nm. The calculated reflectivity as a function of grazing angle with *s*-polarization at the wavelength of 1.59 nm is shown in Figure 1.5. As we can see the value of reflectivity is about 45% at the grazing angle of 11°. In addition we can also make simulation of the reflectivity as a function of photon energy, parameters of each layer and period.

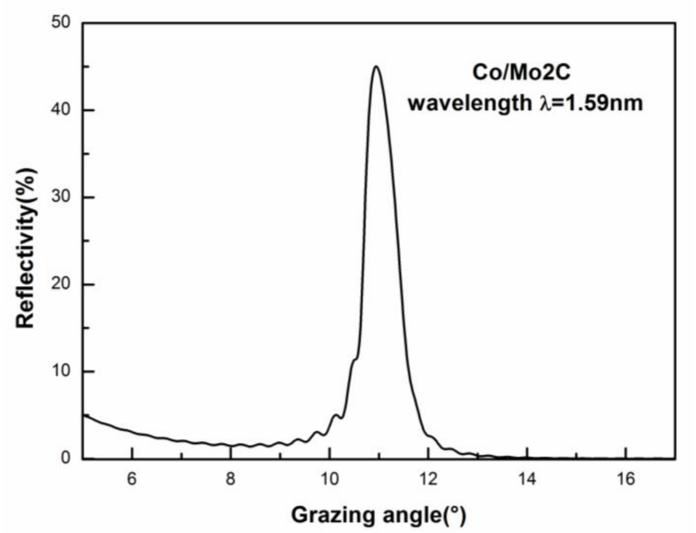

Figure 1.5 Calculated reflectivity of a Co/Mo_2C multilayer with s-polarization at the wavelength of 1.59 nm.

1.2.2 Design of multilayer mirrors for the soft x-ray and EUV ranges

In multilayer mirrors, if we neglect the refraction effect, maximum of reflectivity occurs when its period d satisfies the general Bragg law:

$$2d \sin \theta = p\lambda \tag{1.5}$$

where p is an integer, λ the wavelength of incidence beam, d the period thickness within the multilayer, θ the angle between the incident beam and sample surface. In order to achieve high reflectivity of a multilayer mirror in the soft x-ray and EUV ranges, the selection of materials and matching of material pairs in one period is critical. In the case of normal incidence, the thickness of the individual layers should be equal to half of the period thickness without taking into account absorption. When taking into account the absorption, the thickness of the most absorbing layer should be reduced to improve the reflectivity in the premise of keeping the period thickness constant.

In 1972, Spiller built a multilayer structure which consisted of two materials with different refractive indices, in which one is the spacer and one is the absorber [2]. The basic design idea is to locate the stronger absorber in very thin layers into the nodes of desired wave field which is generated within the periodic structure and fill the remaining space with a material with very low absorption. A reasonable reflectivity higher than 25% was obtained in the range 5-50 nm. Since then a lot of research works have been done for the design and improvement of reflectivity of multilayer mirrors. In 1992, Yamamoto *et al.* reported an optical criterion for selecting a proper pair of materials for designing a multilayer with high reflectivity [3]. This method can provide an effective means for attaining the absolute maximum reflectance on a layer-by-layer basis and also give clear insight into the evolution of the amplitude reflectance of a multilayer. In 2001, Larruquert proposed a general theory of sub-quaterwave multilayers for more than two materials with highly absorbing materials to improve the reflectance of the multilayer mirror [4]. His theory provides an accurate approach for designing a new concept of multilayer mirrors with more than two materials. Since then, the design theory for multilayer in the soft x-ray and EUV has been developed by Larruquert [5–10].

The multilayer mirrors can meet the requirements of the different application wavelengths by adjusting the period thickness. In designing multilayer mirrors an important parameter is the ratio Γ of high Z (atomic number) material thickness d_H to the total period $d = d_H + d_L$, d_L is the thickness of the low Z material.

$$\Gamma = \frac{d_H}{d_H + d_L} \tag{1.6}$$

In general the best case is when the low Z material acts simply as a “spacer”, with as little absorption as possible. In fact, the optical constants of the low Z material should be as small as possible to provide the greatest refractive index contrast with respect to that of high Z material. To obtain strong enough scattering, we can minimize the absorption by reducing the thickness of the high Z layer to have the large optical contrast. Vinogradov has found, for normal incidence, an optimized value Γ_{opt} given by [11]

$$\tan(\pi\Gamma_{opt}) = \pi\left[\Gamma_{opt} + \frac{k_L}{k_H - k_L}\right] \tag{1.7}$$

where k_L and k_H represent the absorptive components of refractive index for the low (L) Z and high (H) Z materials, respectively.

1.3 Applications of multilayer mirrors

Multilayer mirrors have the great advantage of being adaptable to curved surfaces, enabling their use as reflective optics in soft x-ray and EUV microscopes and telescopes. In addition they provide a modest well-defined spectral bandpass with a relatively high throughput, which open up many additional applications. Mo/Si multilayers, as a widely studied structure, have been used successfully in a number of satellite instruments [12,13] over the past years to provide high reflectance in the 13-30 nm wavelength range. In the following we will give some examples of application of multilayer mirror in scientific research and industry.

1.3.1 Astronomical observation with multilayer mirrors

Multilayer mirrors working at normal incidence have been used to obtain high-resolution astronomical images. The images of the Sun and the solar corona obtained at nominal 17.3 nm wavelength are presented in Fig 1.6 (a) and (b). They were obtained using a rocket-launched Cassegrain telescope with Mo/Si-coated mirrors [14,15] and Mo_2C/Si multilayer mirrors. The advantages of multilayer mirrors for solar observations are summarized as follows: (1) compared to grazing incidence optics, normal incidence multilayer mirrors have lower scattering, suffer less from geometrical aberrations, are less expensive to fabricate and easier to mount and align, and can be made more compact. Consequently, it is possible to approach the resolution limit imposed by diffraction for such systems. The combination of filled apertures and high reflection efficiencies provides high sensitivity optical systems in a compact package. (2) The compact nature and the low cost of multilayer telescopes capable of high resolution observation permit the use of multiple telescope and therefore the observation of plasma over a broad range of temperatures, even in a compact rocket borne instrument package. (3) The spectral resolving capability of multilayer mirrors is a powerful analytical tool [16]. Hence the multilayer mirrors provide a powerful diagnostic tool capable of achieving high spatial resolution, broad wavelength coverage, and moderate spectral resolution.

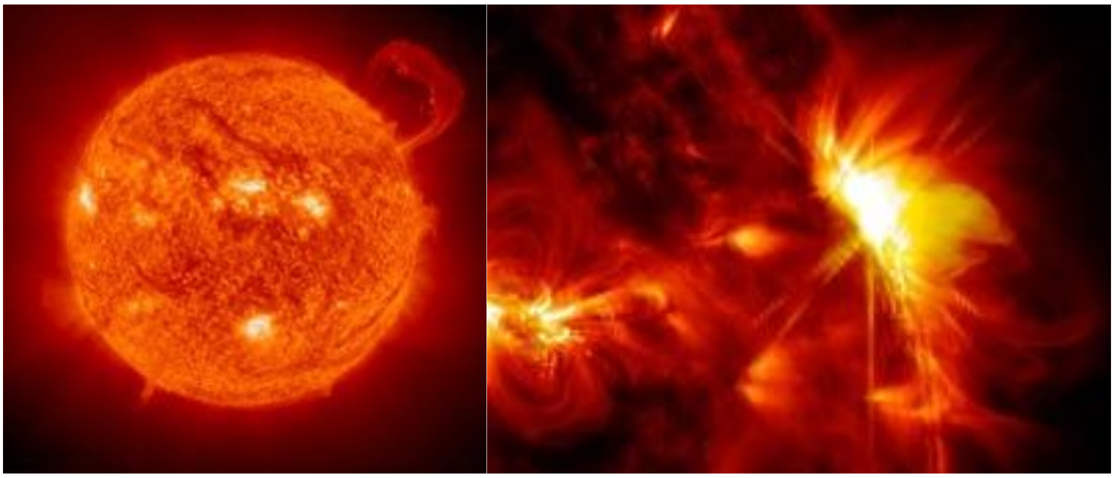

(a) (b)

Figure 1.6 EUV images of the Sun (a) and of solar flare (b) at the wavelength of 30.4 nm.

1.3.2 Extreme ultraviolet lithography

Lithography is a technique widely used in the semiconductor industry to copy patterns for manufacturing processors and memory devices for modern computing systems. Photolithography systems have progressed from blue wavelengths (436 nm) to UV (365 nm) to deep-UV (248 nm) to today's mainstream high-resolution wavelength of 193 nm. The appearance of multilayer mirrors provides the capability of decreasing the critical dimension in high volume manufacturing. The advantage of EUV is the continuation of optical techniques at a significantly reduced wavelength, permitting the achievement of small feature size with modest numerical aperture and large depth of focus. Up to now the wavelength in 13.5 nm is realized by the Mo/Si multilayers which have obtained the reflectivity of order 70% [17].

1.3.3 Photoemission microscope

A photoemission microscope is a valuable tool, which combines high spectral and spatial resolutions, to measure surface composition, including elemental concentration and chemical bonding of heterogeneous surfaces. In a photoemission microscope equipped with a multilayer mirror, the emission of photoelectrons is caused by focusing photons of specified energy onto a sample. This kind of multilayer optical system is known as a Schwarzschild objective [18]. The Mo/Si (photoemission at 91.8 eV) and Ru/B_4C [19] (photoemission at 130 eV) multilayer mirrors have already been employed.

1.3.4 X-ray standing wave

An x-ray standing wave (XSW) is formed by the superposition of two coherent plane waves. The XSW technique is in essence an x-ray interference technique. Within the wave field, x-ray intensity is spatially modulated. Knowing the exact pattern and position of an x-ray interference field and being able to manipulate it in space, information about the real space distribution of inelastically scattering objects can be obtained. In the case of atomic distributions, which are the most important application of the XSW technique, the photo-absorption or subsequent decay channels (such as photoelectrons, Auger electrons, and x-ray fluorescence) serve as marker signals upon shifting the wave field in space. A strong signal indicates that the maxima of the wave field are on atomic positions in the crystal [20].

Based on the above description, the XSW is becoming a potential technique for studying the buried nanometre scale interfaces as it is non-destructive. It can be used to determine the position of impurity atoms within a single crystal or adsorbed onto a crystal surface. The conventional method for generating XSW is to use dynamical Bragg diffraction from perfect crystals. This technique has proven to be very accurate in determining the distance separating adsorbate atoms from the surface-bulk-lattice atoms. However, the XSW, generated by the reflection of an x-ray beam from a periodic multilayer, can be used to accurately locate a layer of heavy atoms embedded in a low-Z thin film, which is deposited on the periodic multilayer [21]. Yang *et al.* have studied the Fe/Cr interfaces deposited on the top of a B_4C/W multilayer by using the XSW generated by the B_4C/W multilayer. They pointed out that this standing wave-plus-wedge would have a range of applications for the characterization of nanostructures and their interfaces [22].

In this thesis, we will present XSW results on the Co-based multilayers. We will study the first buried layer and interface properties of the Co/Mo_2C multilayers by using x-ray fluorescence and photoelectron and fluorescence spectroscopies respectively.

1.3.5 Other applications

Now the multilayer mirrors are used in the synchrotron radiation and free electron laser beam beamlines. They are exposed in vacuum to high-intensity extreme ultraviolet or soft x-ray radiation. In particular the development of free electron lasers puts forward to the high requirement for multilayer optics. High power load can induce interdiffusion at the interfaces and degrade the optical performance of multilayer mirrors. The stability of sharp interfaces upon time is vital for maintaining the reflectivity. This will be described in the

Section 1.5. Furthermore, other applications (plasma diagnostic, polarization studies of magnetic materials, x-ray microprobe) can be realized by the development of multilayer optics.

1.4 Multilayer fabrication

The quality of interfaces is the most important parameter for the performance of multilayer optics. The limit on the quality of interfaces is determined by the size of the atoms. Perfect interface would require that the growth of one atomic plane start only when the previous plane is completely filled. The accurate control of the period and the quality of the each layer are of major importance for the optical properties. This requires a good control of the fabrication techniques used for depositing the multilayers.

Three fabrication techniques are widely used to deposit multilayer mirrors: ion beam sputtering [23], electron beam evaporation [24–27] and magnetron sputtering [28,29]. Among them, magnetron sputtering technique is commonly used as if has proved to be successful for preparing multilayer thin films. This technique allows the deposition of metals, alloys, ceramic and polymer thin films. There are two types of sputtering: direct current (DC) and radio frequency (RF) sputtering. DC magnetron sputtering is usually used to deposit the conductive materials and RF magnetron sputtering for the deposition of conductors, semiconductors and insulating materials. During the sputtering, a magnetic field is applied around the target to enhance the efficiency of the initial ionization process. It can generate plasma at lower pressures which reduces both background gases incorporation in the growing film and energy losses in the sputtered atom through gas collisions. Furthermore, the advantages of accurate control of thickness for each layer and growth of smooth interfaces make it an excellent method for improving the quality of thin film within the multilayers. Ogura *et al.* have compared these fabrication techniques by taking Mo/Si multilayer thin film as an example and found that best reflectivity is obtained by using the radio-frequency magnetron sputtering [30]. In 2002, Bajt *et al.* reported a reflectivity of 70% for the Mo/Si multilayer deposited by the magnetron sputtering [17]. Many materials and multilayers have been successfully deposited using this method [31–37]. All samples in our work are deposited by DC magnetron sputtering technique in Tongji university of China.

The instrument has two vacuum chambers which are separated by a valve. One is the depositing chamber, the other one for transferring samples. When depositing the multilayer thin film, the targets are mounted at the bottom and the substrates are placed above the targets.

The working gas is argon with the purity of 99.999%. In the sputtering process, the substrate was rotated and kept to be above of different targets with different exposure times until the deposition of the desired multilayer thin film structure.

1.5 Thermal stability of multilayer mirrors

We have mentioned in section 1.2 that the high reflectivity of multilayer optics requires a high optical contrast between layers, minimal absorption in the low-Z material and thin high-Z layer (thin absorber layer). In addition, the interface properties between layers play an important role during application. Namely when the multilayer mirrors are used at synchrotron radiation or free electron laser facility, they need to endure high photon fluxes and long working time. Therefore it is necessary to study the physico-chemical environment of interfaces in the multilayer structure to improve optical performance. The following requirements are necessary for achieving good optical performance: interfaces which are chemically stable with time, present minimal interdiffusion, minimal interfacial roughness (no crystallite formation within the layers), thermal stability during illumination and uniform coating thickness. In the following we will discuss the research progress about interface properties in the multilayer optics.

As a classic example, the thermal stability of the Mo/Si multilayers used in the EUV range has been widely studied [26,38–42]. Moreover the Mo/Si multilayers are expected to show a rapid degradation under EUV exposure. The reasons for causing a decrease of the optical contrast in the multilayers are due to the oxidation of surface, interdiffusion and formation of compounds at the interfaces. The basic physics about the evolution of interfacical structure upon the thermal treatment have also been studied by many researchers. Bajt *et al.* reported a transition from amorphous to crystalline of the Mo layer as a function of its thickness [23]. It was found that the Mo layer structure is amorphous when the thickness is less than 2 nm, while it is polycrystalline when thicker than 2 nm. In 2002, Yulin *et al.* reported that the interlayer transition zones existed in the Mo/Si multilayer and proposed a model for explaining a transition from asymmetrical to symmetrical for these interlayers. In that model, they pointed out that the formation of interlayer transition zones at the Mo-on-Si interface is controlled by the surface diffusion of Si atoms on the growing Mo surface layers, and at the Si-on-Mo interface the interlayer transition zones formation is determined by the diffusion of Si atoms in textured Mo grains [43].

Based on amount of studies about interdiffusion mechanism, researchers have also studied how to reduce the interdiffusion during deposition and upon thermal treatment for improving the thermal stability. The use of heating substrate to 150 or175°C during deposition is reported for smoothing the interfaces and leading to the enhancement of reflectivity [24]. Addition of inactive material, such as C and B_4C, into the Mo/Si multilayer have also improved the thermal stability [25,41,44,45]. Braun *et al.* have compared the Mo/Si multilayers with and without C and B_4C barrier layers prepared with pulsed laser deposition and magnetron sputtering [46]. With B_4C and C barrier layers at the interfaces, interdiffusion was reduced. The resulting EUV reflectivity was improved up to 69.8% (λ=13.42 nm, α=1.5°) and 71.4% (λ=12.52 nm, α=22.5°).

1.6 Development of tri-layer multilayer optics

Bi-layer multilayers have been studied for many years and some of them have achieved high optical performances in the soft x-ray and EUV ranges as well as good thermal stability. However, the highest theoretical reflectance of multilayer mirrors is limited because of the absorption of materials over these spectral regions. Tri-layer multilayers, resulting from the addition of a third layer into bi-layer [33,37,47,48], were proposed with the aim of improving the optical performance and thermal stability. Firstly for the theoretical calculation, in 2002 Larruquert proposed sub-quarterwave multilayer mirrors with more than two different materials that exhibit a remarkable reflectivity enhancement [47]. It is reported that the highest possible reflectivity is obtained by selecting the most suitable materials arranged in the correct sequence. Some kinds of examples illustrate the benefit of sub-quarterwave multilayer coatings for high reflectance in the EUV range. Meltchakov reported that the Al-based tri-layer multilayers Al/Mo/SiC and Al/Mo/B_4C, have a normal incidence reflectance of 55% at 17 nm, 50% at 21 nm, 42% at 30 nm. Moreover the introduction of the stable materials C and B_4C reduces the interfacial roughness [49]. Furthermore, Gautier *et al.* have experimentally demonstrated the reflectivity enhancement with tri-layer B_4C/Mo/Si multilayers [50].

In addition to the enhancement of reflectance of multilayer with a third layer inserted into two layers in one period, there are other purposes for the multilayer, such as enhancement of stability and distinction of different interfaces behaviour upon thermal treatment. The former one was demonstrated by the introduction of B_4C into the Mo/Si multilayer for improving the thermal stability [41]. The latter has also been demonstrated to be effective for discerning the interface behaviour in some multilayers. For example, in the case of the Mg/Co multilayer with an insertion of Zr material as a third layer, the reflectance increases up to 50% from the original value of 42.6% and an asymmetrical effect was observed: sharp Zr-on-Co interface and intermixing Co-on-Zr interface [37,48].

Yttrium is a promising material for application in the multilayer and can provide good thermal stability. Indeed, Bosgra has reported that a 0.2 nm thick Y layer significantly reduces the silicon diffusion towards Mo in the B_4C/Mo/Y/Si system [51]. A theoretical study of the Y-based multilayers, for example, Pd/Y, Ag/Y, Mo/Y, Nb/Y, has shown that the combination of yttrium and these materials could give normal incidence peak reflectivity ranging from 50% to 65% in the 8-13 nm range [52]. The study of Mo/Y multilayer demonstrated that this stack is stable up to 400°C [53].

In this thesis, tri-layer systems with an insertion of Y material into Co/Mo_2C system are designed to work in the EUV range at near normal incidence. This is based on the study of bi-layer Co/Mo_2C multilayers, for which we cannot distinguish the effect of Co-on-Mo_2C and Mo_2C-on-Co interfaces on the reflectivity. After the insertion of Y materials, the theoretical reflectance is improved up to 54% from 45% (bilayer multilayers).

1.7 Proposal of Co-based multilayers

Most multilayer systems cannot attain the reflection and resolution requirements given by simulation because of the interdiffusion and chemical reaction between two adjacent layers and large roughness of each layer. Some strategies have been used to prevent the interdiffusion (mentioned in section 1.6). However, sometimes this is accompanied by a decrease of reflectivity [54]. Therefore it is necessary to find out suitable materials for making an efficient combination and carry out the systematic analysis of the interfaces in the multilayers for EUV and soft x-ray ranges.

Co is an appropriate material for interface studies since it can form sharp interface with a number of materials, for example, Mg, C, Mo, Zr and B_4C. In addition, its promising optical performance has been confirmed by the Co/Mg system [36]. Furthermore, the melting point of Co is high (1768 K) and thus can stay up in a harsh working environment such as synchrotron beamlines or space environment. Moreover, the low price of Co makes it easily available.

As Co is a ferromagnetic material, Co-based multilayers can be analysed by magnetic techniques, i.e. magneto-optical Kerr effect and nuclear magnetic resonance spectroscopy (NMR). Such studies can help us to understand the Co atom behaviour in the multilayer.

This work aims not only at designing and fabricating new optical elements to face development of sources and applications in the EUV and soft x-ray ranges, but also at developing a methodology devoted to the analysis of interface in these multilayer structures in order to improve their optical properties by combining simulations and experiments. We also expect to prepare new Co-based multilayers with not only outstanding optical properties but also good stability in some harsh working environment.

We firstly design the Co/Mo_2C multilayers working in the soft x-ray range at grazing incidence and study their thermal behaviour upon annealing up to 600°C for one hour. We use some non-destructive methods to characterize the optical and structural properties. The reflectivity data in the hard x-ray range (0.154 nm) are used to obtain the structural parameters (thickness, density and interface roughness of each layer), the reflectivity data obtained in the soft x-ray range (1.59 nm) are being used to obtain the interface structure. X-ray emission spectroscopy and x-ray diffraction combined to calculation of enthalpy of intermixing are used to explain the interface behaviour upon the annealing. Then we introduce a third material (Y) into the bi-layer Co/Mo_2C multilayer to discern the Co-on-Mo_2C and Mo_2C-on-Co interface effects on the optical performance. The theoretical reflectivity is foun to be enhanced up to 54% (original 45%). The same characterization methods are used on the tri-layer systems.

1.8 Outline

The contents include five chapters in this thesis. Chapter 1 introduces the research background of multilayer mirrors. Chapter 2 describes the characterization techniques non-destructive and destructive methods related to the study of optical performance and of interface properties of the multilayer stack. We will introduce some. Chapter 3 is about the study of Co/Mo_2C multilayers. The studies of tri-layer Co/Y/Mo_2C systems are discussed in the chapter 4. Chapter 5 summarizes the whole research results and draws attention to future research.

Chapter 2 Analysis techniques

In this chapter we will present the main characterization methods used in our work. Basic principle of each technique and description about experiments as well as setup will be presented.

2.1 X-ray reflectometry in hard x-ray range

X-ray reflectometry (XRR) is a non-destructive and non-contact technique for thickness determination between 2-200 nm with a precision of about 0.1-0.3 nm. This method can also be employed to determine the roughness of thin films and the density of a material which is calculated from the electron density. The principle of x-ray reflectometry setup is shown in Figure 2.1. An x-ray tube produces x-rays; a monochromator gives a monochromatic light; a slit is mounted after it collimates the light beam. A slit is also mounted before the detector for minimizing the aberration. In XRR measurements the intensity of the x-ray beam reflected by a sample as a function of the grazing angle is monitored. The mode of operation is θ-2θ mode in which the incident angle is always half of the diffraction angle, *i.e.*, the specular reflection condition is satisfied. The reflectivity, which is defined as a ratio between the intensity of reflected beam and that of incident beam, is related to the value of refractive index and x-ray wavelength. Structural parameters of multilayers can be obtained by fitting the reflectivity data. Informations provided by the x-ray reflectivity curves are shown in Figure 2.2. From the reflectivity curves, we can obtain information on the thickness, the density and the roughness of each layer.

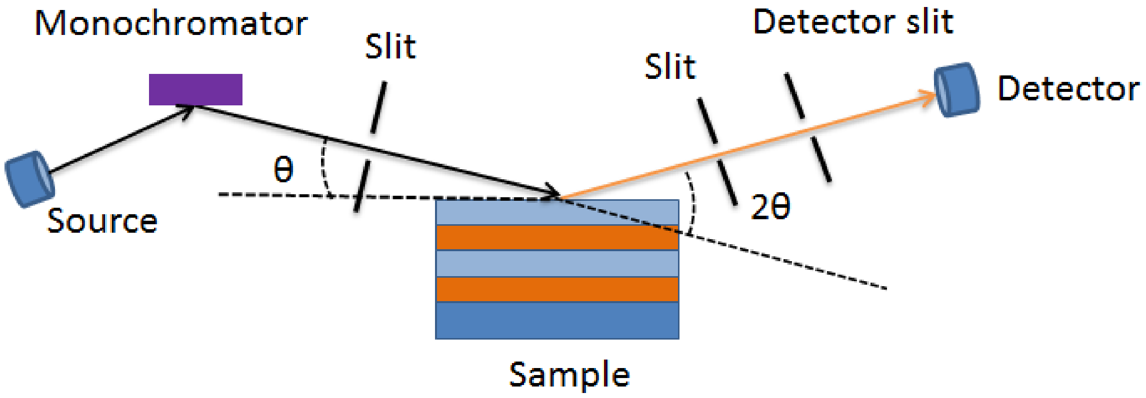

Figure 2.1 XRR reflectometry setup.

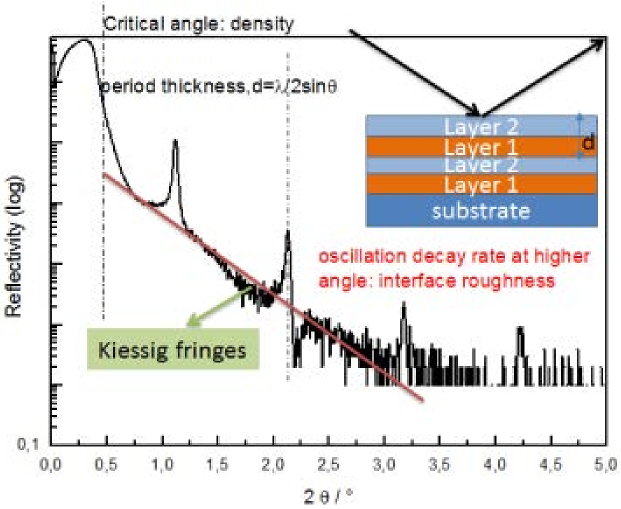

Figure 2.2 Informations provided by the x-ray reflectivity profile.

In this work, all the hard x-ray reflectivity measurements were performed with Cu Kα emission line (0.154 nm, 8048 eV) in Tongji University (China) with a reflectometer. The incident beam is monochromatized with a Si (220) crystal. The angular resolution is 5/1000°. The reflected beam travels through two slits and the photons are counted by a scintillation detector. The alignment is checked for each sample. After that we performed the fitting of reflectivity curves with Bede Refs software (genetic algorithm) [55] to estimate the thickness of individual layer and interface roughness as well as density of materials.

2.2 X-ray diffraction (XRD)

X-ray diffraction as a non-destructive technique is commonly used to determine the structural properties of solid materials. Diffraction effects are observed when electromagnetic radiation impinges on periodic structures with geometrical variations on the length scale of the wavelength of the radiation. The interatomic distances in crystals and molecules amount to 0.15-0.4 nm which correspond in the electromagnetic spectrum at of x-rays having photon energies between 3 and 8 keV. Analysis of diffraction peak can provide the following information: identification of compound or phase, crystallinity, strain, crystallite size, orientation.

In this work all the XRD experiments were performed by using a PANalytical X'Pert Pro diffractometer with Cu Kα radiation (0.154 nm) from an x-ray tube operating at 45 kV and 40 mA. The scan angle range starts at 10° and ends 80° with a step of 0.01°. The XRD patterns of the reference of Co/C multilayers were also performed as a comparison to the results of the Co/Mo_2C multilayers.

2.3 Reflectivity with synchrotron radiation

2.3.1 Description of the BEAR beamline

The BEAR (Bending magnet for Emission, Absorption and Reflectivity) [56] beamline is installed at the right exit of the 8.1 bending magnet at Elettra, Trieste in Italy. The beamline is designed to satisfy the following requirements: (a) a spectral range of approximately 3-1600 eV, (b) an energy resolution ≥ 3000 over the whole energy range, (c) a final spot size of the order of $10\times100\ \mu m^2$ and (d) the availability of elliptically polarized radiation with the possibility of ellipticity selection from linear to near circular polarization, all with an appreciable flux (Figure 2.3). The functions of the beamline can be employed to determine the performance of optical elements (*e.g.* mirrors and multilayers), optical devices and detectors.

The beamline is equipped with a device for selecting the polarization of light. There are three monochromators. Their parameters are listed in Table 2.1.

Table 2.1 Parameters of monochromators.

Grating	Energy range	Resolving power
G 1200	40-1600 eV	3000 @ 400 eV
G 1800	200-1600 eV	5000 @ 400 eV
GNIM	3-50 eV	2000 @ 20 eV

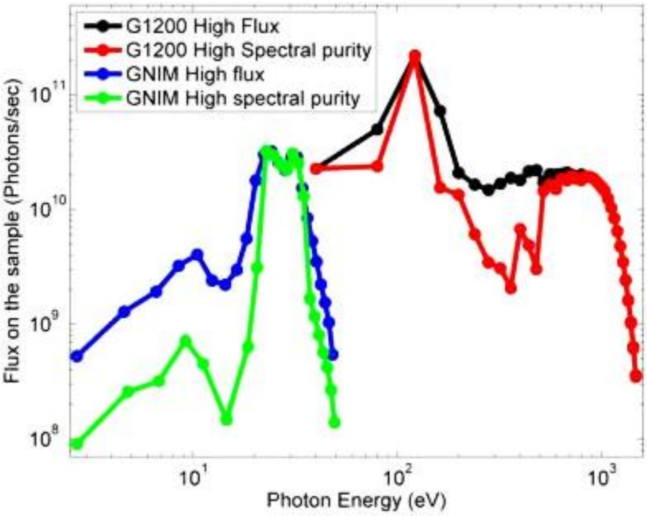

Figure 2.3 Experimental photon flux on the sample (E=2.4 GeV, elettra current 100 mA, vertical slits = 100 μm)

2.3.2 Experiments at the BEAR beamline

1) Reflectivity measurements

The measurements of reflectivity at the soft x-ray and EUV ranges can be made by scanning the photon energy at a fixed incidence angle or by angle scanning at fixed photon energy. During the experiment, the incident and reflected photon flux are collected by a silicon photodiode connected to a picoammeter. A tungsten grid continuously measures the flux after the monochromator to take into account any variation of the current in the storage ring.

To perform a reflectivity measurement, we firstly measured the currents (I_{d1}) in the photodiode corresponding to the direct incident beam and the electron current (I_{d2}) in the tungsten grid. Then, the currents (I_{r1}) in the photodiode corresponding to the reflected beam and the electron current (I_{r2}) in the grid were measured. The absolute reflectivity is calculated by the ratio of the two currents of the reflected and direct incident beams normalized to the electron current in the tungsten grid:

$$R = \frac{(I_{r1}-I_{rb1})/(I_{r2}-I_{rb2})}{(I_{d1}-I_{db1})/(I_{d2}-I_{db2})} \tag{2.1}$$

where I_{rb} and I_{db} correspond to the average background noise intensity from the measuring system. The error on the reflectivity value is about ±1%. All the experiments were performed with s-polarization radiation.

2) Rocking curve (off-specular) measurements

Rocking curve analysis is a good method to study the degree of preferred orientation in the crystals. This method is performed by rocking the sample (ω scan) while the detector is kept a fixed angle of 2θ with respect to the incident beam to record the diffraction intensities from the preferentially-oriented lattice planes. This method can also be applied to study multilayers. The scheme of this measurement is shown in the Figure 2.4.

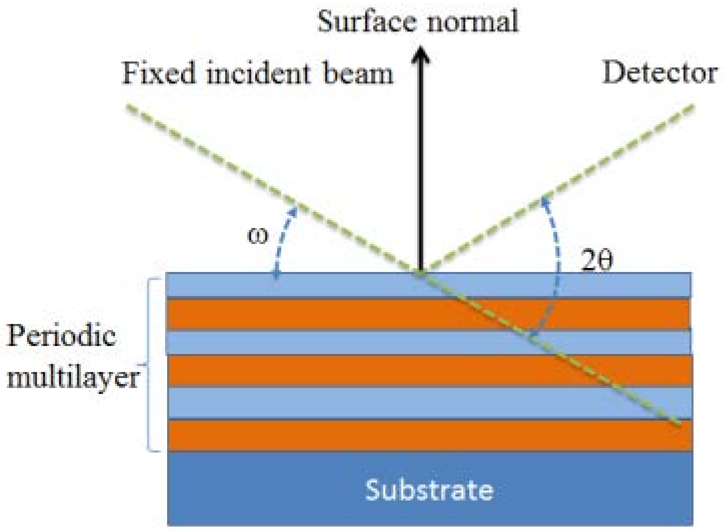

Figure 2.4 Scheme of rocking curves measurements.

When a multilayer structure is characterized by this method, it yields wide rocking curves compared to the perfect crystal. Lateral and vertical correlation lengths of the roughness of layers can be obtained by fitting the rocking curves. Before doing this experiment, we first need to determine the position of the Bragg peaks by making angle scan with fixed photon energy. Then we fix this angle between incidence beam and sample surface and rotate the sample around this Bragg angle. In this work, we performed rocking curves measurements for the Co/Mo_2C system to observe the lateral and vertical correlation lengths of the roughness layers upon annealing.

3) Fluorescence measurement induced by x-ray standing wave

It is known that a periodic multilayer illuminated under Bragg conditions is an XSW generator because of the strong interference between the incident and reflected waves (Figure 2.5). This standing wave field can be used to excite or generate the emission of photoelectrons, Auger electrons or characteristic x-ray emissions of elements from a thin sample deposited onto the multilayer or from the multilayer itself. X-ray photoemission spectroscopy (XPS) studies photoelectrons whose mean free path at some hundreds of eV is about 1~2 nm, while fluorescence detects photons coming from some hundreds of nanometers and thus is sensitive to many buried interfaces. Fluorescence requires doing the modelization of the whole sample, while XPS allows investigating in particular the first interface and then it is a good choice for the analysis of the evolution of the multilayer capping layer. In this specific case, XSW is a powerful technique to investigate the internal modifications of the multilayer induced by thermal treatment.

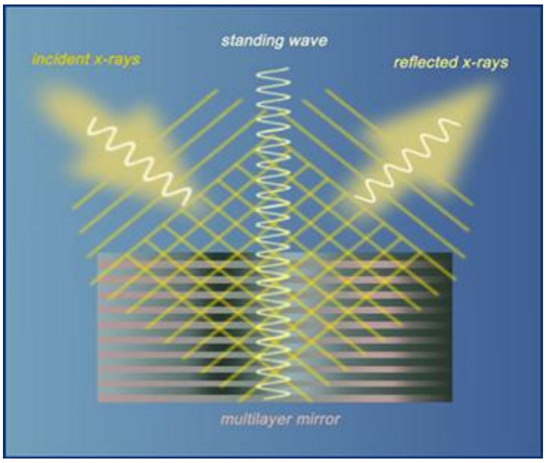

Figure 2.5 Scheme of x-rays standing wave [57].

In this thesis, we used the standing wave XPS to study the evolution of first buried interface between capping layer B_4C and first Mo_2C layer of the samples annealed at different temperature. We also used the x-ray standing wave technique to explore the study of either the center of the layers or their interfaces and obtain the depth distribution of the various species in the sample.

2.4 Reflectivity with MONOX apparatus

The MONOX apparatus consists of three different parts located in separated vacuum chambers [58]. A scheme is shown in Figure 2.6. The first part is an x-ray tube; the second one is a two-crystal monochromator and the third one is the θ-2θ goniometer. The whole apparatus works under a pressure of 5×10^{-7} Torr.

The radiation used for the experiments is either the Bremsstrahlung coming from a target of high atomic number (tungsten, gold, …) or a characteristic emission line: K line of light element (B to Si), $L\alpha$ line of transition elements (Cr to Pd). Thus, these lines cover the spectral range between 12.9 and 0.3 nm. The maximal excitation conditions in the x-ray tube are 10 kV, 100 mA.

There are three working modes: spectrometric mode, dispersion mode and reflectometric mode. In our case, we used the reflectometric mode working the $L\alpha$ line emission of copper (1.33 nm). Two W/C multilayer mirrors are used as monochromators. We firstly need to do alignment and put the detector in the centre of incident beam from the monochromator. We measure the intensity of incident beam I_0. After that we place the sample at the position where the detector receives the intensity of $I_0/2$. Then we make the alignment of sample, which means that the surface of the sample is coincidence with the plane of incident beam. We noted down the height of sample. Once again we measure the intensity of incident beam I_0 without sample and then we put the sample on the right position and measure the reflected intensity. The reflectivity is obtained by making the ratio between the reflected and incident intensities. The error on the reflectivity is less than 5%.

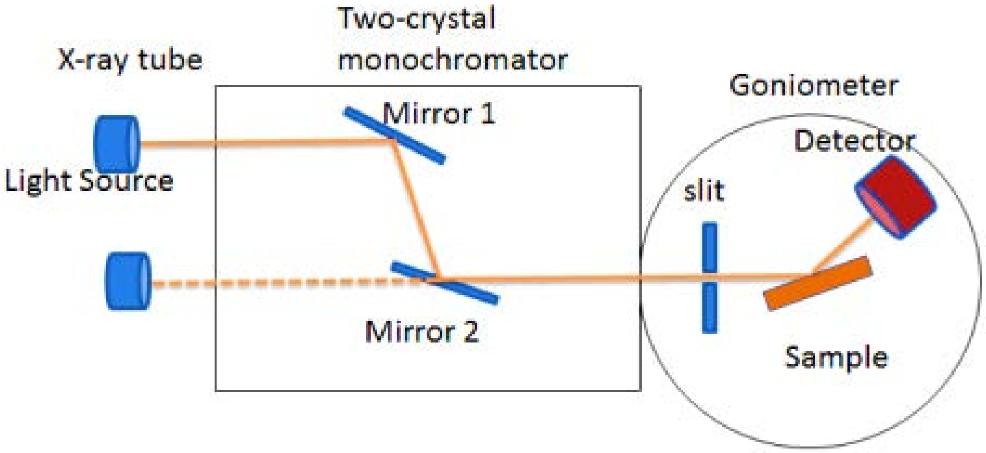

Figure 2.6 Scheme of the reflectometry MONOX in the reflectometric mode.

2.5 X-ray emission spectroscopy (XES)

2.5.1 The principle of XES

X-ray emission spectroscopy (XES) is a technique to study the electronic structure of bulk sample. It can probe the depth information up to few hundreds nanometres without sample damage. The schematic of the principle is shown in Figure 2.7. When high energy photons or electrons ionize atoms in a target sample, an x-ray emission process can be described as the transition of a valence electron or an electron from high energy level into a core hole. Local density of states for one type of atom can be measured separately from the others because the core states are well separated in energy. Electrons transitions between empty and filled levels are determined by the quantum selection rules. For the most intensive x-ray lines the electrical dipole transitions are followed:

$$\Delta l = \pm 1;\ \Delta j = 0\,, \pm 1$$

where l and j are the orbital quantum number and total angular momentum quantum number respectively.

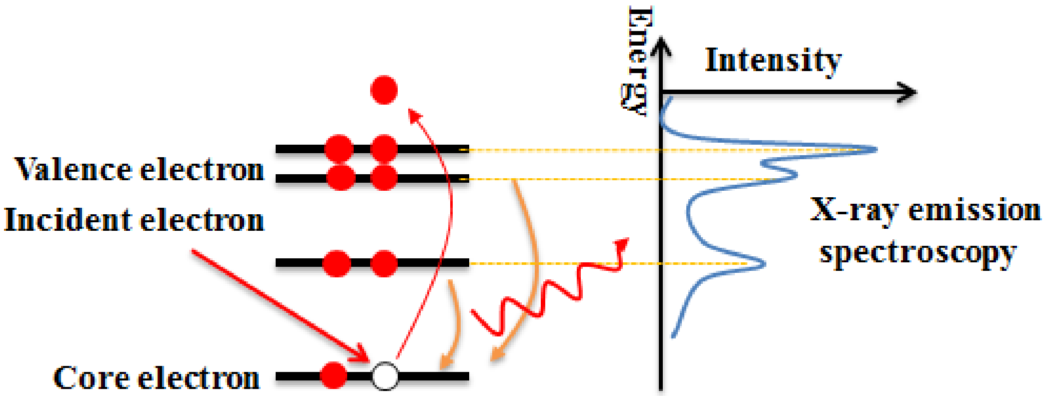

Figure 2.7 Principle of XES.

X-ray emission spectra reflect partial occupied density of electronic states. The position of peak and its chemical shift, the shape of spectrum as well as any satellites are important characteristics for analysing buried interfaces within the sample. The probed thickness can be determined by selecting the incident electron energy. In our experiment, we used the Monte Carlo CASINO program [59] to simulate the depth distribution of ionizations in a material subjected to electron bombardment and hence to determine the probed thickness. A model of the emission study is created and allows us to choose the angle and the appropriate incident electron energy.

2.5.2 Description of IRIS setup

Experimental setup IRIS (instrument for research on interface and surface) consists of three main chambers [60]:

(1) Preparation chamber: it is equipped with slot to insert devices for preparing thin layers. heating, annealing, cleaning samples. The chamber is connected to another chamber where the samples can be stored.

(2) Source chamber: In this chamber, there is an electron gun to bombard the sample which is the radiation source. The energy and the incident angle of electron beam determine the penetration depth of the electrons in the sample. The inclination angle of the sample is the results of compromise between maximizing of probed thickness and minimization of the phenomenon of reabsorption. The kinetic energy of the electrons may vary from 0 to 10 keV. We work with high focusing voltage that adjusts the size of the beam on the sample. The electron current density can be set from 0 to10 mA/cm^2. A sample holder cooled by water is used.

(3) Spectrometer chamber: The scheme of the spectrometer is shown in Figure 2.8(a). This room is equipped with dispersive spectrometer and curved crystal working in reflection mode. The focusing spectrometer is of Johann type [61], whose principle is shown schematically in Figure 2.8(b).

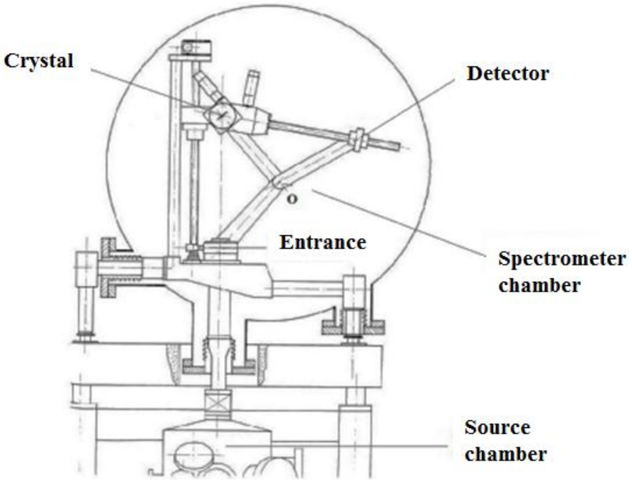

(a)

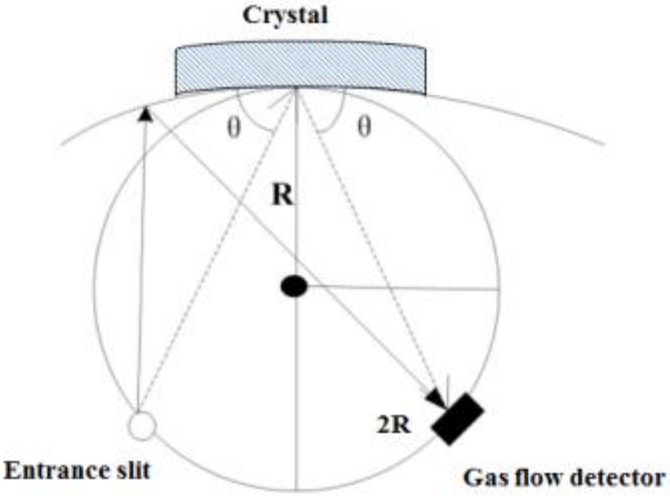

(b)

Figure 2.8 Scheme of the IRIS spectrometer (a) and principle of the Johann-type spectrometer (b).

In Figure 2.6(b), the beam reflected by the bend cylindrically (2R) crystal is focused on a cylinder of radius R, which is called focusing cylinder. The radius of curvature of 2R is 500 mm. The detector, placed behind an adjustable slit, is a gas (90% Ar and 10% CH_4) flow meter operating in the Geiger field.

2.6 Nuclear magnetic resonance (NMR) spectroscopy

Nuclear magnetic resonance (NMR) spectroscopy is based on the fact that nuclei of atoms have magnetic properties that can be utilized to yield chemical information. Quantum mechanically subatomic particles (protons, neutrons and electrons) have spin. In some atoms (^{12}C, ^{16}O, ^{32}S) these spins are paired and cancel out each other so that the nucleus of the atom has no overall spin. However, in many atoms (^{1}H, ^{13}C, ^{31}P, ^{59}Co), the nucleus does possess an overall spin. To determine the spin of a given nucleus one can use the following rules: if the number of neutrons and the number of protons are both even, the nucleus has no spin. If the numbers of neutrons plus the number of protons is odd, then the nucleus has half-integer spin (*i.e.* 1/2, 3/2, 5/2). If the number of neutrons and the number of protons are both odd, then the nucleus has an integer spin (*i.e.* 1, 2, 3).

The NMR allows the observation of specific quantum mechanical magnetic properties of the atomic nucleus. There are two possible measurement techniques. One is the conventional NMR where the sample needs to be placed in a high magnetic field. The applied magnetic field serves several purposes. Most nuclei have two states: spin-up and spin-down. When nuclei are placed in a magnetic field, the spin-down state is at a higher energy level than the spin-up state. The sample is excited by radio waves and then we measure the energy absorbed or emitted when nuclei flip between the two states. The same nuclei in different parts of a molecule have slightly different transition frequencies. Thus measuring these frequencies allows determining the environment of particular atoms in the molecule. The other one is the zero-field NMR; in this mode no external field is applied and the nuclei are excited by the oscillation of the hyperfine field which is created by the spontaneous magnetic moment in the magnetic materials.

The direct yield of a zero-field NMR experiment in magnetic materials is the hyperfine field produced by the electron spin polarization at the observed nuclei. As such, the measurement provides a direct insight, element and site specific, onto the electron moment values and possible magnetic structure. The hyperfine field is sensitive to the local environment of atoms, which can be used to study the local atomic structure of individual layers and the interfaces topology of metallic multilayers and superlattices. Indeed, the hyperfine field distribution (the NMR spectrum) reflects the occurrence probability distribution of all nearest neighbour configurations in the samples (each configuration giving rise to a characteristic line in the spectrum). In our work we use zero-field NMR to characterize the Co-based multilayers. In multilayers where there are several mixed planes at interfaces. The analysis of the interface concentration profile yields also the average hyperfine field for each atomic plane. This reflects the magnetization profile at the interfaces.

In this work, all the NMR experiments are carried out on the home-made NMR instrument in IPCMS (Institut de Physique et Chimie des Matériaux de Strasbourg). A spectrometer with 20-750 MHz wide band is used to receive the signal. To improve the sensitivity, the measurement temperature is 2 K for all the multilayers and 4.2 K for the disordered alloy reference. We measured the spin echo intensity of Co atoms surrounded by others atoms in the Co/Mo_2C and Co/Y/Mo_2C systems. Meanwhile the NMR spectra of some references Co_3Mo, CoMo1 %(at.) disordered alloys and Co/C multilayers were measured.

2.7 Time-of-flight secondary ion mass spectrometry (ToF-SIMS)

Time-of-flight secondary ion mass spectrometry (ToF-SIMS) is a surface-sensitive analytical method that uses a focused and pulsed particle beam (typically Cs or Ga) to sputter chemical species on a material surface. The resulting secondary ions are then accelerated into a flight path on their way towards a detector. The lighter ones arrive before the heavier ones. Their mass is determined by measuring their time of flight from the sample surface to the detector and a mass spectrum is recorded. There are three different modes of analysis in ToF-SIMS: (a) mass spectra are acquired to determine the elemental and molecular species on a surface; (b) images are acquired to visualize the distribution of individual species on the surface; and (c) depth profiles are used to determine the distribution of different chemical species as a function of depth.

Figure 2.9 shows the principle of the ToF-SIMS for the mode (c). Extremely short ion pulses with duration below 1 nanosecond are applied for high mass resolution analysis. These ion pulses are formed from a continuous beam by a pulsing unit and can be compressed in time by electro dynamic fields (bunching). The pulsed beam can be focused to a small spot to invesitgate a small area of interest and can be rastered to determine the lateral distribution of elements and molecules. During the drift time of the secondary ions, the extraction field is switched off and low energy electrons are used to compensate for any surface charging caused by primary or secondary particles. Thus all types of bulk insulators can be analyzed without any problems. The time during which the extraction field is switched off can also be used to apply low energy ion beams for sample erosion. In this case the low energy beam forms a sputter crater, the center of which is analyzed by the pulsed beam (dual beam mode).

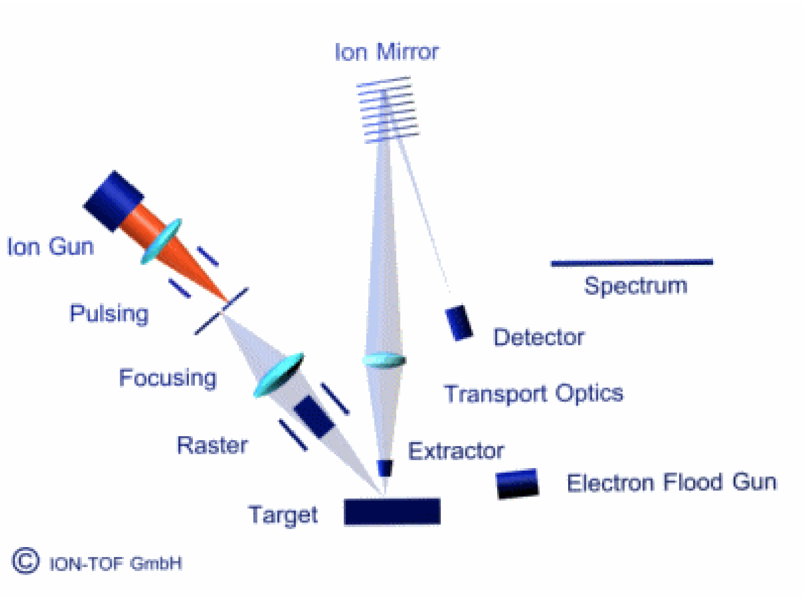

Figure 2.9 Scheme of the ToF-SIMS instrument.

In this work all the ToF-SIMS experiments described were carried out in LPCS (Laboratoire de Physique et Chimie des Surfaces) of ENSCP (Ecole Nationale Superieure de Chimie de Paris) on the ToF-SIMS 5 apparatus (ION-TOF GmbH). All the samples were analyzed by ToF-SIMS instrument working in the dual-beam mode. The sputtering was performed using a 1 keV (59 nA) Cs^+ ion beam, rastered over an area of 300 µm × 300 µm. A pulsed 25 keV Bi^+ primary ion source at a current of 1.3 pA (high current bunched mode), rastered over a scan area of 100 µm × 100 µm, was used as the analysis beam. The raster of the analysis beam was centred inside the etching one. Both ion beams were impinging the sample surface forming an angle of 45° and were aligned in such a way that the analyzed ions were taken from the center of the sputtered crater. Both positive and negative ions were recorded. In this work, only negative spectra are presented because they provided sufficient information. The ToF-SIMS technique provides only a qualitative chemical analysis as the relative concentrations does not correspond to the number of atoms in the multilayer (the sputtering yields vary from one element to another as well as from one matrix to another).

2.8 Transmission electron microscopy

2.8.1 Principle of TEM

The transmission electron microscopy (TEM) can be applied to investigate some parameters of multilayer thin film: layer thickness, crystallographic orientation in and out of the plane of films, physical roughness, chemical interdiffusion, grain size and orientation, atomic-scale structure and so on. High-resolution transmission electron microscopy (HRTEM) imaging is a type of phase-contrast imaging and can reveal crystalline defects, second-phase or amorphous layers and atomic-resolution structure across boundaries, as well as information on the topography of the interface, provided that it is properly aligned in the direction of the electron beam. Otherwise, the selected-area electron diffraction (SAED) can be performed inside HRTEM image to obtain the crystallinity of samples.

Scanning transmission electron microscopy (STEM) is a modification of the normal technique in which a nanometer-sized electron beam is focused and scanned point by point across the sample in a raster. In the STEM mode, an annulus-detector with a large hole in the centre is employed to exclude the coherently diffracted beams scattered at low angles. In this case, the images formed from the incoherently scattered electrons are known as high-angle annular dark-field images (HAADF). Because the image intensity depends only on the atomic number and thickness of the sample, the images can be interpreted directly and chemical concentrations of heavy species can be accurately estimated. In the STEM mode, we also performed energy dispersive spectroscopy (EDS) line profile, which is a tool for element analysis or chemical characterization, to determine the composition of layers in one period.

2.8.2 Preparation of sliced sample

It is known that the preparation of thin film slices for the TEM observation is difficult because the sample is thin and easy to destroy. Moreover diffusion can be introduced during the preparation, in particular when using a mechanical polishing method, in the step of annealing the stacks (“sandwich” sample) for hardening the glue. This is bad for preparing the as-deposited sample (deposited at room temperature). In our case, we use two methods to make the slices for the TEM observation. In the case of the as-deposited sample, in order to avoid the introduction of diffusion, we use focused ion beam (FIB) to cut the slices with the thickness of about 60 nm. Others samples with thermal treatment are prepared by the combination of mechanical polishing and ion milling.

Regarding the FIB method, a finely focused ions beam (usually gallium) is operated at low beam current for imaging or high beam current for site specific sputtering or milling. In our case, we first deposited a thin carbon rich platinum film to protect the sample surface against ion-beam damage. Then a thick platinum layer was deposited to protect the sample against ion milling damage. A first cross-section of the multilayers was cut and observed by scanning electron microscopy. A lamella, whose size is approximately 10 μm×4 μm with a thickness of about 1 µm, was excavated. Then it was lifted out using a micromanipulator and glued to a copper grid. A SEM image is shown in Figure 2.10. Finally, the lamella was polished by using ion milling to a thickness of about 60 nm, giving the electron transparency needed for TEM. Further thinning to about 30 nm in a Gatan Precison Ion Polishing System operating at 1 kV was performed to meet the requirement of the high resolution imaging experiment.

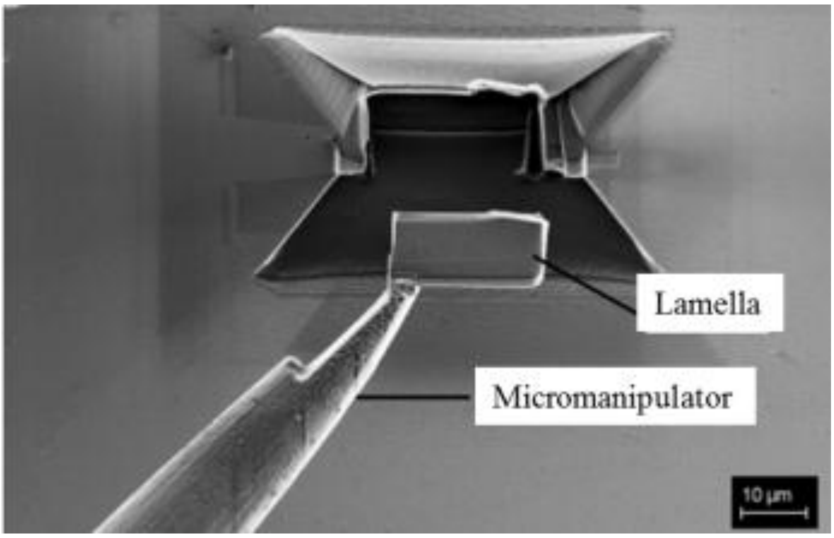

Figure 2.10 Scheme of a lamella lifting-out using a micromanipulator.

For the annealed samples, we used the mechanical polishing method combing the ion milling to prepare the slices. Firstly we need to prepare a sandwich stack using the glue M-Bond 610 to bond two small pieces (with the size of about 3 mm×5 mm) together via the way of face to face. After we put the sandwich stack in an oven about 2.5 h at 130°C. Then the sandwich stack was glued on a holder and then we used a precision diamond wire saw to cut the sandwich into some slices with thickness of about 750 µm. Then we glued the slices onto another holder and polished both sides until the thickness decrease down to be about of 30 µm. Last we unglued the polished slices and used the ion milling to thin it up to get a small hole.

2.8.3 Description of the TEM experiments

In our work, all FIB experiments described were carried out on the equipment NEON 40 BSE (FIB/TEM Cross Beam®, Carl Zeiss) of IMPMC (Institut de Minéralogie et de Physique des Milieux Condensés). All the TEM and STEM experiments were performed on the equipment Jeol 2100F in IPCMS (Institut de Physique et Chimie des Matériaux de Strasbourg). The applied voltage is 200 kV. The image resolution in TEM and STEM is 0.2 nm and 0.11 nm, respectively.

Table 2.2 lists all the analysis techniques used in our work and their advantages and disadvantages.

Table 2.2 Analysis techniques used in our work.

Technique	Principle	Obtained information	Advantages	Disadvantages
XRR	Constructive interference of x-ray beam	Layer thickness of thin film and multilayer Surface and interface roughness Density of material	Non-contact, non-destructive	Average information of the whole multilayer
XRD	x-ray diffraction from the crystalline structures	Crystalline structure	Non-destructive	Average information of the whole multilayer
XPS-XSW	X-ray interferometric method combining diffraction	surfaces and interfaces properties on the atomic scale	Non-destructive, elemental specific	Average information over 1 nm
XES	Electron induced x-ray emission	Chemical state of bulk material	Non-destructive, elemental specific	Average information
NMR	Magnetic properties of atomic nuclei	Atom local chemical environment	Non-destructive	Average information
ToF-SIMS	Ions sputter and ionize material from surface, with mass measured using mass spectrometer	In-depth intensity	High material selectivity	Limited in-depth information, destructive
TEM	Transmitted energetic electrons are imaged	Cross-section of multilayer structure	High in-depth resolution	Intensity scale has no calibration, destructive
HAADF-STEM	Measurement of high angle scattered electrons	Cross-section of multilayer structure	Sensitive to atomic number	Limited to high-Z material

Chapter 3 Study of Co/Mo_2C multilayers

In this chapter we discuss the optical performances and interface properties of Co/Mo_2C multilayers upon thermal treatment. We firstly investigate the reflectivity of Co/Mo_2C multilayer upon annealing from 200°C to 600°C for one hour, with an interval of 100°C. This is described in the section 3.1. The reflectivity was measured at hard x-ray range at grazing incidence angle for checking the periodic structure of the Co/Mo_2C multilayer stack. Then we measured the reflectivity in application wavelength of 1.59 nm at grazing incidence angle of 11°.

In section 3.2, we fitted all the reflectivity data to evaluate the structural and optical parameters of multilayers. In the section 3.3 and 3.4, we investigate the interface changes of the Co/Mo_2C multilayers upon annealing by combing non-destructive and destructive methods. We observe the evolution of the first buried interfaces upon annealing by using soft x-ray standing wave enhanced x-ray photoemission spectroscopy. In section 3.4 we present interface properties within the multilayer stack by using XES, ToF-SIMS, NMR and TEM techniques. Meanwhile we also calculate mixing enthalpy to interpret the interface change phenomenon.

The contents of this chapter are based on the following papers:

3.1 Investigation of reflectivity of Co/Mo$_2$C multilayer upon thermal treatment. Yanyan Yuan, Karine Le Guen, Jean-Michel André, Zhanshan Wang, Haochuan Li, Jingtao Zhu , Philippe Jonnard. **SPIE Proceedings**, 85501U-85501U-6. (2012).

3.2 Co/Mo$_2$C multilayer as x-ray mirror: Optical and thermal performances. Yanyan Yuan, Karine Le Guen, Jean-Michel André, Zhanshan Wang, Haochuan Li, Jingtao Zhu, Christian Mény, Angelo Giglia, Stefano Nannarone, Philippe Jonnard. **Physica Status Solidi(B)**, 251, (4) 803-808 (2014).

3.3 Interface analysis of heat-treated Co/Mo$_2$C multilayer. Yanyan Yuan, Karine Le Guen, Jean-Michel André, Christian Mény, Corinne Ulhaq, Anouk Galtayries, Jingtao Zhu, Zhanshan Wang, Philippe Jonnard. **Submitted.**

3.4 Thermal effects on Co/Mo$_2$C multilayer mirrors studied by soft x-ray standing wave enhanced photoemission spectroscopy**.** Angelo Giglia, S. Mukherjee, N. Mahne, Stefano Nannarone, Philippe Jonnard, Karine Le Guen, Yanyan Yuan, Jean-Michel André, Zhanshan Wang, Haochuan Li, Jingtao Zhu. **SPIE Proceeding**, 87770I-87770I-10 (2013).

3.5 Co/Mo$_2$C mirror as studied by x-ray fluorescence and photoelectron spectroscopies induced by x-ray standing waves. Philippe Jonnard, Karine Le Guen, Yanyan Yuan, J Jean-Michel André, S. Mukherjee, Angelo Giglia, Stefano Nannarone, N. Mahne, Zhanshan Wang, Haochuan Li, Jingtao Zhu. **SPIE Proceedings**, 85501D-85501D-6. (2012).

3.1 Investigation of the reflectivity of Co/Mo$_2$C multilayer upon thermal treatment

3.1.1 Introduction

Co-based multilayer mirrors can have a high reflectivity. For example the Co/Mg multilayer has a reflectivity higher than 50% at 25 nm wavelength at the angle of 45° [36,37]. In order to meet the needs of light sources working in the soft x-ray range, the Co/Mo$_2$C multilayer is proposed. Its theoretical reflectivity is 45% at 778 eV close to the Co L$_3$ absorption edge. It has been reported that a Mo$_2$C layer inserted into the Mo/Si multiyear as a barrier layer can improve its thermal stability up to 600°C [62]. Recently the optical properties of the B$_4$C/Mo$_2$C multilayer have been studied [63] and have given evidence of abrupt interfaces with respect to the B$_4$C/Mo multilayer where interlayers were detected. The standard enthalpies of formation of α-Mo$_2$C compound is ΔH_f^o(298.15 K)=-(6.37 ± 0.73) kcal.mol^{-1} [64]. This indicates that Mo$_2$C possesses a good thermal stability and is a good barrier candidate in the multilayer stacks.

Recently, some results on the thermal stability of the Mo/Si and Co/Mg systems have been reported. Stearns and Petford-Long reported that the reflectivity and period thickness of the Mo/Si multilayer decrease with increasing temperature because of interdiffusion of Mo and Si atoms at the interfaces [42,65]. Hu *et al.* showed that the thermal treatment have an influence on reflectivity for the Co/Mg system [66]. In this work, we focus on the influence of annealing temperature on reflectivity of Co/Mo$_2$C samples and try to find relationship between structural parameters and annealing temperature.

3.1.2 Experimental details

We first made simulations for obtaining the optimized parameters using optical constants from CXRO [67], thickness of each layer and period number giving a high reflectivity. A roughness of 0.5 nm of Si substrate was taken into account, but no interfacial roughness and interdiffusion between Co and Mo$_2$C layers. The multilayer period and the Γ ratio between the thickness of Mo$_2$C layer and the period were varied from 1 to 20 nm and from 0.1 to 0.9, respectively. A maximum reflectivity of 45% with a grazing angle of 11° was obtained at 1.59 nm (778 eV) when the period is equal to 4.10 nm and the Γ ratio to 0.36 (d_{Co}=2.60 nm and d_{Mo2C}=1.50 nm). This photon energy is close to that of the Co L$_3$ absorption edge.

The Co/Mo_2C multilayers were deposited on the polished Si (100) wafers substrate with a surface roughness of 0.40 nm *rms*. The base pressure was 10^{-5} Pa before deposition. The sputtering gas was argon (99.999% purity) at a constant working pressure of 0.1 Pa. The power applied to sputtering target was 40 W for Co and 60 W for Mo_2C. Six samples with an area of 20 x 20 mm^2 were deposited separately on the Si wafer under the same conditions. From one sample to another a small variation of the period can exist. The bi-layer number for each sample was 30. The first layer on the substrate is the Co one. To prevent oxidation, a 3.50 nm thick B_4C capping layer was deposited.

To investigate the thermal behaviour of Co/Mo_2C multilayer, five samples were annealed at 200°C, 300°C, 400°C, 500°C and 600°C for one hour in a furnace with a base pressure of 3.0×10^{-4} Pa. After annealing, the samples were cooled down to room temperature naturally.

3.1.3 Results and discussion

1) X-ray reflectivity at 0.154 nm

The reflectivity curves of the Co/Mo_2C multilayers with different annealing temperatures up to 500°C are presented in Figure 3.1 on a logarithmic scale. Four well-defined Bragg peaks are observed in all the probed range. They are almost the same from room temperature to 400°C, which indicates that the Co/Mo_2C multilayer is stable up to 400°C. However, at 500°C, the 4th Bragg peak almost disappears. This phenomenon could be due to a change of the interface structure. Some parameters such as the period and interfacial roughness, deduced from the fit of the XRR curves, are listed in Table 3.1, except density. The density ratio, which is the density of the layer with respect to the bulk value, is determined with a 15% uncertainty and within this uncertainty there is no significant density change as a function of annealing. These fits were done using a bi-layer model, by considering only Co and Mo_2C layers in one period. The measured periods are in good agreement with the aimed value of 4.10 nm but vary slightly from one sample to another one (see the column before annealing) because the sample have been prepared separately. The densities of the layer are close to those of the bulk materials taking into account the uncertainty. The roughness of the Mo_2C layers is small (0.25 nm) and independent of the annealing temperature. The fitted value of the roughness of the Co layer fluctuates largely with the annealing temperature between 0.3 and 0.8 nm, which is considered to be large with respect to the thickness of the Co layer ~2.60 nm. The roughness of the Mo_2C layers is smaller than that of the Co layers. This means that Co-on-Mo_2C and Mo_2C-on-Co interfaces are asymmetrical. This asymmetry has also been reported in Co/Mg and Mo/Si systems [43,48,68,69].

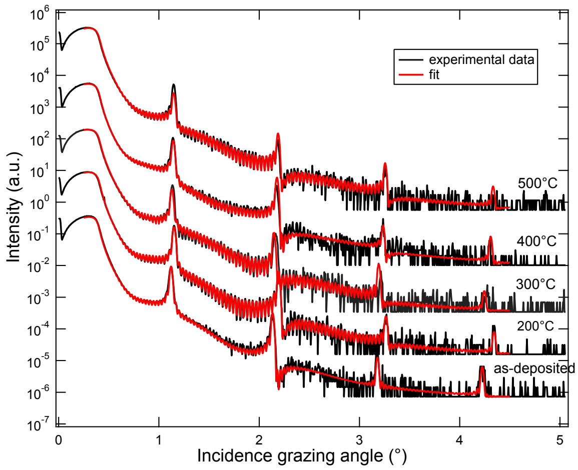

Figure 3.1 Reflectivity curves as a function of grazing angle measured at 0.154 nm of Co/Mo_2C multilayers annealed at different temperatures. Data of the samples annealed at 200, 300, 400 and 500°C are shifted vertically for the sake of clarity.

Table 3.1 Structural parameters derived from the fit of the XRR curves measured at 0.154 nm.

Sample	Period d (nm) before annealing	Period *d* (nm) after annealing	Thickness/Roughness (nm) (±0.05 nm)		
			B_4C	Co	Mo_2C
As-deposited	4.20	-	3.60/0.56	2.65/0.32	1.55/0.26
200°C	4.08	4.08	3.62/0.55	2.66/0.40	1.42/0.25
300°C	4.17	4.18	3.31/0.56	2.93/0.82	1.25/0.26
400°C	4.15	4.12	3.92/0.81	2.86/0.33	1.26/0.21
500°C	4.12	4.09	3.36/0.62	2.99/0.71	1.10/0.22
600°C	4.17	4.13	2.89/0.54	2.47/0.38	1.66/0.22

2) X-ray reflectivity with synchrotron radiation

First the samples were measured at the designed Bragg angle of 11° in the photon energy range of 745-805 eV. Reflectivity as a function of the annealing temperature is shown in Figure 3.2. The curves present two main peaks, one close to the Co L_3 edge and the other close to the Co L_2 edge. It can be seen that the maximum of reflectivity, happening for the sample annealed at 300°C, is 27.4% at 776.56 eV, which has a 1.54 eV shift with respect to the Co L_3 absorption edge at 778.1 eV. The maximum of reflectivity as well as its photon energy vary to some extent with the different annealing temperatures. For the samples annealed at 200, 400, 500 and 600°C, the photon energy corresponding to the maximum reflectivity are very close to Co L_3 edge. In order to move away from the Co L_3 edge, some measurements for the samples annealed from 200 to 600°C were also performed at a grazing angle of 11.25°. In this case too, the best reflectivity takes place on the sample annealed at 300°C. It is noted that a transition between annealing temperature of 500 and 600°C occurs, where the reflectivity decreases from about 25% to 20%.

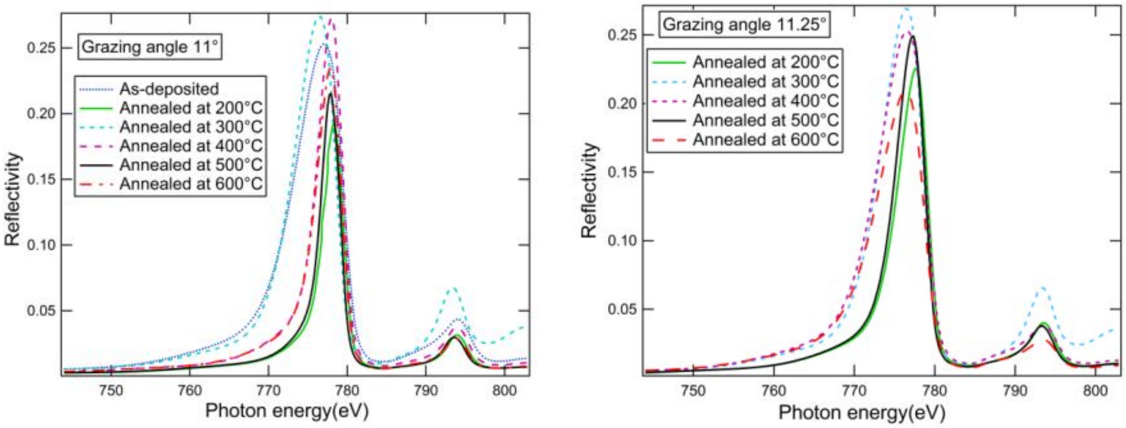

Figure 3.2. Reflectivity as a function of energy at Bragg angles of 11° and 11.25° for the Co/Mo_2C multilayers as-deposited and annealed from 200 to 600°C.

Figure 3.3 shows the reflectivity for all the samples up to the fourth Bragg peak in the θ-2θ mode in the range of 5-55°, where the photon energies used are determined according to the maximum of the curves obtained at the grazing angle of 11°. It can be seen that the differences between samples are more evident in terms of reflectivity and angular position at large angles. Detailed position and corresponding reflectivity of the four Bragg peaks are collected in Table 3.2. It is noticed that the reflectivity of the fourth Bragg peak for all the samples is less than 0.1%. In addition, except for the first peak, the other three Bragg peaks are surrounded by shoulders. This phenomenon is due to some contribution of the diffuse scattering. This was checked on one sample: in the same experimental conditions, we used a detector with a smaller angular acceptance than the one used to measure the sample annealed at 200°C and obtained the reflectivity curve without shoulders (not shown).

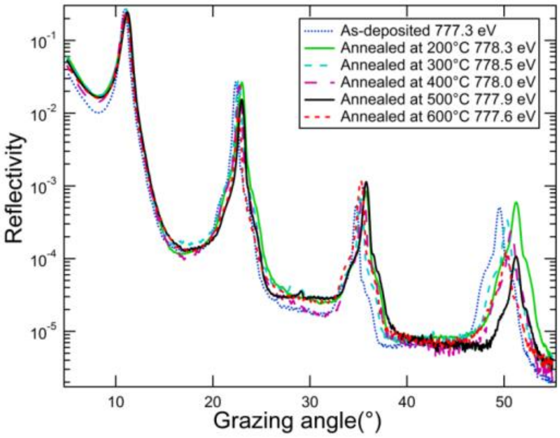

Figure 3.3 Evolution of reflectivity curves as a function of grazing angle at ~ 778eV photo energy (in the θ-2θ mode) for the Co/Mo_2C multilayers.

Table 3.2 Position and reflectivity of the four Bragg peak of the Co/Mo_2C multilayers.

Sample	Position of the Bragg peak / Reflectivity (%)			
	1st	2nd	3rd	4th
As-deposited	10.9° / 26.7	22.3° / 2.7	34.7° / 0.05	49.55° / 0.05
200°C	11.2° / 20.9	23.0° / 2.6	35.7° / 0.08	51.25° / 0.06
300°C	11.0° / 27.0	22.6° / 2.8	35.2° / 0.07	50.25° / 0.03
400°C	11.0° / 27.3	22.7° / 2.4	35.5° / 0.09	50.75° / 0.02
500°C	11.2° / 24.5	22.9° / 1.5	35.8° / 0.11	51.23° / 0.01
600°C	11.0° / 23.6	22.6° / 0.9	35.2° / 0.13	50.25° / 0.01

To investigate the lateral and vertical correlation length of roughness of annealed samples, off-specular measurements are also done. The evolution of the first and second Bragg peaks as a function of annealing temperature is presented in Figure 3.4 on a logarithmic scale. Concerning the first Bragg peak, the wing on the right of the Co/Mo_2C_600°C sample goes up towards high angles. For the second Bragg peak, the wing on the right of the Co/Mo_2C_300°C sample slightly goes up towards high angles. For other samples, no significant evolution of the curves as a function of annealing temperature takes place, except a slight change at both sides for the Co/Mo_2C_500°C sample. It is suggested that the lateral and vertical correlation length of roughness of samples annealed at 500°C and 600°C is slightly larger than that of other samples. In all cases the changes are small and indicate no large variation of the lateral and vertical correlation length of roughness in the Co/Mo_2C system as upon annealing. The slight change of lateral and vertical length of roughness should be responsible for the decrease of reflectivity upon annealing.

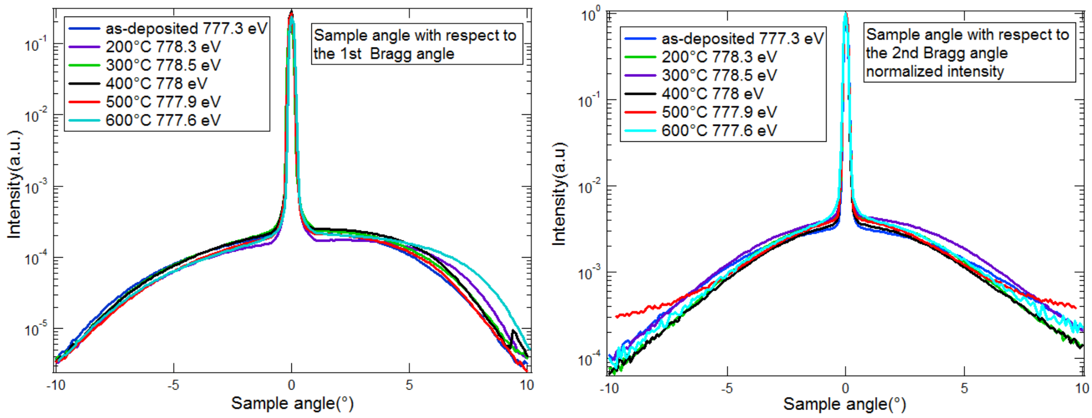

Figure 3.4 Off-specular reflectivity curves around the first and second Bragg peak for the Co/Mo_2C samples annealed at different temperatures.

3.1.4 Conclusions

The simulated reflectivity of Co/Mo_2C multilayer is 45% with a grazing angle of 11° in the soft x-ray range around the Co L_3 absorption edge. These multilayers are fabricated then annealed up to 600°C and their reflectivity is characterized. The x-ray reflectivity results show that the multilayers possess good thermal stability. The multilayer period derived from the fit of XRR curves is in good agreement with the designed one. The reflectivity obtained using synchrotron radiation in the soft x-ray range shows that the highest reflectivity, occurring on the sample annealed at 300°C, is about 27%. When the temperature goes up to 500°C, the reflectivity slightly decreases to 25% and then drops to 20% at 600°C. Off-specular reflectivity curves are also reported and show no significant changes, again showing the good thermal stability of the stack. From all above results, it is clear that this multilayer can work up to 600°C.

3.2 Evaluation of structure and optical parameters of Co/Mo_2C multilayer upon annealing

3.2.1 Introduction

We firstly characterize the optical performance of Co/Mo_2C multilayer with the combination of three methods: (1) XRR at 0.154 nm to determine the structural parameters of multilayer; (2) soft x-ray reflectometry (SXR) at 1.59 nm and 1.33 nm, *i.e.* close to and far from the Co L_3 absorption edge, to investigate the optical performances; (3) enhanced fluorescence by x-ray standing wave (EFXSW) to confirm the usefulness of the stack model. The value of the EUV optical index of nano-films in the vicinity of the absorption edges is known to have a large uncertainty. In fact, its accurate determination is required in order to calculate the optical performance of various optical films such as the proposed Co/Mo_2C multilayer. Thus, in addition to studying the optical performance of Co/Mo_2C multilayers in both hard and soft x-ray regions, we show in this part that it is possible to determine the optical index (n-ik) of a Co nano-film in the Co/Mo_2C multilayer system near the Co L_3 edge by combining these three methods.

X-ray reflectometry is a well-established technique to determine the characteristics (thickness, density, optical index) of thin films [37]. EFXSW in the soft-x-ray range is only in its early stage compared to the hard x-ray range [70]. Recently our team has developed a model based on the emission of a radiating dipole embedded in a multilayer structure to describe the EFXSW [71].

In this part we also explore the interface by simulating the electric field within the stack. It is known that in the x-ray standing wave technique excitation of the atoms of the stack is maximum at depths corresponding to the nodes of the electric field while it is kept at minimum at the antinodes of the field. This excitation can be at the origin of characteristic emission (or fluorescence) or of photoelectron emission. By slightly varying the angle around the Bragg angle, the position of the nodes and antinodes of the electric field moves and it is possible to probe either the center of the layers or their interfaces and so to obtain the depth distribution of the various species of the sample with a sub-nanometer depth resolution.

3.2.2 Results and discussion

1) Fitting of reflectivity curves

XRR reflectivity at hard x-rays has been described in the section 3.1.3 and gives the structural parameters.

SXR measurements in the Co L$_3$ region (1.59 nm) were performed at the BEAR beamline [56] at the Elettra synchrotron radiation center using *s*-polarized light. The photon energy was calibrated by x-ray photoemission spectroscopy (XPS) using as a gold reference. Since in the vicinity of Co L$_3$ absorption edge the refractive index of the Co nano-film may be strongly modified different from the tabulated bulk value, the real and imaginary parts of the Co refraction index have been considered as variables in the SXR fitting.

To confirm the description of each layer (thickness and roughness), reflectivity measurements around the first Bragg peak for samples annealed from 200 to 600°C temperatures were performed at 1.33 nm. They are presented in Figure 3.5. It can be noticed that the maximum position varies to some extent with the annealing temperatures, as has already been observed in the hard x-ray range (Figure 3.1). Within the experimental uncertainty, the values of period and roughness derived from the fit of the curves obtained at 1.33 nm are in agreement with those from the curves measured at 0.154 nm.

We use the structural parameters of the stacks taken from the fits of the reflectivity curves (both at 0.154 and 1.33 nm) to fit SXR curves by adjusting the optical indices, real and imaginary parts, of cobalt considering only a bi-layer system, *i.e.* Co and Mo$_2$C layers, without interlayers. The optical constants of the other materials Mo$_2$C and B$_4$C are kept fixed to their tabulated values [67] since these materials have no absorption edge in this spectral region.

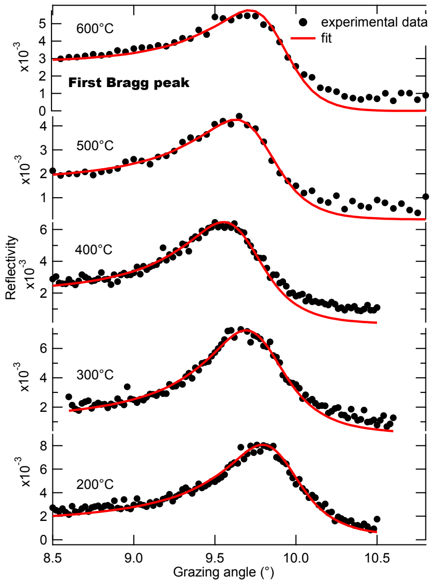

Figure 3.5 Reflectivity curves measured at 1.33 nm (Cu Lα emission) of Co/Mo$_2$C multilayers annealed from 200 to 600°C.

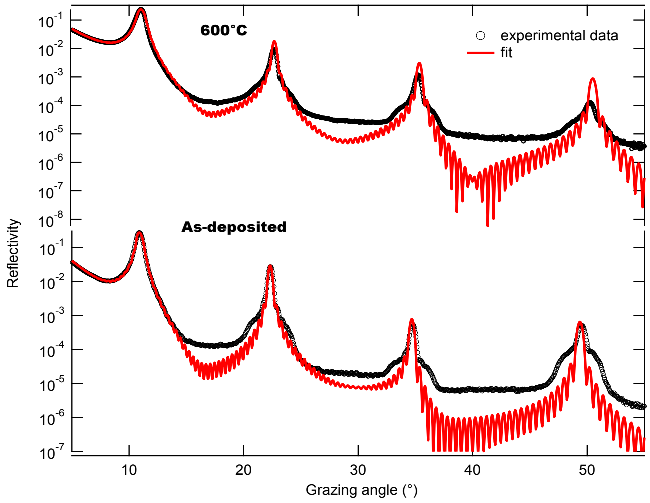

Figure 3.6 Comparison between soft x-ray reflectivity curves (black lines) and fit (red lines) using the parameters from XRR fit for as-deposited and 600°C annealed sample.

The corresponding reflectivity curves and fit results are presented in Figure 3.6 for the as-deposited and 600°C annealed samples. The variations of the Co optical indices *n* and *k* with respect to the CXRO (the center for x-ray optics) database [67] are listed in Table 3.3. It can be seen, the imaginary part *k* for both samples has to be modified significantly to obtain a good agreement, while the real part *n* is almost equal to the value from the CXRO database and needs only to be adjusted slightly. The same has been done for the reflectivity curve of the 200°C annealed sample. This leads to a 33% reduction of the imaginary part of the Co index (Table3.3). This means that the absorption in Co layers is much smaller than expected from the tables.

Table 3.3 Variations of the optical complex index *n*-i*k* of Co, with respect to the CXRO database required in order to fit the soft x-ray reflectivity curves obtained around 778 eV (1.59 nm).

Sample	*n* (% of tabulated value)	*k* (% of tabulated value)
As-deposited	99.96	24.0
200°C	99.98	33.0
600°C	100.0	40.0

It can be seen in Figure 3.7 that the database value does not take into account the fine structure of the absorption coefficient in the vicinity of the Co $L_{2,3}$ edge; in the database the absorption profile is represented by a single jump and the Co L_2 edge does not exist. It is surprising to see that the imaginary part of the index deduced from the absorption experiment [72] should be higher than that from the database while in our analysis it is the contrary. However, the experimental curve in Figure 3.7 is obtained for bulk Co and is probably not fully representative of Co nano-film owing to some possible change of density or of chemical state if some intermixing exists with the Mo_2C layers. Let us note also that a slight error in the photon energy calibration can affect significantly the imaginary part of the Co optical index.

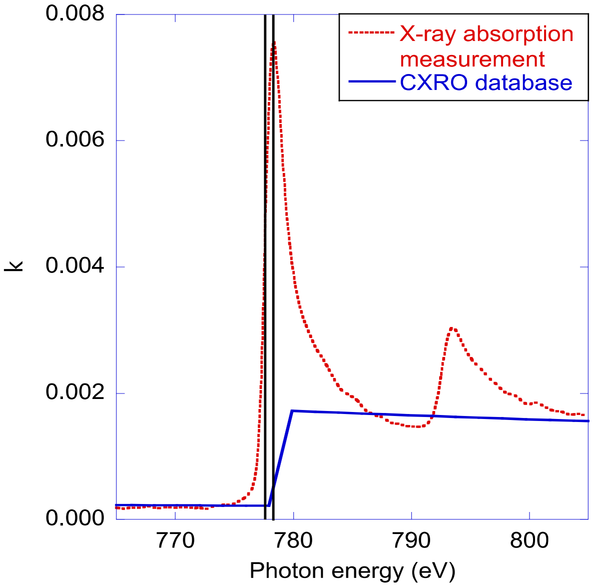

Figure 3.7 Comparison of the imaginary part of the Co optical index in the vicinity of the $L_{2,3}$ edge, deduced from absorption measurement (dotted line) and from the CXRO database (solid line). The two vertical bars indicate the photon energies used to perform the XSW measurements (right: sample annealed at 200°C; left: sample annealed at 600°C).

The reflectivity curves are well reproduced by the fits only to the low angle side (Figure 3.6). This is probably due to the fact that the simulations are made by considering the bi-layer model without the presence of any interfacial compound. Actually, formation of an interfacial compound should be considered as one reason for the variation of the imaginary part of the Co optical index upon annealing (see Table 3.3).

2) Enhanced Fluorescence by XSW

EFXSW is based on the system of standing waves obtained within a periodic multilayer structure in the Bragg diffraction regime. The peaks of electric field intensity can be localized in the regions of interest of the multilayer structure by adjusting the grazing angle of the incident excitation radiation. This radiation can give rise to fluorescence radiation coming mainly from the regions of the intensity peaks of the excitation radiation. This kind of experiment can be carried out with different geometries. In the present work we have adopted the so-called de Boer configuration [73] where only the incident excitation radiation undergoes Bragg diffraction. In our experiment the excitation radiation is around 778.3 eV for the 200°C annealed sample and 777.6 eV for the 600°C annealed sample. With a SDD detector [74], we record the intensity of the Co Lα emission line at 776.4 eV versus the grazing angle in the range 8-13° around the first Bragg peak (11°). The results are displayed in Figure 3.8. Curves of the samples annealed at 200 and 600°C are obtained at different incident photon energies and thus show different intensities. Indeed for the sample annealed at 600°C the absorption coefficient is low, as indicated by the vertical bars in Figure 3.7, thus leading to a low generation of Co L$_3$ ionizations and consequently a lower number of Co Lα photons. Another effect is the small angular shift of the first Bragg peak, as indicated by the vertical bars in Figure 3.8, leading to a small angular shift of the XSW curves.

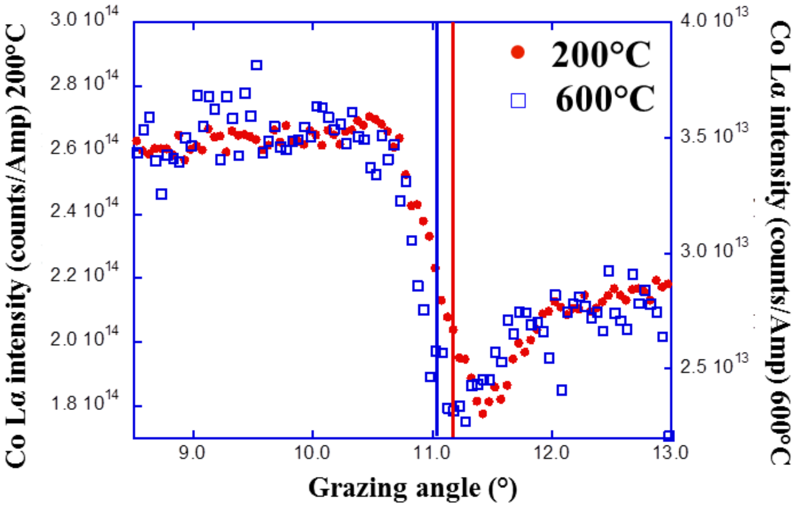

Figure 3.8 EFXSW curves of the samples annealed at 200 and 600°C versus the grazing angle; the recorded radiation is the Co Lα line. Full red circles: sample annealed at 200°C; open blue squares: sample annealed at 600°C. The vertical bars indicate the position of the first Bragg peak. Red bar: sample annealed at 200°C; blue bar: sample annealed at 600°C.

By means of the model given in Ref. [71], we have fitted the EFXSW curves using a bi-layer model as for the reflectivity fitting. Figure 3.9 shows the results: for the Co/Mo$_2$C_200°C annealed sample (Figure 3.9(a)). The tabulated value of the Co refractive index does not allow us to fit the experimental curve but using the tabulated value of the real part of the refractive index and 25% of the tabulated value of the imaginary part allows us to obtain an agreement provided one smoothens the theoretical results to take into account the aperture of the detector. This analysis is in agreement with the results of the reflectivity measurements. The same fitting procedure was performed with the Co/Mo$_2$C_600°C annealed sample (Figure 3.9(b)), and the best fit was obtained when 40% of the tabulated value of the imaginary part of the Co optical index is used.

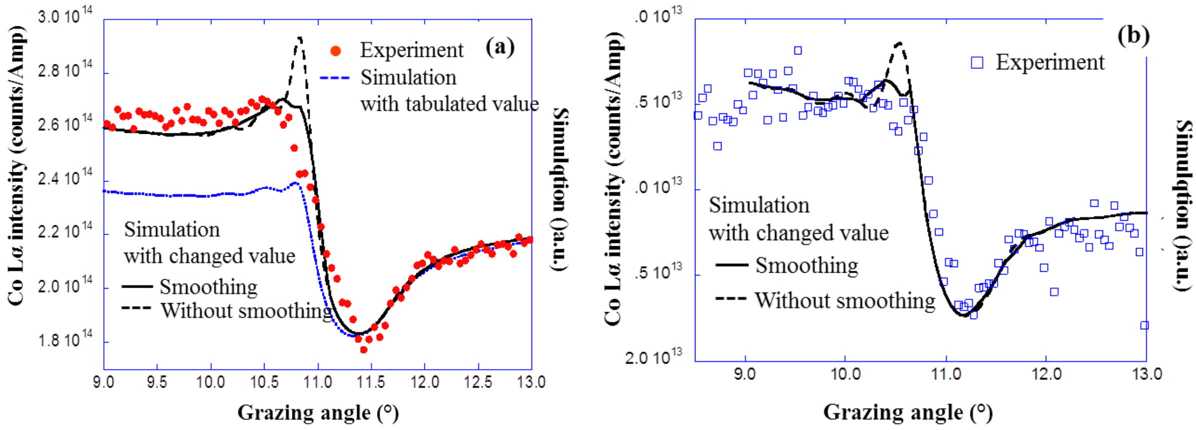

Figure 3.9 Comparison of the experimental (points) and simulated EFXSW curves (lines) for the samples annealed at 200°C (a) and 600°C (b); simulation with tabulated optical index of Co (blue dotted line); simulations with the imaginary part deduced from reflectivity measurements, without smoothing (black dashed line) and smoothing (black solid line).

Let us note that the simulation for the 600°C annealed sample seems better than the one for the 200°C annealed sample. This is probably due to the fact the simulations are made by considering the bi-layer model without interfacial mixing as also suggested in preceding part. Actually, the formation of an interfacial compound could be considered as one reason for the variation of the imaginary part of Co upon annealing (see Table 3.3).

3) Simulation of the electric field within the multilayer stack

All the following simulations were performed by using the optical constants of the CXRO. Let us note that the incident photon energy is very close to the Co L$_3$ edge. No interfacial roughness has been considered. We present the depth distributions of the electric field intensity by the radiation in the capping layer and the two top periods of the stack.

The electric field is calculated with the IMD code [1]. In Figure 3.10, the depth variation of the field is shown for three different angles: the Bragg angle and plus and minus one degree with respect to this angle. One can see the periodic oscillation of the electric field having the periodicity of the stack. The maximum of intensity is obtained for the Bragg angle. As a function of the depth, the field intensity decreases. When the grazing angle equals the Bragg angle, the maximum of the field lies in the Co layer close to the Co-on-Mo$_2$C interface, while minimum is close to the Mo$_2$C-on-Co interfaces. In the case of our sample the maximum of field is within the superficial boron carbide layer. When the angle shifts by one degree, the position of the maximum moves to the center of the Co or Mo$_2$C layers. In this case, both depth distributions of the field are almost in phase opposition. It is possible to put the intensity maximum at the Co-on-Mo_2C (and B_4C-on-Mo_2C) interfaces for an angle equal to the Bragg angle plus 0.4°. For larger angles, the maximum of the field shifts inside the Mo_2C layers.

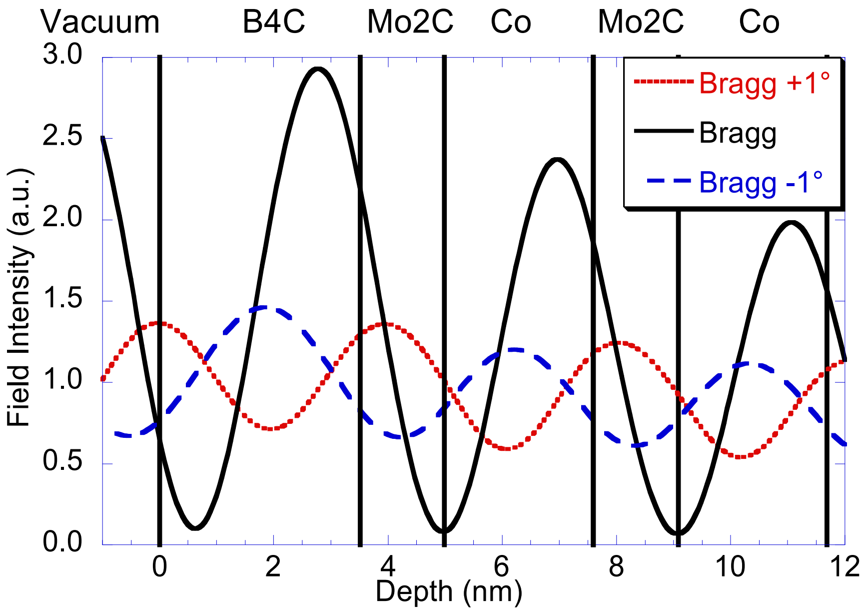

Figure 3.10 Depth distribution of the electric field intensity within the Co/Mo_2C sample excited at 778.3 eV for three different grazing angles: Bragg angle and plus or minus one degree with respect to this angle.

3.2.3 Conclusions

The optical properties of Co/Mo_2C multilayers have been studied by x-ray reflectivity measurements in the hard and soft x-ray ranges, and enhanced fluorescence by x-ray standing waves measurements. The values of the structural parameters of the stack derived from the fit of the XRR curves (at both 0.154 and 1.33 nm) show a good agreement between experimental and desired periods as well as a limited variation of period and interfacial roughness after annealing. The convergence between the analysis by reflectivity and by fluorescence, requiring the use of the same modified optical indices of the Co layers, confirms the description of the stack. Corresponding simulations of the depth distribution of the electric field were also presented.

3.3 Observation of the first buried interfaces within Co/Mo_2C multilayers studied by soft x-ray standing wave enhanced photoemission spectroscopy

3.3.1 Introduction

Standing wave enhanced x-ray photoemission spectroscopy is a powerful sampling depth spectroscopic technique, in particular for interferential multilayer mirrors [75,76]. It is based on the analysis of photoelectrons excited in the standing wave field that is created inside the periodic multilayer at the incidence angle that gives constructive interference. By rotating the sample around the resonant angular position, the standing wave moves vertically along the normal of the sample, exciting selectively the emitting atoms/molecules at different depths. Taking into account that the period of the standing wave is equal to the period of the multilayer sample, this technique can be sensitive to 1/10 of the period; then to some nanometers in case of soft x-ray optics, change of period by some tens of nanometers.

In this part we focus on the evolution of the first buried interfaces of a B_4C capped Co/Mo_2C multilayer mirror induced by annealing up to 600°C. We performed the soft x-ray XSW spectroscopy of the Mo 3d, B 1s, C 1s, O 1s core levels by using a photon energy close to that of the Co $L_{2,3}$ edge and corresponding to the first Bragg peak of the multilayer.

3.3.2 Results and discussion

The Co/Mo_2C multilayer annealed at 200°C and 600°C was studied by x-ray photoemission spectroscopy in correspondence to the first Bragg peak at a grazing angle of 11° with photon energy of 776 eV. The XSW analysis associated with XPS spectroscopy revealed to be useful for the analysis of the first interface Mo_2C-on-B_4C. The Mo_2C/B_4C system seems very promising for the development of soft x-ray multilayers [63], having Mo_2C optical properties very close to Mo but being more thermally stable and having lower mechanical stress.

A first overview photoelectron spectrum has been obtained on the both samples at 45° and the electron analyzer in normal emission. The XPS spectra peaks of B 1s, Mo $3d_{3/2}$ and $3d_{5/2}$, C 1s, O 1s are shown in Figure 3.11. The binding energy is located at 188.5 eV for B 1s (a), at 231.8 eV and 228.5eV for Mo $3d_{3/2}$ and $3d_{5/2}$ (b), at 285 eV for C 1s (c) and at 532 eV for O 1s (d). The monochromator energy was calibrated with the same incident photon energy the Au 4f spectrum of a clean gold film.

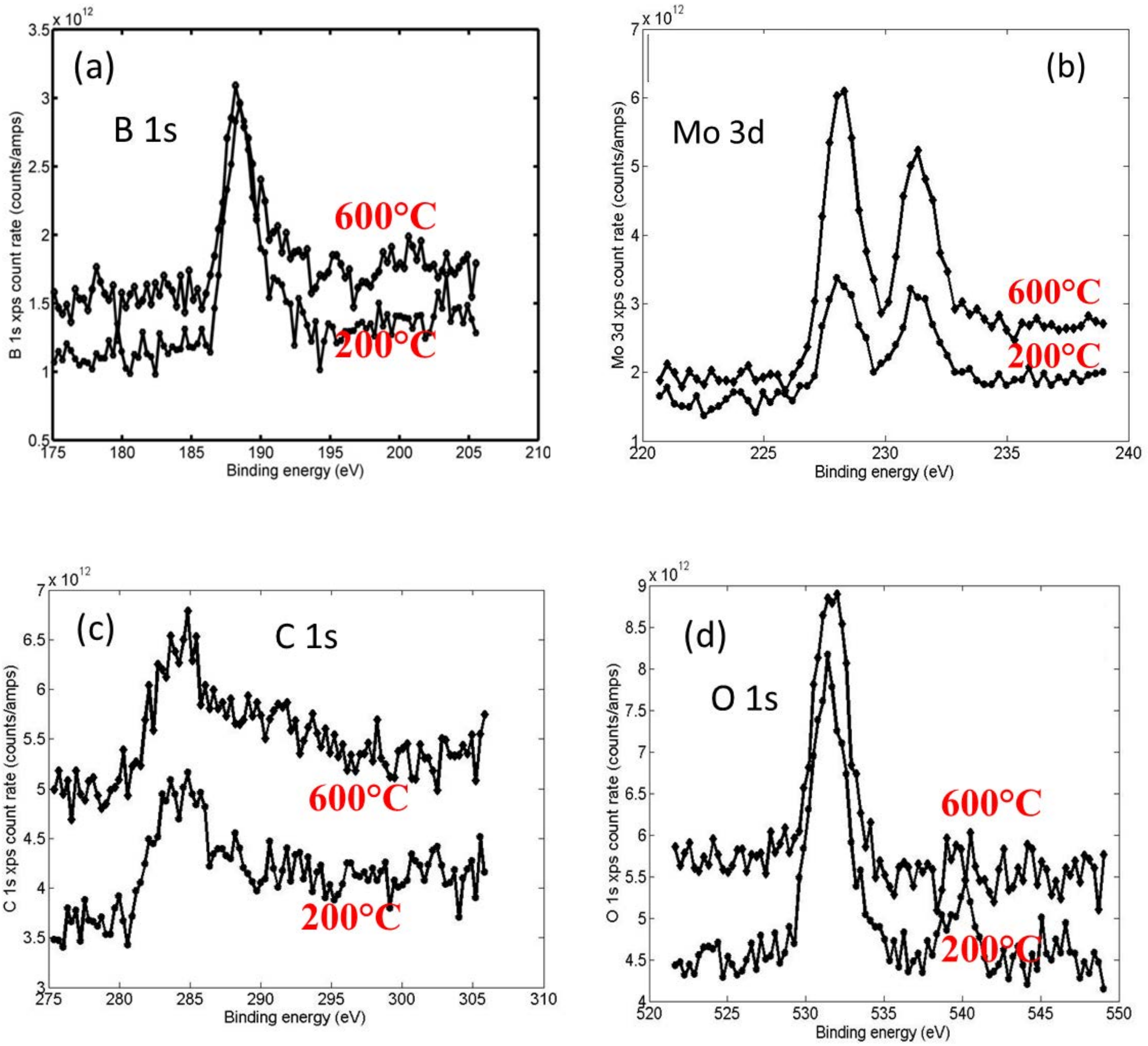

Figure 3.11 B 1s (a), Mo 3d (b), C 1s (c) and O 1s (d) XPS spectra of the multilayer samples annealed at 200 and 600°C. The ratios between integral areas of B 1s, Mo 3d, C 1s and O 1s XPS spectra between Co/Mo$_2$C_200°C and Co/Mo$_2$C_600°C samples are 0.92, 0.46, 1.3 and 1.43 respectively.

A quantitative analysis has been done by comparing the XPS intensities coming from Co/Mo$_2$C_200°C and Co/Mo$_2$C_600°C samples. It shows that the thermal treatment at 600°C induces an intensity increase of Mo 3d of about 2.2 times. The B 1s signal intensity remains almost constant for both samples, while the signals coming from O and C in the Co/Mo$_2$C_600°C sample decrease a factor of 1.3 and 1.4 respectively with respect to that of the Co/Mo$_2$C_200°C sample. The O 1s spectrum of Co/Mo$_2$C_200°C sample presents a peak at 540 eV that can be referred to solvents such as ethylic alcohol.

The same XPS analysis has been done corresponding to the maximum of reflectivity at the onset of Co L_3 edge with photon energy of 776 eV, around the Bragg peak at grazing angle of 11°. Figure 3.12 presents the comparison between the reflectivity curves of Co/Mo_2C_200°C and Co/Mo_2C_600°C samples which show their maximum at about 11.2° and 11.05° respectively with a peak value of 0.21 and 0.24 respectively. The reflectivity of the sample annealed at 200°C is lowest due to variation of the period of the as-deposited multilayers, whose Bragg condition is too close to the Co L_3 absorption edge.

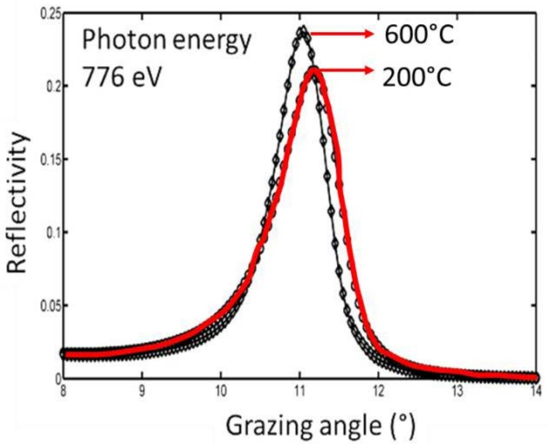

Figure 3.12 Reflectivity of the Co/Mo_2C_200°C and Co/Mo_2C_600°C samples as a function of the grazing incidence angle.

Simulations of electric field inside the samples have been performed with the OPAL code, assuming abrupt interfaces [77]. The calculation of the energy loss inside the structure from the electromagnetic wave is shown in Figure 3.13. According to simulations, the increment of the incidence angle moves the position of the standing wave towards buried depths of about 1 nm for one degree. As can be seen in Figure 3.13, the position of the reflectivity peaks can be used as a reference for the movement of the standing wave inside the sample.

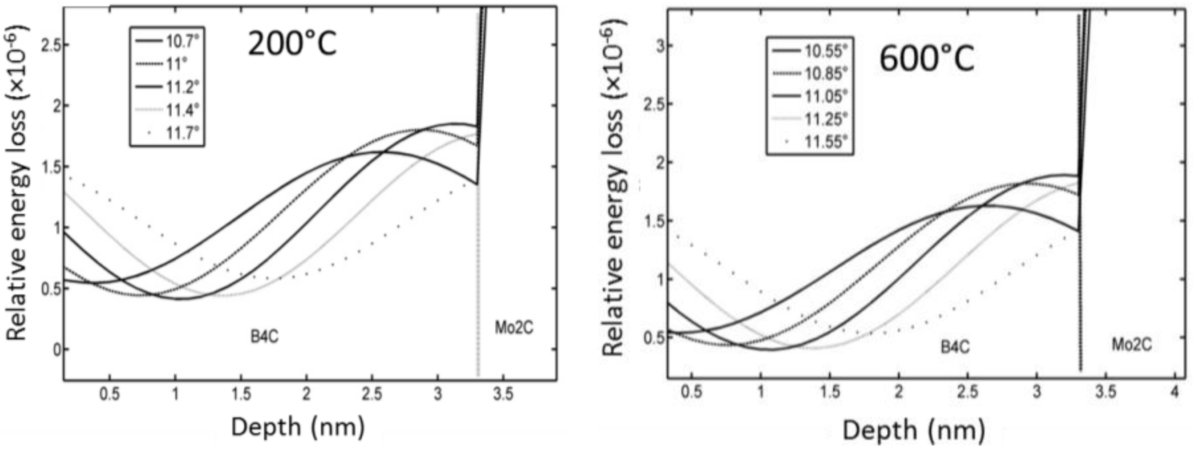

Figure 3.13 Calculation of the energy loss inside the Co/Mo_2C_200°C and Co/Mo_2C_600°C samples.

XPS spectra have been acquired with a step of 0.075° from 8° to 14°. For each spectrum, a quantitative analysis was performed with a MATLAB automatic procedure. The spectrum has been fitted, after subtracting a linear background, to the sum of Gaussian curves with amplitude, energy center and full width at half maximum as fitting parameters (Figure 3.14). The quantitative analysis of the spectra has been done by taking the integral of the Gaussian curves, after subtracting the background. The analysis of the binding energy show for both samples a drift of about 1 eV when going from normal to grazing angles, that could be ascribed to the change of the light penetration depth inside the sample and to the enhancement of the oxidation of the sample at the surface.

The Mo 3d XPS spectra of the Co/Mo_2C_200°C sample (Figure 3.14 (a)) are characterized by a doublet peak separated by 3.2 eV. Thus the quantitative analysis of Mo 3d has been done by fitting the spectra with two doublet components, with the doublet given by the sum of two Gaussian peaks with a shift of 3.2 eV and with fixed intensity ratio of 3/2 between the Mo $3d_{5/2}$ and Mo $3d_{3/2}$ components. According to the Ref. [78], the first doublet can be ascribed to Mo-Mo and Mo-C bonds of Mo_2C, while the shoulder component shifted by 1.5eV corresponds to an oxidized state. The intensities of the two contributions as a function of the grazing angle are shown in Figure 3.14 (b). A qualitative investigation of the data shows that there is a strong variation of the intensity of the XPS peaks corresponding to the Bragg resonance. The angular positions of the Mo-C peaks are shifted about 0.35° with respect to the reflectivity peak. This is well consistent with simulations, showing that at the Bragg peak the maximum of intensity falls at 0.4 nm from the first interface between B_4C and Mo. The fact that the angular position of the peaks is the same for both samples indicates that the first interface between Mo_2C and B_4C is quite stable up to 600°C.

The angular position of the maximum of Mo-O component shifts by about 0.4° and 0.2° to the low angles with respect to that of the Mo-C component for Co/Mo_2C_200°C and Co/Mo_2C_600°C samples, respectively. This indicates that the Mo-O component, buried 0.2 nm over the interface in the Co/Mo_2C_200°C sample, moves 0.2 nm towards the surface in the Co/Mo_2C_600°C sample and then that the 600°C annealing induces a progressive oxidation of about 0.2 nm of the first interface Mo-C-B_4C interface.

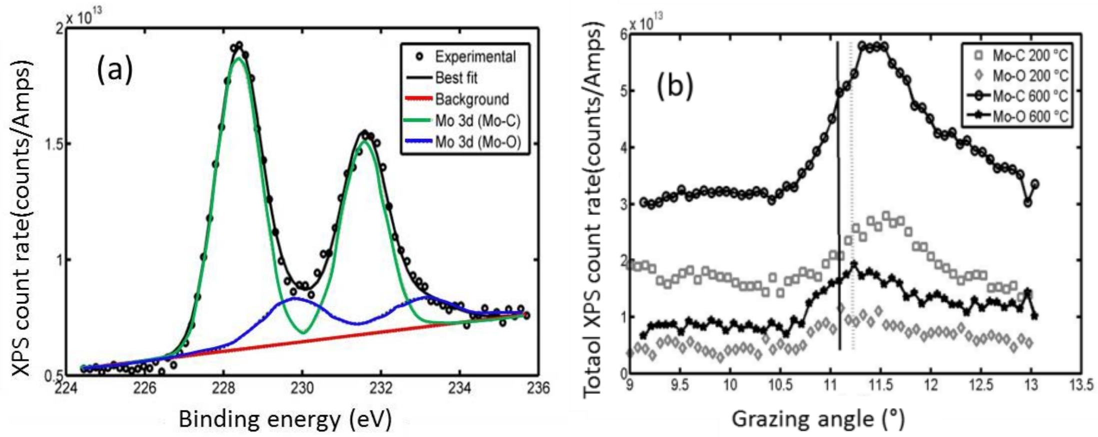

Figure 3.14 Mo 3d XPS count rate and fitting curves of the Co/Mo$_2$C_200°C sample (a), intensity of the fitting Gaussian components of the Mo 3d spectra of the Co/Mo$_2$C_200°C and Co/Mo$_2$C_600°C sample (b). Vertical bars are positioned at the Bragg peaks.

Figure 3.15 (a) show the B 1s XPS spectra peak of the Co/Mo$_2$C_200°C sample. It is comprised of a main peak located at 188.5 eV and a shoulder with a shift of 2 eV towards high energies. According to the Ref. [79], the main peak can be ascribed to B-B and B-C bonds of pure B$_4$C, while the shoulder at 190.5 eV can be ascribed to B-C-O and B-O bonds present in an oxidation B$_4$C layer. The analysis has been done by fitting the spectra with two Gaussian components. The two components for both spectra show an important angular modulation of the signal, as shown in Figure 3.15 (b). The position of the B-C peak decreases at higher angles due to the progressive shift of the standing wave to more buried depths. The slope minimum is positioned in the Co/Mo$_2$C_200°C sample exactly at the Bragg angle and shift by 0.2° toward high angle for the Co/Mo$_2$C_600°C sample. This indicates that high thermal annealing induces a diffusion of B$_4$C towards the interface with depth of about 0.2 nm.

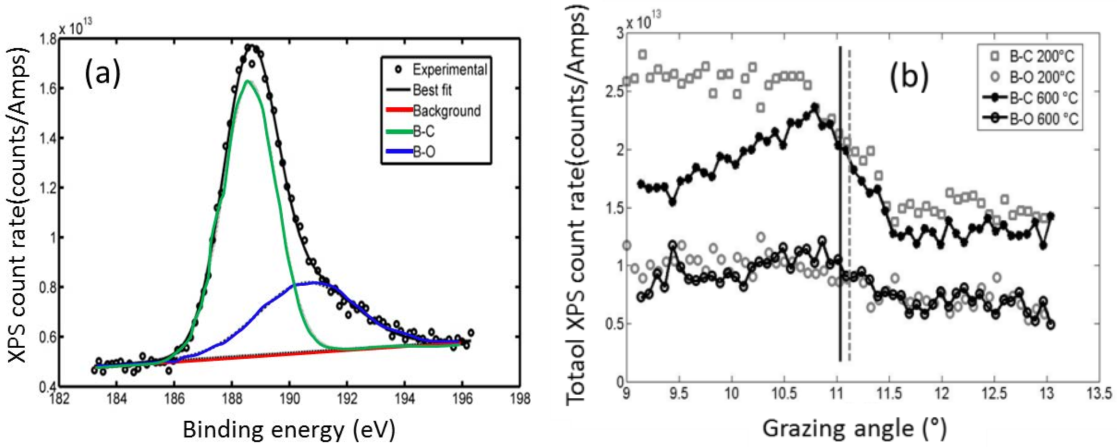

Figure 3.15 B 1s XPS count rate and fitting curves of the Co/Mo$_2$C_200°C sample (a), intensity of the fitting Gaussian components of the B 1s spectra of the Co/Mo$_2$C_200°C and Co/Mo$_2$C_600°C sample (b).

The O 1s XPS spectra of the Co/Mo_2C_200°C sample, shown in Figure 3.16 (a), present a main peak located at about 532 e, a small shoulder located at about 529.5 eV present at the left side of the main peak and a third peak located at 539.5 eV. The third peak is definitely less intense in the Co/Mo_2C_600°C sample. According to Ref. [79], the main peak at 532 eV can be assigned to the oxidation of the surface boron carbide and the shoulder at 529.5 eV to the oxidation of the buried Mo_2C layer [80]. Both spectra show an important signal modulation of the intensity of the main peak relative to oxidized B_4C corresponding to the Bragg peak. The modulation of the signal for the two samples is very different, indicating a progressive shift of the O 1s signal towards higher depths. The phase variation between the O 1s curves is about 0.9°, indicating a progressive oxidation of 1.0 nm of the B_4C capping layer. The intensity of the shoulder relative to oxidized Mo is low and does not allow us to evaluate eventual modulations.

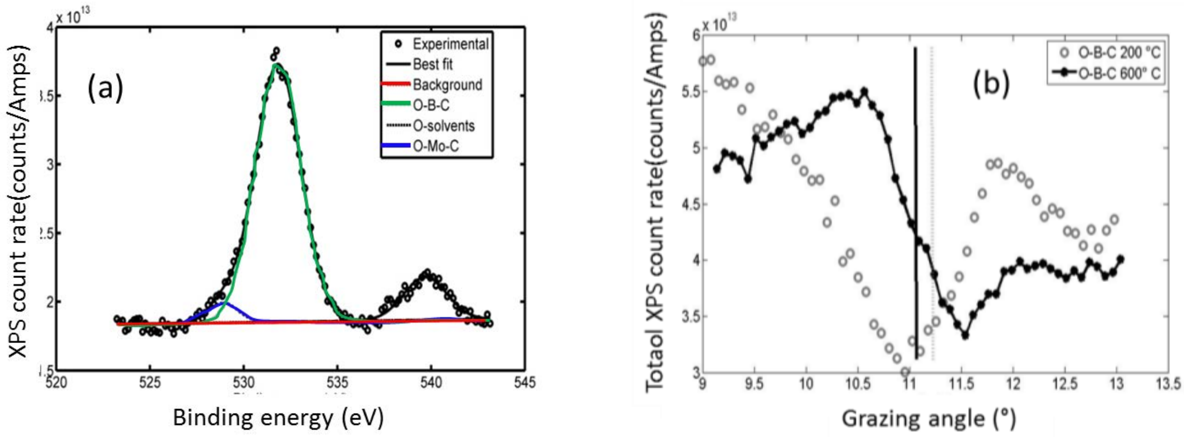

Figure 3.16 O 1s XPS count rate and fitting curves of the Co/Mo_2C_200°C sample (a), intensity of the fitting Gaussian components of the O 1s spectra of the Co/Mo_2C_200°C and Co/Mo_2C_600°C sample (b).

The C 1s XPS spectra of the Co/Mo_2C_200°C sample, shown in Figure 3.17 (a), are characterized by a main peak located at about 285 eV and three shoulders respectively located at around 283 eV, 288 eV and 294 eV. According to Refs. [78,79], the peak at 283 eV can be ascribed to carbide related to B-C bonds of pure B_4C or Mo-C bonds of pure Mo_2C, the peak at 285 eV to surface graphitized carbon and the peak at 288 eV can be ascribed to B-C-O bonds of oxidized B_4C. The peak at 294 eV can be ascribed to C-O bands of oxidation of B_4C. The quantitative analysis of C 1s for the Co/Mo_2C_200°C and Co/Mo_2C_600°C sample samples has been done by fitting the spectra with respectively three and four Gaussian components peaks at 283, 285, 288 and 294 eV. The analysis of the C 1s peaks confirms the previous analysis. The evolution of the carbide is very close to that of the B 1s component and indicates the diffusion of B_4C induced at 600°C annealing. It is not possible to distinguish in this case the contribution of Mo_2C, but being very low signal coming from buried Mo_2C; it does not modify significantly the evolution of the intensity. The evolution of the graphitized carbon, as expected, is very close to that of the O 1s component and confirms that thermal annealing induces a progressive oxidation of about 1 nm of the capping layer.

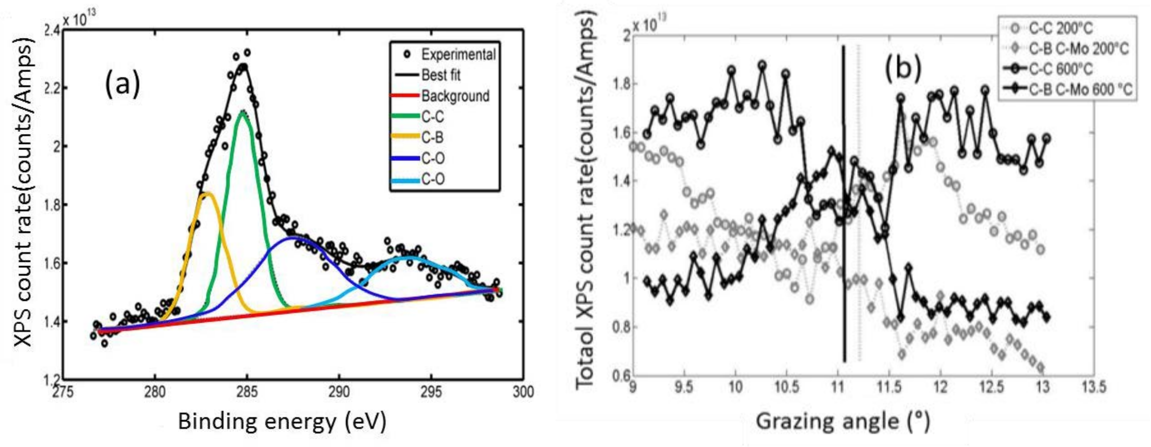

Figure 3.17 C 1s XPS count rate and fitting curves of the Co/Mo_2C_200°C sample (a), intensity of the fitting Gaussian components of the C 1s spectra of the Co/Mo_2C_200°C and Co/Mo_2C_600°C sample (b).

3.3.3 Conclusions

We studied the first buried Mo_2C-on-B_4C interface by using soft x-ray standing wave enhanced photoemission from the Mo 3d, B 1s, C 1s, O 1s core levels by using a photon energy close to the Co L_3 edge and corresponding to the first Bragg peak of in the Co/Mo_2C multilayer. Samples annealed at 200°C and 600°C have been studied. The experimental results have been compared with simulations to obtain information on the chemical state (*e.g.* oxidation state) and interface morphology in terms of profiles of distribution of elements and interdiffusion of B, oxidized B and C in the interface region. The results show the good stability of the Mo_2C-on-B_4C interface upon annealing and the good protective action of the B_4C capping layer. The analysis showed no significant increase of the Mo_2C-on-B_4C interface width, with only a small oxidation of 0.2 nm of the buried Mo_2C first layer. The increase of the surface carbide layer has been quantified to about 1.0 nm. The results confirm the usefulness of XSW for this kind analysis of multilayer optics.

3.4 Interface analysis of heat-treated Co/Mo_2C multilayers

3.4.1 Introduction

The evolution of interface structure upon annealing has been widely studied. In Mo/Si multilayers, it has been reported that the reflectivity decreases upon annealing owing to the increase of interdiffusion at interfaces [81]. The Co/C multilayers showed an enhanced reflectivity at annealing temperatures lower than 250°C due to phase separation [82]. Moreover a backward diffusion of two elements, from their mixtures to the pure elements, at the interfaces was also observed in the Co/Au, Co/Ag, Co/C and CoN/CN multilayers annealed up to 250°C [83–86].

In this part, we study the change of the interface properties of the Co/Mo_2C multilayer with the annealing temperature. The interface structure is studied by combining both non-destructive methods (x-ray emission spectroscopy (XES), nuclear magnetic resonance (NMR) spectroscopy, x-ray diffraction (XRD)) and destructive methods (time-of-flight secondary ions mass spectroscopy (ToF-SIMS) and transmission electron microscopy (TEM)). The comparison of the XES Co/Mo_2C multilayer spectra with that of reference samples, a Mo_2C thin film and Co/C multilayer, is used to determine the chemical state of the C atoms within the stack. NMR spectra of a Co_3Mo disordered alloy and two Co/C multilayers (as-deposited and 600°C) were also measured for reference. The depth distribution of the Co/Mo_2C multilayers was investigated using a ToF-SIMS instrument working in the dual-beam mode. We also performed the XRD and TEM measurements to check the phase structure and interface morphology of the Co/Mo_2C samples annealed at different temperatures.

3.4.2 Experimental methods

We prepared some reference samples for helping the interface study of the Co/Mo_2C multilayer. A reference Mo_2C thin film, with a thickness of about 60 nm, was deposited onto a silicon substrate using the same deposition conditions as the Mo_2C layers of the Co/Mo_2C multilayer. Three Co/C multilayers with the thickness of 2.0 nm for both Co and C layers in one period were deposited on a silicon substrate using the same conditions as for the Co/Mo_2C multilayers. Two of them were annealed at 300°C and 600°C for one hour in a furnace with a base of pressure of 3.0×10^{-4} Pa.

The C Kα emission (2p – 1s transition) from the Co/Mo_2C multilayers and the reference samples (Mo_2C thin film and Co/C multilayer) was analysed. Graphite was also used as a reference material. The Mo valence states have not been studied since the corresponding emission (Mo Lβ_2, 4d – $2p_{3/2}$ transition), accessible with our spectrometer, is not very sensitive to the chemical state of the molybdenum atoms. The same is true with the Co atoms [87].

3.4.3 Results and discussion

1) X-ray emission spectroscopy

The C Kα emission bands emitted by the as-deposited and annealed at 600°C Co/Mo_2C multilayers as well as the Mo_2C, graphite and Co/C multilayers references (for this latter, as-deposited and annealed at 600°C), are presented in Figure 3.18. The spectrum of the Co/Mo_2C annealed at 300°C is the same as that of the as-deposited sample and is thus not shown here. The spectra of the Co/Mo_2C annealed at 400 and 500°C are not shown here as they are the same as that of Co/Mo_2C annealed at 600°C (Figure 3.18 (a)).

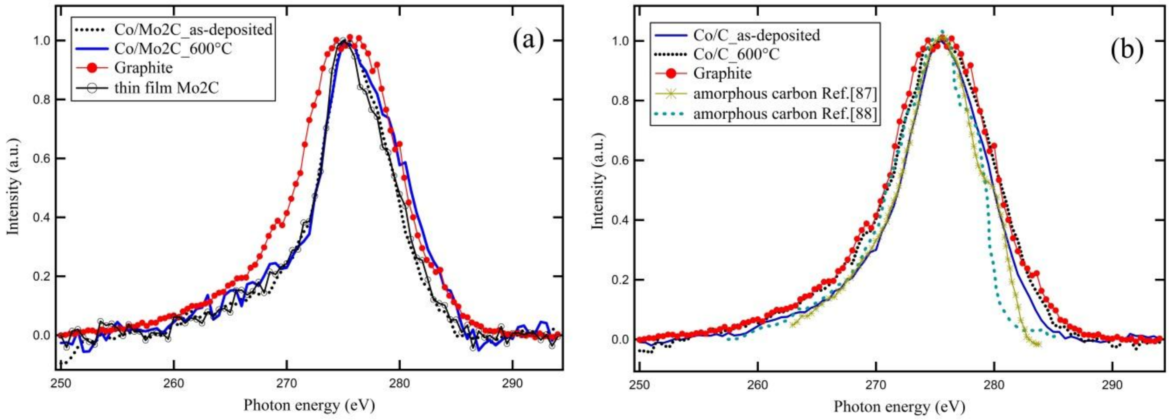

Figure 3.18 C Kα emission bands emitted by the as-deposited and annealed at 600°C Co/Mo_2C multilayers as well as the thin film Mo_2C, graphite (a) and by (as-deposited and annealed at 600°C) Co/C references, graphite and amorphous carbon from Refs.[87,88] (b).

Regarding the Co/C reference multilayers, the spectrum of the as-deposited Co/C sample should be similar to one of the amorphous carbons if no interaction takes place within the structure. The comparison with the spectra of amorphous C from Refs. [88,89] shows that this is not the case (Figure3.18 (b)). This indicates that, in the as-deposited Co/C system, some interaction exists between the C and Co atoms leading to intermixing between C and Co layers. The consequence is a change in the density of C (and Co) valence states and thus in the shape of the C Kα emission band. With respect to as-deposited Co/C, the spectrum of Co/C annealed at 600°C shows a significant broadening and is close to that of graphite. These results suggest that the Co and C atoms are intermixed within the as-deposited Co/C, while the annealing at 600°C induces the demixing of Co and C atoms and the "graphitization" of C layers.

The spectrum of as-deposited Co/Mo_2C is the same as that of both as-deposited Co/C and of the Mo_2C references. Thus the chemical state of the C atoms is not distinguishable in this sample: the carbon atoms exist either in the form of Co and C mixture or in the form of Mo_2C compound or in both forms. Following annealing at 400°C and above, the spectra of the Co/Mo_2C multilayers show a slight broadening towards the high photon energy side. This suggests that a slight change of the chemical state of the C atoms takes place from 400°C.

2) Zero-field nuclear magnetic resonance spectroscopy

NMR spectra of all Co/Mo_2C multilayers as a function of the annealing temperature are presented in Figure 3.19. It can be seen that the spectra of the as-deposited and 200°C samples consist of a wide structure without any extra feature. For the 300, 400, 500 and 600°C annealed samples, a well-defined line is observed at around 221 MHz. This intense line corresponds to bulk Co with an *hcp*-like structure [90]. However the frequency is lower than the one expected for well crystallized *hcp* Co. As suggested in Ref. [91], this is most probably due to the presence of a large amount of stacking faults within the layer. Regarding the as-deposited and 200°C annealed samples the absence of a well-defined feature indicates that most of Co atoms are mixed with other atoms (Mo or C). From 300°C, the intensity of the 221 MHz line increases with the annealing temperature while the low frequency (<220 MHz) contributions stay almost unchanged. This indicates that the total amount of ferromagnetic Co atoms as well as pure Co increase from 300°C and above. From the phase diagram of Co-Mo system showing the existence of several ordered phases, it is unlikely that annealing the samples result in a phase separation between Co and Mo. Therefore the strong intermixing revealed by the as-deposited NMR spectra is more likely a mixing of Co and C atoms. Since the Co carbides are not stable, the carbon atoms separate from Co-C mixed region upon annealing. This phenomenon has also been reported by H. Bai *et al.* [85].

To check this interpretation, we measured the NMR spectrum of a reference Co_3Mo disordered alloy, as well as the spectra of the Co/C multilayers as-deposited and annealed at 600°C (Figure 3.20). The spectra of the Co_3Mo disordered alloy and of the Co/C as-deposited multilayer show a low frequency signal (<220 MHz) without bulk Co peak. However in both cases the detailed shape of the NMR spectra is different from that of the Co/Mo_2C as-deposited sample. More interestingly, the spectrum of the Co/C sample annealed at 600°C shows an intense peak at about 220 MHz that can be attributed to *hcp*-like Co. This behaviour is very similar to the one of the Co/Mo_2C annealed multilayers. Therefore this strongly suggests that the phase separation observed after annealing of the Co/Mo_2C samples is due to the incorporation of C onto the Co layers of the as-deposited samples, the molybdenum staying outside the Co layer. The difference between the Co/Mo_2C and Co/C multilayers is attributed to the fact that the carbon content in the Co layer is different in the Co/C and Co/Mo_2C multilayers.

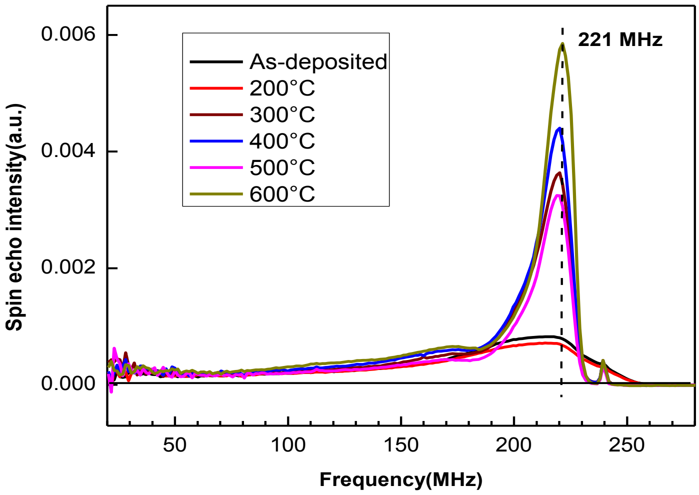

Figure 3.19 NMR spectra of the Co/Mo_2C multilayers as a function of the annealing temperature.

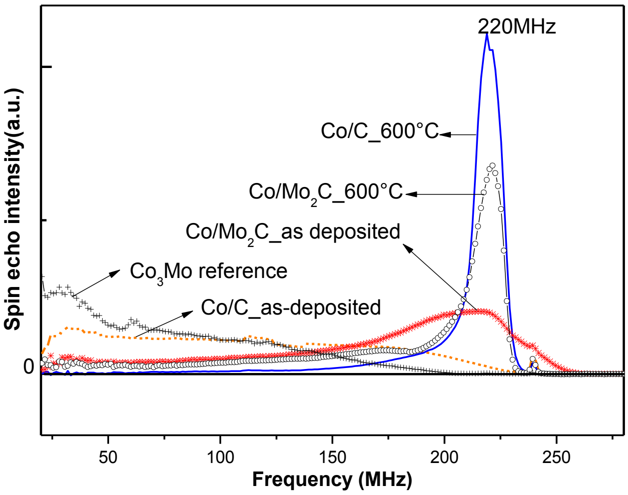

Figure 3.20 NMR spectra of as-deposited and annealed at 600°C Co/Mo_2C, compared to the NMR spectra of Co_3Mo disordered alloy and as-deposited and annealed at 600°C Co/C references.

3) X-ray diffraction

The x-ray diffraction patterns of the as-deposited and 200°C to 600°C annealed Co/Mo_2C samples are presented in Figure 3.21 (a). A broad and low intensity Bragg peak is observed at around 44° which corresponds to the Co (111) or Co_3Mo (002) phases. The intensity of this feature increases slightly from the as-deposited sample to 500°C annealed sample. After annealing at 600°C, the intensity increases much more showing a significant structural change. This phenomenon can be related to the recrystallization of the Co layers owing to the demixing of Co and C atoms after annealing or the crystallization of the disordered Co_3Mo mixture after annealing at high temperature.

In order to explain the change between Co and C layers upon annealing, we performed the XRD patterns of the Co/C multilayers (Figure 3.21 (b)). There is no intense peak to be seen. This means that the Co/C multilayers are mainly amorphous and the Co layers are not crystallized. It should be noted that the thickness of Co layer in one period is about 2 nm. So the probability of forming a crystalline phase in the stack is low.

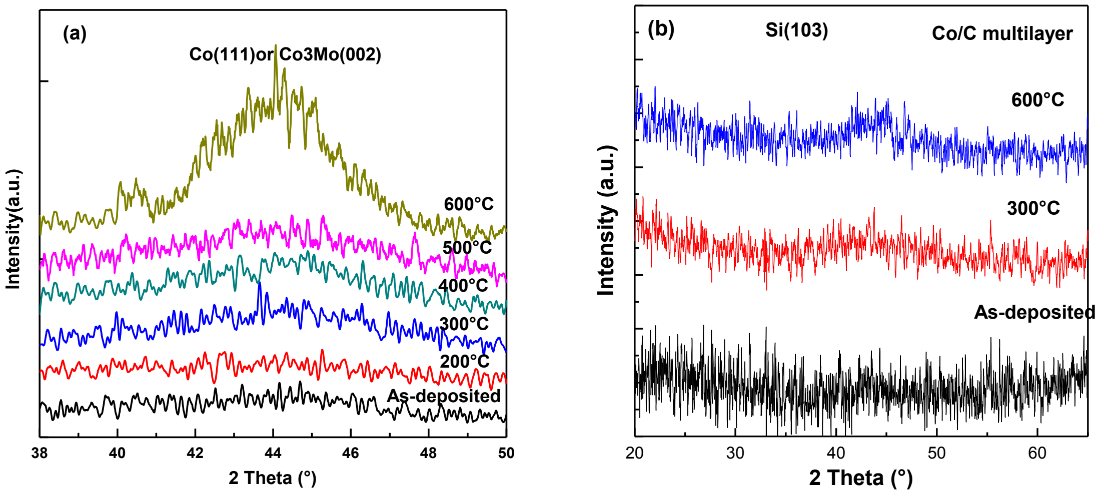

Figure 3.21 Diffraction patterns of the Co/Mo_2C samples: as-deposited, annealed at 200°C, 300°C, 400°C, 500°C and 600°C (a) and of the Co/C multilayers: as-deposited, 300 and 600°C (b).

4) Time of flight-secondary ions mass spectroscopy

Shown in Figure 3.22 are the ToF-SIMS depth profiles of C^- ions of the as-deposited, 300 and 600°C Co/Mo_2C samples. The amplitude of the signal in the middle of the profile is normalized to unity to show the relative contrast of the ion signal. Then, for the sake of clarity, the curves of 300°C and 600°C annealed samples are arbitrarily shifted. The periodic modulation of C^- ions signal gives evidence of the periodic structure of the multilayer. There are only 29 periods for these three samples from the outermost period to the substrate, meaning that the 30th period is chemically modified. At the stack/substrate interface, this period is mixed with the Si substrate and the C^- profile presents a low amplitude signal at the end of the profile.

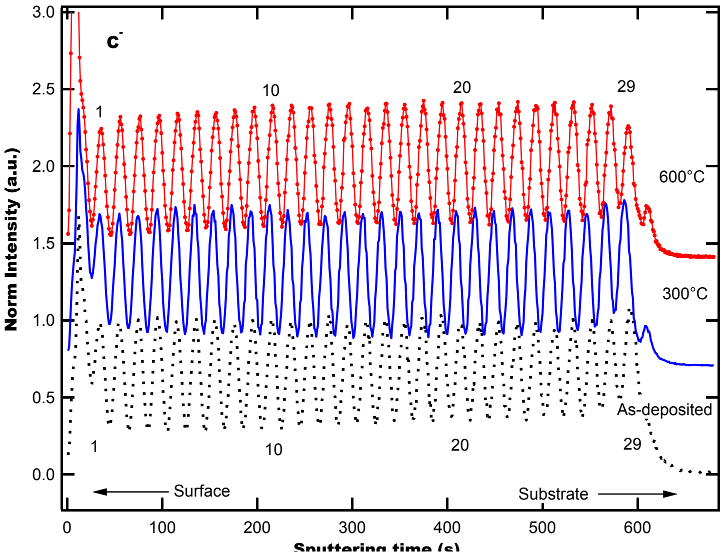

Figure 3.22 ToF-SIMS depth profiles of the C$^-$ ions for the as-deposited, 300°C and 600°C annealed Co/Mo$_2$C samples (Cs$^+$, 1 keV, 59 nA).

The C$^-$, Co$^-$, O$^-$, CoO$^-$, B$^-$ and MoO$_2^-$ profiles toward the air/stack and stack/substrate interfaces for the as-deposited, 300 and 600°C annealed samples are presented in Figure 3.23. From the O$^-$ depth profiles, it can be deduced that oxidation took place at both interfaces. Oxidation at the air/stack interface is due to the atmospheric contamination of the surface layers during storage in air and transfer. Oxidation at the stack/substrate interface is due to the native oxide on the silicon substrate. Similar phenomena were reported in Al/Mo/SiC multilayers [33]. The oxidation of the first Mo$_2$C layer in the stack was also reported by Giglia *et al.* [92] and in the previous section. At the stack/substrate interface, the O$^-$ profile for the 300°C and 600°C annealed samples is sharper than that of the as-deposited sample. This is probably caused by the diffusion of oxygen atoms from the substrate into the stack after annealing. We did not get the information about the combination between O and Mo atoms as no difference in the MoO$_2^-$ profile can be found when the annealing temperature is varied. The oxidation at the stack/substrate interface explains why the 30th period is not well detected.

Furthermore, in the case of as-deposited and 300°C annealed samples, the signal of the CoO$^-$ ions at the air/stack and stack/substrate interfaces is more intense than in that of the 600°C annealed sample. For 600°C annealed sample, the signal of the CoO$^-$ ions is not detected at the air/stack interface. Firstly, this indicates that Co layers are oxidized at temperatures lower than 300°C and that the Co oxide decomposes at high temperature. The C$^-$ and B$^-$ profiles do not show any significant change in the three samples.

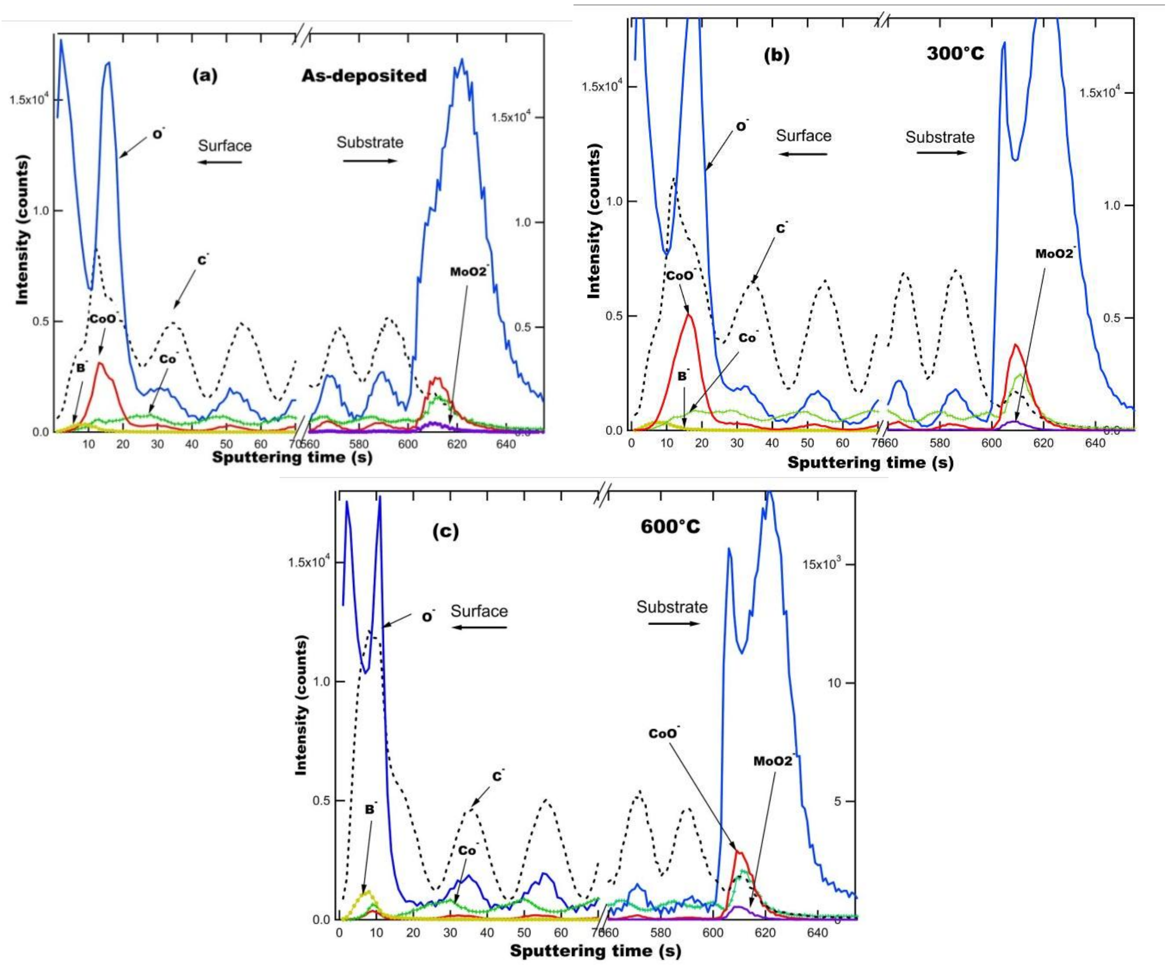

Figure 3.23 ToF-SIMS depth profiles of the C^-, Co^-, O^-, CoO^-, B^- and MoO_2^- ions at the air/stack and stack/substrate interfaces domains for as-deposited (a), 300 (b) and 600°C (c) annealed samples.

Figure 3.24 (a) shows the ToF-SIMS depth profiles of the Co^-, $CoMo^-$ and C^- ions of the 600°C annealed sample. The Mo^- profile follows the C^- profile (not shown). The C^- profile displays a symmetrical shape and is almost in the opposite phase with respect to the Co^- profile. The Co^- depth profile displays some shoulders which correspond to the maxima in the $CoMo^-$ depth profile. This is attributed to a matrix effect since for ultra-thin layers it is not possible to reach a steady sputtering regime before the end of the period. Figure 3.24 (b) shows the comparison of the Co^- and C^- ions profiles of the as-deposited and 600°C annealed samples. Both ions profiles are normalized to unit for the sake of clarity. We cannot observe any significant changes in the Co^- depth profile between as-deposited and 600°C annealed samples. The same situation is recorded for the C^- depth profile except a slightly better contrast for the sample annealed at 600°C with respect to the as-deposited sample.

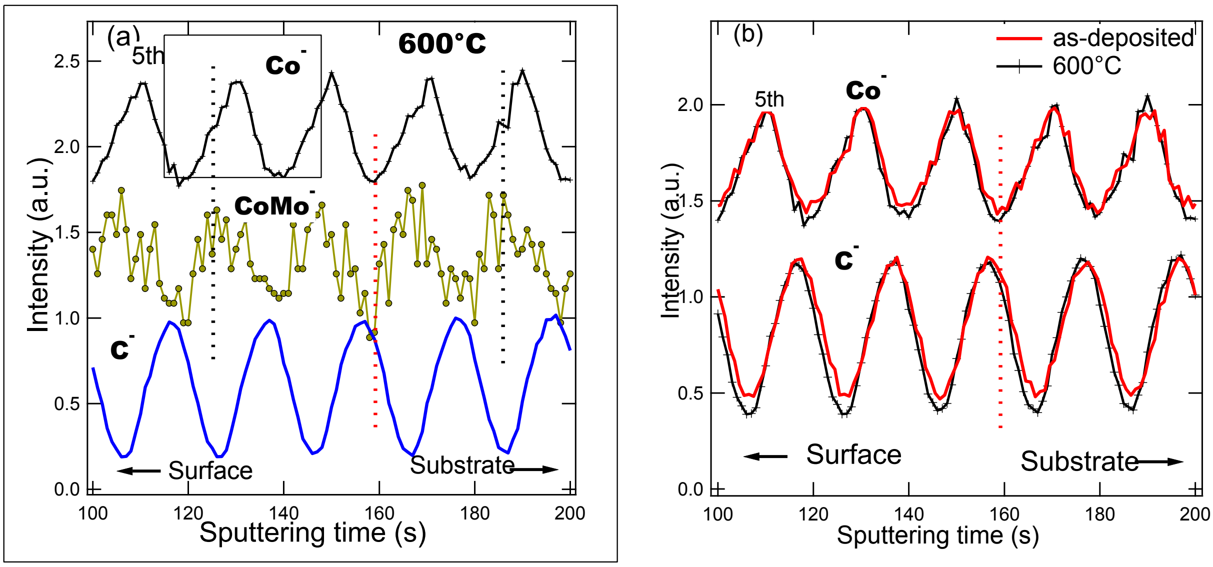

Figure 3.24 ToF-SIMS depth profiles of the Co$^-$, CoMo$^-$ and C$^-$ ions for the 600°C annealed sample (a) and comparison of depth profiles of the Co$^-$ and C$^-$ ions for the as-deposited and 600°C annealed samples (b). ToF-SIMS depth profiles of Co$^-$ and CoMo$^-$ ions are shifted vertically for clarity.

5) Transmission electron microscopy

Figures 3.25 (a) and (b) show the HAADF and bright-field images of the Co/Mo$_2$C as-deposited sample, respectively. The HAADF image shows a nice periodic multilayer structure since the individual layers are smooth. In the bright field image, Co layers appear bright and Mo$_2$C layers dark. We observe the appearance of dark areas in some Co layers, which suggests the presence of some crystallites. In the high-resolution image shown in Figure 3.25 (c), we can observe the lattice fringes within the Co layers and at the interfaces, even if the contrast between Co and Mo$_2$C layers is poor, owing to their close mean atomic number. Selected-area diffraction, shown in Figure 3.25 (d), gives evidence of mainly amorphous structure in the stack. This observation is in agreement with the results of XRD. It is noted that crystallites in the thin film cannot be detected with the XRD technique.

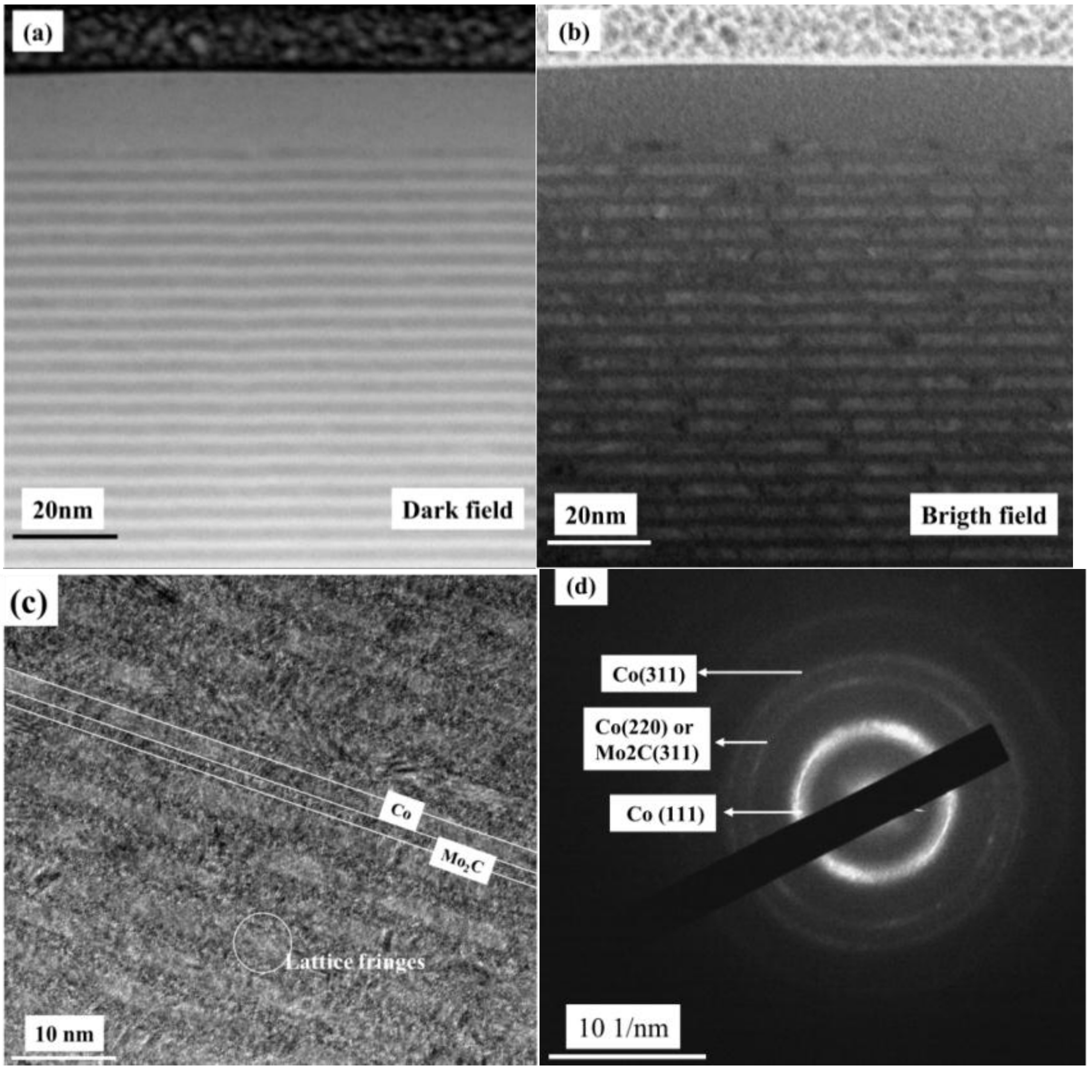

Figure 3.25 Transmission electron microscopy of the Co/Mo_2C as-deposited sample: HAADF (a) and bright field image (b); high-resolution image (c) and selected-area diffraction (d).

3.4.4 Discussion

From the preceding analysis, it follows that the enhancement of ferromagnetic Co signal above 300°C should be primary ascribed to a separation of Co and C atoms at the interfaces. In the Co-C binary phase diagram, there is no stoichiometric compound resulting from the reaction between Co and C [93]. In the Co-Mo binary phase diagram, Co_3Mo, and Co_7Mo_6 (μ and δ phase) are mentioned [94,95]. The Co-C-Mo ternary phase diagram gives two ternary compounds Mo_3Co_3C and Mo_6Co_6C but there is a small possibility for their formation in the Co/Mo_2C multilayer because of their high formation temperature [96]. Otherwise, the XRD results show that no significant Co_3Mo crystallites can be formed from as-deposited to 500°C annealed samples. Therefore, we can deduce that intermixing takes place for the as-deposited and 200°C annealed samples with a limitation of the Co_3Mo compound.

Based on the Miedema's macroscopic atom model [97], we can calculate the mixing enthalpy of the Co-Mo and Co-C systems to confirm our results. The Miedema's atom model is described in appendix I. According to this model, which have been able to calculate the enthalpy values for binary alloys, the calculated mixing enthalpy of Co-Mo system is shown in Figure 3.26. It is always negative. This indicates that the Co and Mo compounds can easily form. Moreover the mixing enthalpy decreases when the mole fraction of Mo changes from 0 to 0.45. However the ratio of atomic fraction between Co and Mo in the Co/Mo_2C multilayer stack is about 3:1 and thus the Mo atomic fraction is 0.25 (according to the designed thickness of each layer). This means that the formation enthalpy of the Co and Mo compound always decreases even if all Co atoms react with all Mo atoms in the Co/Mo_2C multilayer, or in other words, once Co and Mo compounds are formed and they cannot easily separate.

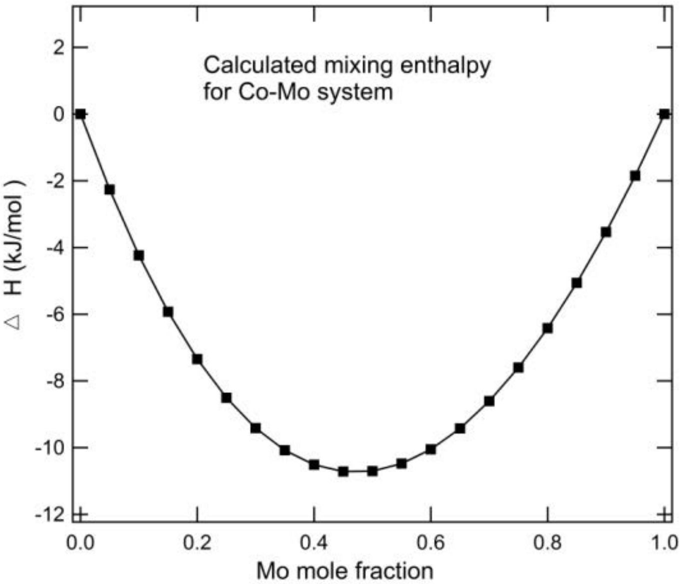

Figure 3.26 Simulated mixing enthalpy of the Co-Mo system.

The loss of the ferromagnetic Co signal in NMR could be ascribed to a disordered mixture at the interface, such as Co_xC_y. Moreover, mixing enthalpy calculations in Ref. [98] indicate that the Co-C system separates easily into two phases. This is testified by the NMR results of the reference Co/C multilayers. From the change of the chemical state of C atoms upon annealing and the increase of ferromagnetic Co signal above 300°C, we should pay attention to the change of formation enthalpy for Mo-C mixing system.

The calculated mixing enthalpy of the Mo-C system is presented in Figure 3.27. We can see that it is negative at C mole fraction below 0.45 and after increases sharply. In the Co/Mo_2C stack, the atomic fraction of Mo to C in the Mo_2C layer is designed to be 2 (C mole fraction is 0.33). That is to say, the Mo_2C compound shows small possibility of phase separation. Moreover the thermal stability of Mo_2C has been already demonstrated [63,99]. Regarding the results mentioned above, we infer that there is a possibility of excess C atoms existing in the multilayer. Actually, this is demonstrated by the x-ray photoemission spectroscopy results of thin film Mo_2C, which gives the atomic ratio of 0.5 between Mo and C atoms, *i.e.* MoC_2.

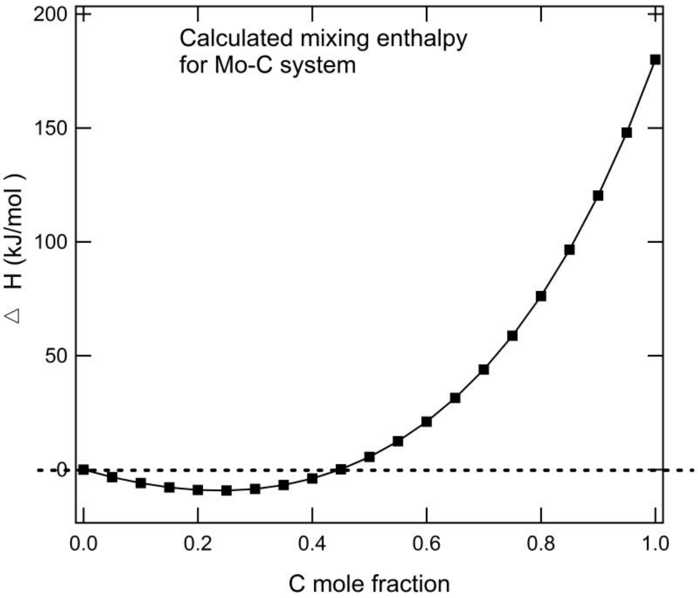

Figure 3.27 Simulated mixing enthalpy for the Mo-C system.

Based on all the described results, we conclude that the Co atoms in the Co layers are mixed with C atoms to form disordered alloy for as-deposited and 200°C annealed Co/Mo_2C samples. After annealing at 300°C and above, Co and C atoms demix from their mixed regions and progress crystallization of Co layers take place upon annealing. However the direction of demixing may not follow the growth direction of thin layers but other directions, such as a direction parallel to the surface. This means that separated Co and C atoms do not necessarily go back to their original layers. This phenomenon explains the decrease of the reflectivity of the multilayer after annealing which is discussed in the Section 3.2.

A scheme of diffuse processing in the Co/Mo_2C multilayer upon annealing is shown in Figure 3.28. In the as-deposited sample, the interdiffusion between Co and C atoms exists at the interfaces. The C atoms diffuse into the Co layer in a disorder way and destroy the pure Co layer. After annealing, the Co and C atoms separate from their mixed region and both atoms show a partial order arrangement, but the C atoms still stay in the Co layer. This explains why we can obtain a ferromagnetic Co signal of the Co/Mo_2C multilayer after annealing by NMR spectroscopy.

Note that the fact that Co and C atoms do not form a compound is in agreement with results of the Section 3.2 where we fitted the EUV data taking into account the formation of Co_xC_y compounds and no improvement was obtained. Therefore the results are not shown in the Section 3.2. This indicates that only a small number of C atoms go into the Co layer and this makes the Co layer lose ferromagnetic Co signal. However the whole periodic structure is not destroyed. The TEM image and ToF-SIMS profile also demonstrate the periodic structure of the multilayer.

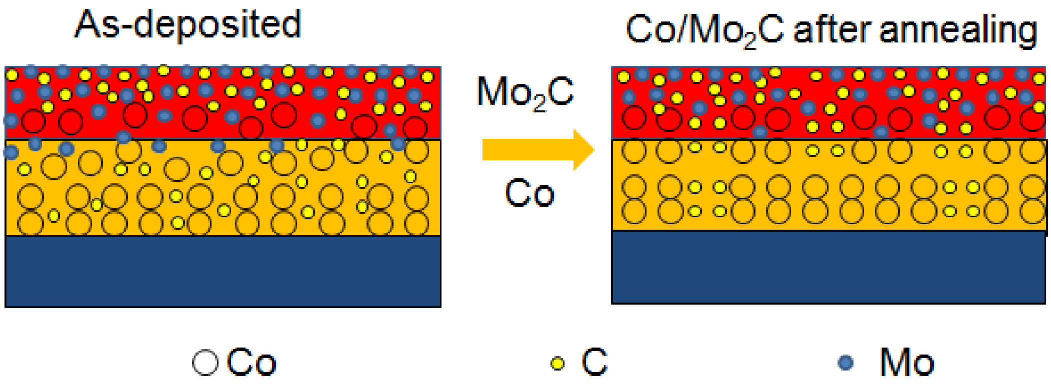

Figure 3.28 Scheme of the diffusion in the Co/Mo_2C multilayer upon annealing.

3.4.5 Conclusions

The interfacial and structural properties of Co/Mo_2C multilayers with annealing were characterized by the XES, NMR, ToF-SIMS, XRD and TEM. The Co/Mo_2C multilayers show a periodic structure, the Co and Mo_2C layers in the stack being mainly amorphous. The formation of oxide layers at both air/stack and stack/substrate interfaces are observed by the ToF-SIMS. According to TEM results, some crystallites are present in the as-deposited samples. The C Kα emission spectra of the Co/Mo_2C multilayers annealed at 400°C and above show a slight broadening with respect to that of the as-deposited sample, suggesting a slightly change of the carbon chemical state. The NMR spectra demonstrate a demixing phenomenon between Co and C in the multilayer stack after annealing. Comparing the NMR spectroscopy results of the Co/Mo_2C multilayers with these of the Co/C reference multilayers, we find that Co and C mix together after deposition and then, after annealing at 300°C and above, Co and C demix from their mixed regions and Co layers show progress crystallization upon annealing. The Miedema's model is used to calculate the mixing enthalpy and accounts for the phenomenon of phase separation of the Co-C system.

Chapter 4 Study of Co/Mo_2C/Y multilayers

In this Chapter, we present the optical performance and interface properties of Co/Mo_2C/Y tri-layer systems upon annealing. Two systems Co/Mo_2C/Y and Co/Y/Mo_2C, are designed for working in the EUV range at near normal incidence. In Section 4.1 we investigate the structural and optical properties of both systems by combing the XRR, NMR and XRD techniques. Two fitting models are used to fit the reflectivity data and explain the changes of the interface width in these systems upon annealing. Section 4.2 presents the TEM observation for both systems after annealing. We analyzed the intensity profiles extracted from the bright field images and obtain information on the interface width.

The contents of this chapter are based on the following papers:

4.1 Yanyan Yuan, Karine Le Guen, Jean-Michel André, Zhanshan Wang, Jingtao Zhu, Christian Mény, Philippe Jonnard.Optical and structural characterization of the Co/Mo_2C/Y system. **Applied Surface Science**. In press.

4.2 Yanyan Yuan, Karine Le Guen, Jean-Michel André, Zhanshan Wang, Jingtao Zhu, Corinne Ulahq, Christian Mény, Philippe Jonnard. Transmission electron microscopy observation of Co/Mo_2C/Y system. In preparation.

4.1 Optical and structural characterization of the $Co/Mo_2C/Y$ system

4.1.1 Introduction

In the Chapter 3 we studied the optical performance of Co/Mo_2C multilayer. In this bi-layer system, we cannot know clearly which interface, Co-on-Mo_2C or Mo_2C-on-Co, has more influence on the optical performance. Thus in order to distinguish the two interfaces contributions and improve the optical performance, we insert a third layer, yttrium, into the Co/Mo_2C multilayer stack. Two types of multilayers are formed: $Co/Mo_2C/Y$ with interfaces Mo_2C-on-Co, Y-on-Mo_2C and Co-on-Y; $Co/Y/Mo_2C$ with interfaces Co-on-Mo_2C, Y-on-Co and Mo_2C-on-Y.

The deposition order of the Y layer in the system cannot only significantly affect the reflectivity but also the interfacial diffusion, as reported in the Co/Mg system with an insertion of Zr layer [48]. The two designed systems $Co/Mo_2C/Y$ and $Co/Y/Mo_2C$ present a theoretical reflectivity of 54% and 11% at near normal incidence, respectively. The reason for the significant difference of reflectivity is the difference of the phase of beam reflected at each interface. By changing the order of the material reflected beams go from a constructive interference scheme to a destructive interference scheme.

4.1.2 Experimental details

The $Co/Mo_2C/Y$ and $Co/Y/Mo_2C$ systems were deposited by direct-current magnetron sputtering. The substrates were sliced and polished Si (100) wafers, with surface roughness of 0.4 nm (*rms*) determined by atomic force microscopy in the range of 10^{-2} to 10 μm^{-1} spatial frequencies. The designed period is 7.71 nm and the thickness of Co, Mo_2C and Y layer was 1.00 nm, 2.67 nm and 4.04 nm, respectively. The base pressure was 10^{-5} Pa before deposition. The working gas was argon (99.999% purity) at a constant working pressure of 0.1 Pa. The number of periods is 30. There were six 10×10 mm^2 substrate sections cleaved from a single wafer for each system. Then six multilayers were deposited separately in the same conditions. The first layer on the substrate for the $Co/Mo_2C/Y$ and $Co/Y/Mo_2C$ systems was the Co and Mo_2C layer, respectively. With our notation, the layers are indicated from the substrate toward the surface. A 3.5 nm-thick B_4C capping layer was deposited to prevent oxidation. Five as-deposited samples of each system were annealed at 200, 300, 400, 500 and 600°C during one hour under high vacuum to study their thermal behaviour.

First these two systems were characterized by the x-ray reflectometry (XRR) using Cu Kα wavelength (0.154 nm) to check their quality. Then we measured the reflectivity with *s*-polarized radiation at the application wavelength of 14.6 nm on the BEAR beamline at the Elettra synchrotron radiation facility [56]. The photon energy was calibrated by the Si $2p_{3/2}$ binding energy at 99.2 eV. The reflectivity curves were obtained at the angle of 4° off-normal incidence. We also performed the zero-field NMR spectroscopy for these samples. To identify the phase present in our systems as a function of the annealing temperatures, we performed x-ray diffraction of the $Co/Mo_2C/Y$ (as-deposited, 300 and 600°C) and $Co/Y/Mo_2C$ (as-deposited) samples with Cu Kα radiation (0.154 nm).

4.1.3. Results and discussion

1) X-ray reflectometry at 0.154 nm

We show in Figure 4.1 the XRR curves of the $Co/Mo_2C/Y$ and $Co/Y/Mo_2C$ systems before and after annealing. Six well-defined peaks are observed for both systems, indicating that these multilayers possess a well-defined periodic structure. After 400°C annealing the peak positions of the $Co/Mo_2C/Y$ multilayers shift toward high angles, which implies a period decrease according to the Bragg law. Concerning the $Co/Y/Mo_2C$ systems, it is observed that the Bragg peak position of the 600°C annealed sample significantly shift toward high angles.

We performed the fit of the XRR data with Bede Refs software (genetic algorithm) [55] using a tri-layer model (no interlayer is taken into account). A good agreement between fitted and experimental curves is obtained. As an example, we show in Figure 4.2 the results for the $Co/Mo_2C/Y$ multilayers as-deposited and annealed at 600°C. The structural parameters are listed in Table 4.1, except density. The density ratio, which is the density of the layer with respect to the bulk value, is determined with a 15% uncertainty and within this uncertainty there is no significant density change as a function of annealing. The period variation of each sample is plotted in Figure 4.3 as a function of the annealing temperature. Δd represents the period change before and after annealing. It can be seen that the period change of the $Co/Mo_2C/Y$ system decreases quickly with temperature and then increases gently from 400°C. The period of the $Co/Y/Mo_2C$ system decreases gradually upon annealing. Both systems show compressed periods after annealing. This phenomenon can be explained by the interdiffusion between two layers with the formation of compounds. Moreover the crystallization induced by annealing can also effect the variation of period.

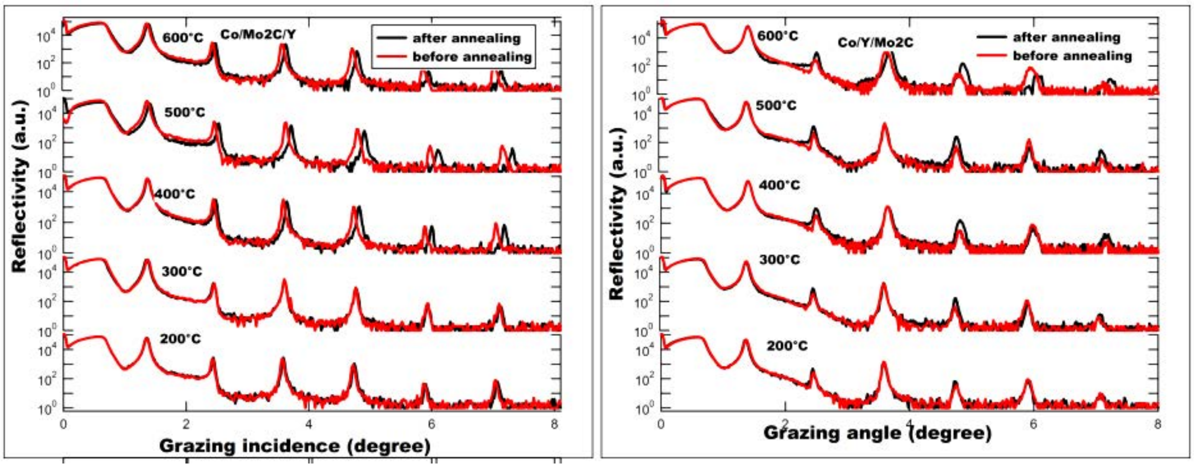

Figure 4.1 Reflectivity curves at 0.154 nm of the Co/Mo$_2$C/Y and Co/Y/Mo$_2$C systems before and after annealing as a function of the grazing angle. For the sake of clarity, spectra of the sample annealed at 200, 300, 400, 500 and 600°C as well as corresponding as-deposited samples are shifted vertically.

Table 4.1 Structural parameters extracted from the fit of the XRR curves measured at 0.154 nm.

T/°C	Sample	Period / nm Before /after annealing	Thickness / roughness nm (±0.05 nm)			
			B$_4$C	Co	Mo$_2$C	Y
200°C	Co/Mo$_2$C/Y	7.56 / 7.55	3.02	2.00/1.00	1.32/0.33	4.23/0.29
	Co/Y/Mo$_2$C	7.52 / 7.55	3.96	0.89/0.55	2.91/1.03	3.75/0.30
300°C	Co/Mo$_2$C/Y	7.52 / 7.48	3.48	1.21/0.33	2.06/0.31	4.21/0.31
	Co/Y/Mo$_2$C	7.55 / 7.55	3.60	1.99/0.62	1.39/1.30	4.17/0.30
400°C	Co/Mo$_2$C/Y	7.59 / 7.39	3.77	0.90/0.12	2.22/0.26	4.27/0.72
	Co/Y/Mo$_2$C	7.41 / 7.41	3.37	1.91/0.44	1.31/0.97	4.19/0.38
500°C	Co/Mo$_2$C/Y	7.55 / 7.37	3.55	1.05/0.04	2.15/0.28	4.17/0.68
	Co/Y/Mo$_2$C	7.52 / 7.49	3.76	1.26/0.41	2.04/0.94	4.19/0.30
600°C	Co/Mo$_2$C/Y	7.59 / 7.46	3.10	1.94/0.96	1.38/0.33	4.14/0.36
	Co/Y/Mo$_2$C	7.46 / 7.37	3.90	1.70/0.31	1.71/0.12	3.96/0.67

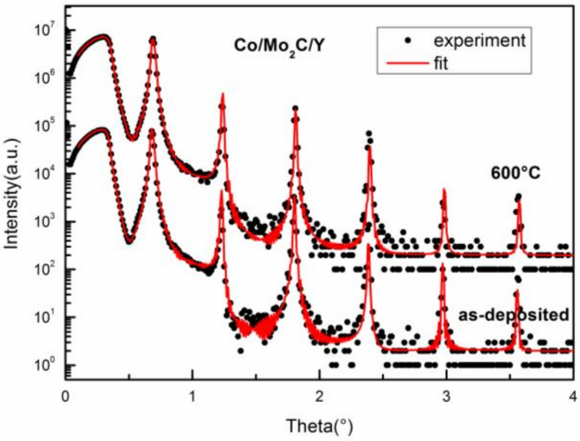

Figure 4.2 Comparison of experimental and fitted data of the as-deposited and 600°C annealed Co/Mo$_2$C/Y samples. Curves of 600°C annealed sample are shifted vertically for the sake of clarity.

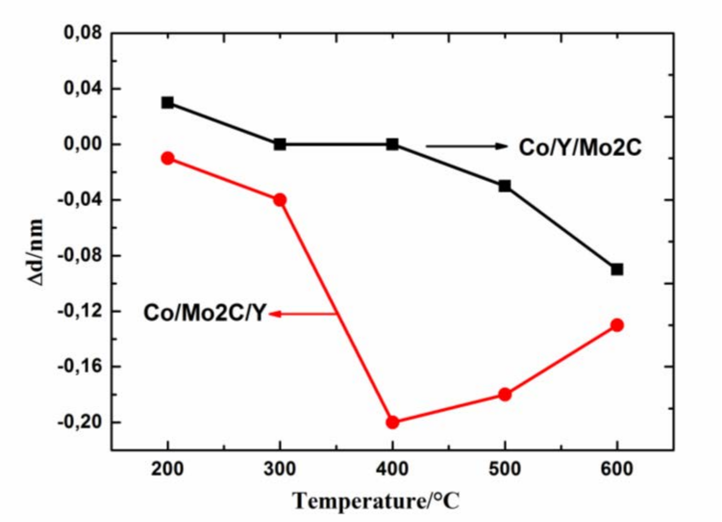

Figure 4.3 Variation Δd of the period of the Co/Mo_2C/Y and Co/Y/Mo_2C systems upon annealing with respect to the value of the as-deposited sample.

2) Extreme ultra-violet reflectivity with synchrotron radiation

Shown in Figure 4.4 (a) and (c) are the reflectivity measurements of the two systems performed at the application wavelength of 14.6 nm for as-deposited and annealed at 300 and 600°C samples. In Figure 4.4 (b) and (d) we present the evolution of the reflectivity values as a function of the annealing temperature. As can be seen the Co/Mo_2C/Y multilayer achieves a reflectivity of 27.5% with as-deposited sample; after annealing the reflectivity linearly decreases to 17% at 600°C. The reflectivity of the Co/Y/Mo_2C system is low, less than 2.5%. This value is about 4 times smaller than the theoretical reflectivity (about 11%). One reason for the loss of reflectivity may be the high sensitivity of Y to atomic oxygen: present in the vacuum system during deposition. Montcalm [100]pointed that when the base pressure is above 10^{-6} Pa, oxygen contamination of the Y layer leads to a decrease of reflectivity 3.2% with respect to the value obtained with a base pressure of 10^{-8} Pa. In addition the deposition order of the Y layer is an important factor, which can cause an asymmetrical interface width. It should be noted that the reflectivity of the Co/Y/Mo_2C sample increases slightly after 400°C. This could be related to the creation of compound or mixtures which changes the optical contrast in the stack.

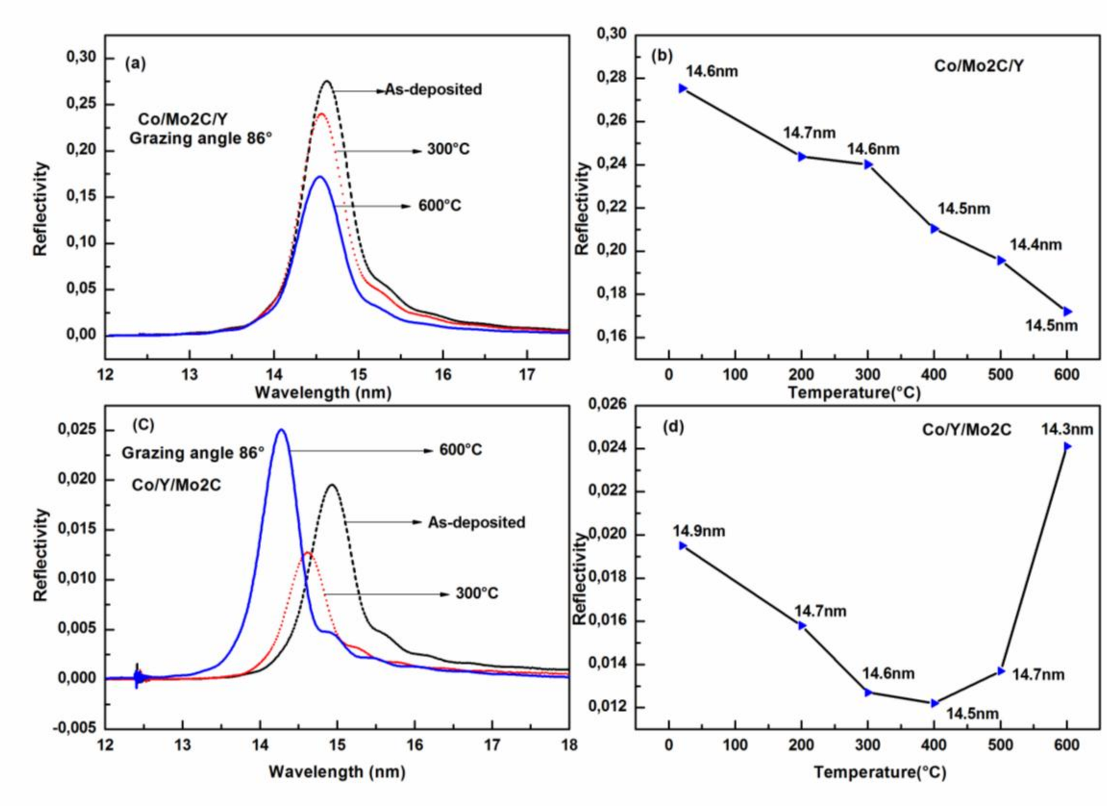

Figure 4.4 (a) and (c) EUV reflectivity of the Co/Mo$_2$C/Y and Co/Y/Mo$_2$C systems respectively at near normal incidence. (b) and (d) evolution of the reflectivity peak as a function of the annealing temperature. The wavelengths indicated in (b) and (d) correspond to the position of the maxima of the reflectivity curves.

To estimate the interface widths, we first use a tri-layer model to fit the EUV experimental data for both systems, meaning that we are considering only Co, Mo$_2$C, Y layers in one period. The resulting fitted reflectivity curves of the as-deposited, 300°C and 600°C annealed samples for both systems are presented in Figure 4.5. Table 4.2 lists the interface widths (δ) and periods, as well as the interface widths derived from the XRR data. Note that δ represents the total interface widths with contributions from both local interdiffusion and interfacial roughness.

Comparing the parameters extracted from the XRR and EUV data, it is found that the periods derived from EUV data are larger than those given by the XRR (for all samples, fluctuation of 0.2 to 0.3 nm). In addition, the interface widths derived from the EUV data are much larger than those derived from XRR data. This can be explained by considering that photons with different wavelengths respond to different effective roughnesses on the respective spatial frequency scales. Moreover the availability of accurate optical constant in the EUV spectral range is limited, so it is difficult to obtain precise values for the structural parameters.

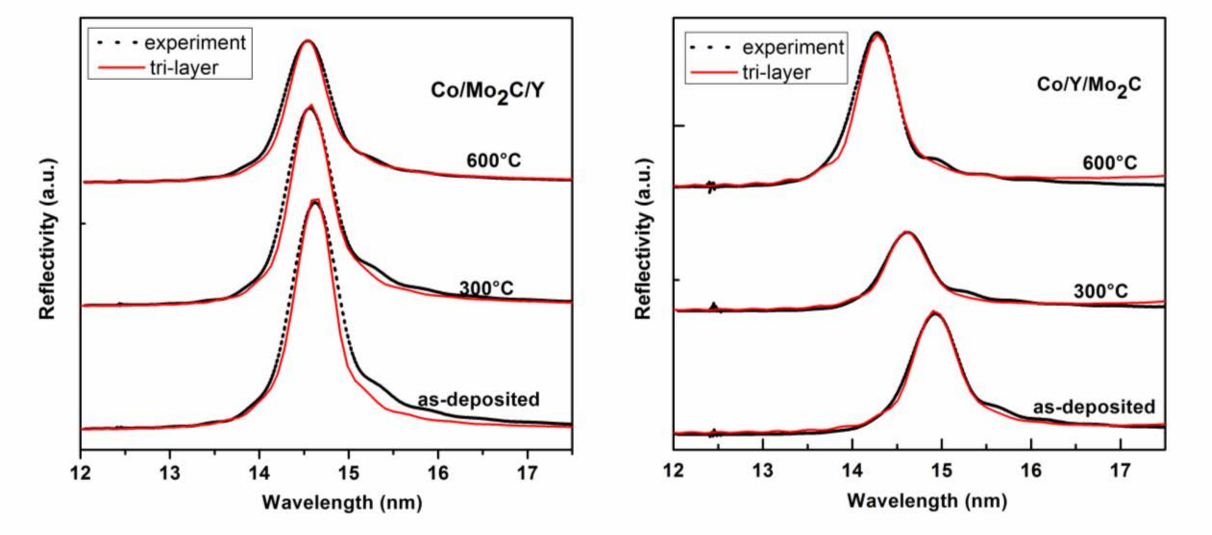

Figure 4.5 Comparison of experimental and fitted data for as-deposited, annealed at 300 and 600°C of the Co/Mo_2C/Y and Co/Y/Mo_2C systems. The incident angle is at 4° from normal.

Table 4.2. Interface widths (δ), period and thicknesses of the Co/Mo_2C/Y and Co/Y/Mo_2C systems (as-deposited and annealed at 300 and 600°C) fitted with tri-layer model. The uncertainty of interface width is about 0.05 nm.

T/°C	Sample	Period/nm	$\delta_{Co\text{-}on\text{-}Mo2C}$ $\delta_{Y\text{-}on\text{-}Co}$ $\delta_{Mo2C\text{-}on\text{-}Y}$ / nm EUV/XRR	$\delta_{Mo2C\text{-}on\text{-}Co}$ $\delta_{Co\text{-}on\text{-}Y}$ $\delta_{Y\text{-}on\text{-}Mo2C}$ / nm EUV/XRR	d_{Co}/nm	d_{Mo2C}/nm	d_Y/nm
As-deposited	Co/Mo_2C/Y	7.76	-- -- --	1.05 / 0.98 0.65 / 0.30 1.65 / 0.35	1.20	2.61	3.95
	Co/Y/Mo_2C	7.97	1.15 / 0.95 1.30 / 0.57 1.26 / 0.39	-- -- --	1.30	2.67	4.00
300°C	Co/Mo_2C/Y	7.74	-- -- --	0.94 / 0.33 1.30 / 0.31 1.15 / 0.31	1.24	2.53	3.97
	Co/Y/Mo_2C	7.77	1.00 / 1.30 1.27 / 0.62 1.27 / 0.30	-- -- --	1.32	2.50	3.95
600°C	Co/Mo_2C/Y	7.74	-- -- --	1.00 / 0.96 2.00 / 0.36 1.30 / 0.33	1.20	2.59	3.95
	Co/Y/Mo_2C	7.56	1.00 / 1.20 1.01 / 0.31 1.33 / 0.67	-- -- --	1.23	2.38	3.95

The evolution of interface widths upon annealing allows assessing the thermal stability of the multilayers. The interface widths of the Mo_2C-on-Co and Co-on-Mo_2C interfaces derived from XRR and EUV data for all samples are close to the thickness of the Co layers (designed to be 1.0 nm), those values derived from XRR data are larger than that of the Y-on-Co, Co-on-Y, Mo$_2$C-on-Y and Y-on-Mo$_2$C interfaces. This implies that the Co layers are probably mixed completely with other layers to form compounds or mixtures in the stack. In addition, based on fitted parameters from the EUV data for the Co/Mo$_2$C/Y multilayer, the $\delta_{\text{Mo2C-on-Co}}$ value stays close to 1.0 nm while $\delta_{\text{Co-on-Y}}$ value increases upon annealing and the $\delta_{\text{Y-on-Mo2C}}$ value slightly decreases upon annealing. At the opposite, in the Co/Y/Mo$_2$C multilayer, the three values of interface width δ do not significantly depend on annealing: this indicates that the interdiffusion strongly takes place at the deposition time and thus there is no more evolution of interdiffusion as a function of annealing temperature. This also illustrates that the diffusion at the Y-on-Co and Mo$_2$C-on-Y interfaces in the Co/Y/Mo$_2$C multilayer is easier than at the Co-on-Y and Y-on-Mo$_2$C interfaces in the Co/Mo$_2$C/Y multilayer.

3) Zero-field nuclear magnetic resonance spectroscopy

NMR spectra of the Co/Mo$_2$C/Y as-deposited sample and two references, Co$_3$Mo and CoMo1% (atomic ratio) disordered alloys, are presented in Figure 4.6. All spectra are normalized to their integrated area. The spectra of the samples annealed from 200 to 600°C for the Co/Mo$_2$C/Y and Co/Y/Mo$_2$C systems show no signal (and thus, not are shown here). The multilayer NMR spectrum shows no bulk Co peak (intense peak at 217 MHz for *fcc* Co) but only a low frequency signal (<200 MHz). This demonstrates that the Co layers are strongly mixed with the other atoms of the multilayer stack. In order to probe the influence of the vicinity of Mo atoms on the resonance frequency of Co we have measured the reference sample CoMo1%. As in Ref. [90,101] the peak at 176 MHz is attributed to the presence of one Mo atom within the 12 first neighbors of a *fcc* Co atoms. This shows that the frequency shift due to the presence of Mo atoms is very strong and explains why the NMR signal obtained for the multilayer is mainly found at rather low frequencies. It can be seen that the spectrum of the Co/Mo$_2$C/Y as-deposited sample is very close to the one of bulk Co$_3$Mo disordered alloy. These observations strongly suggest that the Co layers are fully mixed with Mo and that the Mo concentration in Co is of the order of 25at%. But we cannot get a conclusive result: indeed if the Co atoms were totally surrounded by other atoms such as Y atoms, no ferromagnetic signal would also be measured. At the present time, NMR spectra of Co_xY_y compounds are unavailable.

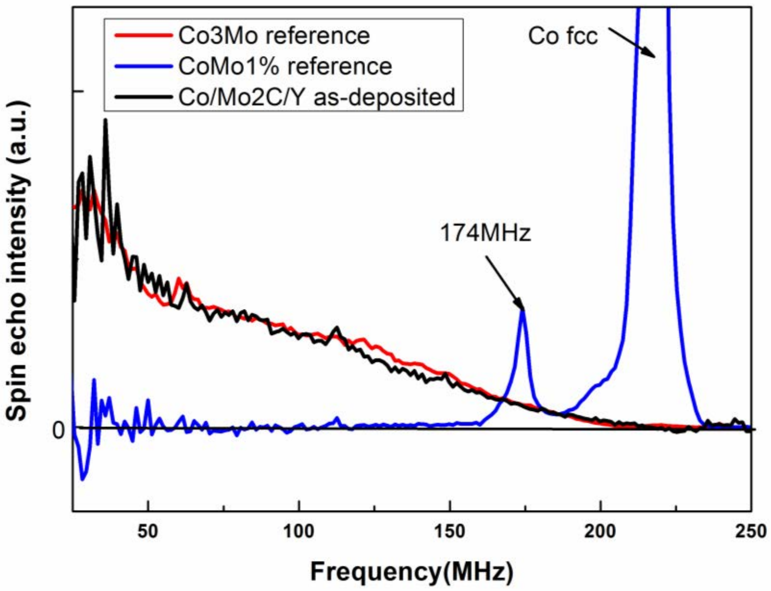

Figure 4.6 NMR spectra of the Co/Mo$_2$C/Y as-deposited sample and two reference samples Co$_3$Mo and CoMo1% (atomic ratio) disordered alloys.

4) X-ray diffraction

The XRD patterns of the Co/Mo$_2$C/Y as-deposited, 300 and 600°C samples and the Co/Y/Mo$_2$C as-deposited samples are presented in Figure 4.7. A series of weak peaks are detected in the 2θ=10-80° range for the Co/Mo$_2$C/Y multilayer. The peak at 30° probably corresponds to Y (002) [53,102,103] or Co$_3$Mo (101). It is found that the intensity of this peak decreases upon annealing, no peak shift being observed, which indicates that the pure Y layers react upon annealing with atoms from the others layers. Another possible reason for the decrease of the pure Y intensity is the interfacial diffusion during the annealing or amorphous phase formation. The peak at 44° may be the combination of several phases, *i.e.* Co$_3$Mo (002) or Co$_2$Y (222) or Co$_5$Y (111) phase. The peak at 49° may correspond to MoC (101). The compounds produced from Mo and Y are not easy to form because of their positive heat of mixing being +26 kJ/mol [104] and consequently we exclude this possibility. From NMR spectra, we know that there is no pure Co layer left in the stack and the NMR spectrum of the Co/Mo$_2$C/Y as-deposited sample is the same as that of the Co$_3$Mo reference. Hence we assume that the Co$_3$Mo disordered alloy is formed at the interfaces. However, the combination of the Co and Y atoms is also possible. The peaks around at 40° and 48° are unidentified. The Co/Y/Mo$_2$C as-deposited sample does not show intense peaks: this sample is mainly amorphous.

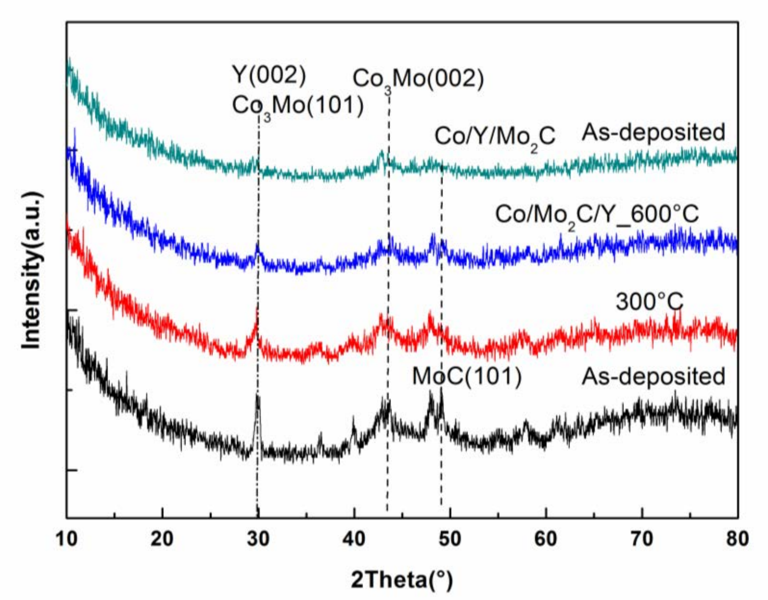

Figure 4.7 X-ray diffraction patterns of the Co/Mo$_2$C/Y as-deposited, 300 and 600°C samples and the Co/Y/Mo$_2$C as-deposited sample.

4.1.4 Discussion

From XRD and NMR results, a four-layer model is proposed to fit the EUV reflectivity data. An interfacial reaction is considered and the model structure is designed as Si/[Co$_3$Mo/MoC/Y/Co$_2$Y]$_{30}$/Y$_2$O$_3$/YC$_2$/B$_4$C and Si/[Co$_2$Y/Y/MoC/Co$_3$Mo]$_{30}$/B$_4$C for the Co/Mo$_2$C/Y and Co/Y/Mo$_2$C multilayers respectively. The fitting procedure is performed using the Levenberg-Marquardt (MINIPACK-1) algorithm within IMD software [1]. The thickness of the Y$_2$O$_3$ and YC$_2$ layers is assumed to be 1.0 nm. We used the density of bulk Co$_3$Mo, Co$_2$Y, Y$_2$O$_3$ and YC$_2$ in the fits. Original Mo$_2$C layers are modified as MoC layers due to the Co$_3$Mo formation. The parameters (thickness and interface width) derived from these fits are collected in Table 4.3 for the Co/Mo$_2$C/Y system. Figure 4.8 (a) shows the resulting fitted spectra compared to those measured for the Co/Mo$_2$C/Y (as-deposited and annealed samples at 300 and 600°C). With respect to tri-layer model, this new set of fitted reflectivity curves including surface oxidation layer and interlayers exhibits a slight improvement, especially for as-deposited sample.

The interface widths are large with respect to the thickness of the Co$_3$Mo and Co$_2$Y layer. Let us consider the atomic number per mole N_i

$$N_i = N_0 \frac{\rho_i \cdot s_i \cdot d_i}{M_i} \tag{4.1}$$

where N_0 is the Avogadro number, ρ_i the layer density, s_i the area of each layer, d_i the thickness of each layer and M_i the atomic weight and subscript i represents the type of the atom. We can obtain the atomic ratio n from

$$n = {}^{N_i}\!/_{N_j} \tag{4.2}$$

where i and j represent the different atoms. Taking the Co/Mo$_2$C/Y 600°C annealed sample as an example, the thickness of Co, Mo$_2$C and Y layer being 1.94 nm, 1.38 nm and 4.14 nm, respectively (see Table 4.1), the atomic ratios of Co to Mo and Co to Y are 2.4 and 1.4, respectively. This means that only a small amount of the Co$_3$Mo and Co$_2$Y compounds can be formed by consuming the whole Co layers in one period.

In the case of the Co/Y/Mo$_2$C multilayer, the fitted spectra with the four-layer model are worse than that obtained from the tri-layer model (not shown here). In addition it is mentioned that there is no peak found in the XRD pattern. This means that there is no (or few) crystalline phase in the stack. However one possibility could exist: the formation of different compounds. Thus a new model, Si/[Co$_2$Y/Y$_2$C/MoC]$_{30}$/B$_4$C, is proposed for fitting the EUV reflectivity data of the Co/Y/Mo$_2$C multilayer. The comparison of experimental and fitted (tri-layer and a new model) reflectivity curves of the Co/Y/Mo$_2$C multilayer (as-deposited and annealed at 300 and 600°C) are shown in the Figure 4.8 (b). One can see that the fitted curves obtained by using both models are close to the experimental curves. The parameters of each layer are listed in the Table 4.3. The results show that the thickness of the MoC and Y$_2$C layer are stable and that of the Co$_2$Y varies upon the annealing. Furthermore, the interface width of the MoC-on-Y$_2$C is very close the Y$_2$C thickness. This indicates that a strong interdiffusion takes place at the interfaces.

The two different fitting models of the Co/Mo$_2$C/Y and Co/Y/Mo$_2$C systems give a good agreement with respect to the experimental data. This indicates that the formation of compound or solid solution is dependent on the deposition order of the layers and also shows that the formation of Co$_3$Mo is located at the Mo$_2$C-on-Co interface rather than at the Co-on-Mo$_2$C interface.

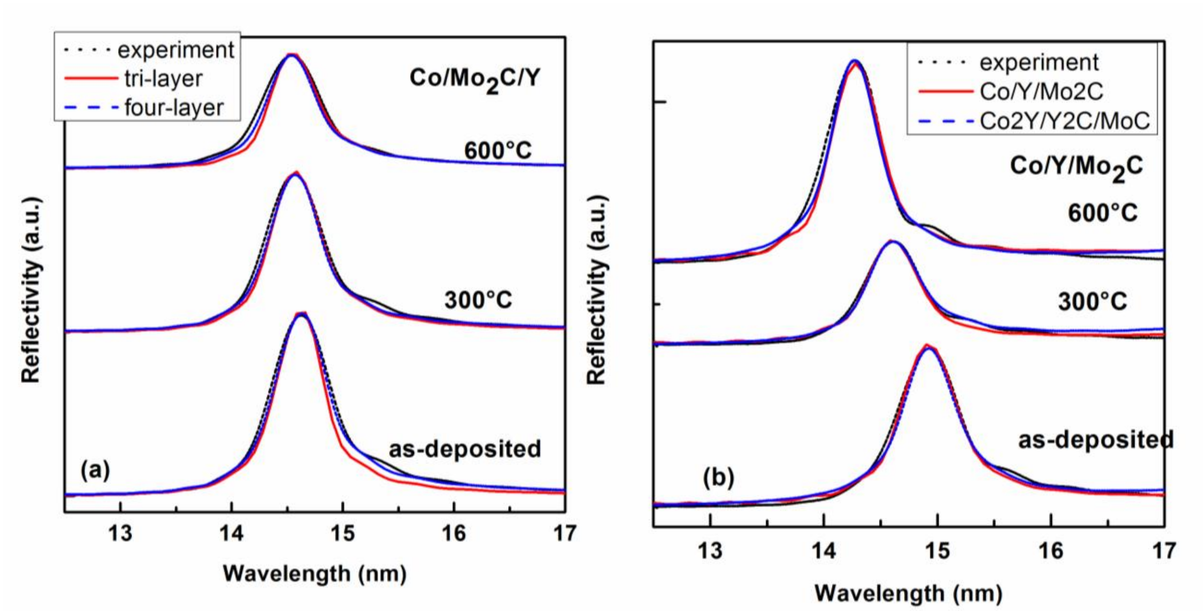

Figure 4.8 (a) Comparison of experimental and fitted (tri- and four-layer models) reflectivity curves of the $Co/Mo_2C/Y$ multilayer (as-deposited and annealed at 300 and 600°C) and (b) comparison of experimental and fitted (tri-layer and the new model) reflectivity curves of the $Co/Y/Mo_2C$ multilayer (as-deposited and annealed at 300 and 600°C).

Table 4.3 Parameters of four-layer model to fit the $Co/Mo_2C/Y$ multilayer and of tri-layer model to fit the $Co/Y/Mo_2C$ multilayer.

Sample		Thickness / interface width /nm (±0.10 nm)			
		Co_3Mo	MoC	Y	Co_2Y
$Co/Mo_2C/Y$	As-deposited	1.50 / 0.60	2.10 / 0.84	3.05 / 0.70	1.10 / 0.50
	300°C	1.50 / 0.80	2.10 / 1.02	3.12 / 0.85	1.01 / 0.50
	600°C	1.50 / 0.85	2.06 / 1.62	3.05 / 1.00	1.10 / 0.50
			MoC	Y_2C	Co_2Y
$Co/Y/Mo_2C$	As-deposited		2.00 / 0.30	2.25 / 2.00	3.72 / 0.38
	300°C		2.00 / 0.30	2.25 / 2.00	3.52 / 1.15
	600°C		2.00 / 0.30	2.00 / 2.00	3.57/ 0.30

4.1.5 Conclusions

The optical and interfacial properties $Co/Mo_2C/Y$ and $Co/Y/Mo_2C$ systems were investigated by a combination of reflectivity, XRD and NMR measurements. The results showed that the $Co/Mo_2C/Y$ multilayers present a well-defined periodic structure; a peak reflectivity of 27.5% at 14.6 nm at near normal incidence in the extreme ultraviolet was obtained, while the $Co/Y/Mo_2C$ multilayer showed a poor reflectivity 2.5%. NMR spectra results showed that there is no pure Co layer left in the stack since the Co layers are strongly mixed with other layers in both systems. XRD patterns indicate that the crystalline phases in the $Co/Mo_2C/Y$ multilayer are different from that in the $Co/Y/Mo_2C$ multilayer.

Based on the NMR and XRD results, we fitted the EUV data using different models for two systems which take into account the formation of the Co_3Mo, Co_2Y and Y_2C compounds or solid solution. The Si/[Co_3Mo/MoC/Y/Co_2Y]$_{30}$/Y_2O_3/YC_2/B_4C model to fit the Co/Mo_2C/Y multilayer and the Si/[Co_2Y/Y_2C/MoC]$_{30}$/B_4C model to fit the Co/Y/Mo_2C multilayer obtained the best agreement with the experiment spectra. Comparison of those fitted results showed that the interdiffusion accompanied with the formation of compounds or solid solution is responsible for the degradation of the reflectivity. These two systems with different interfaces orders probably show the formation of different compounds or solid solutions.

4.2 Transmission electron microscopy observation of $Co/Mo_2C/Y$ system

4.2.1 Introduction

The accurate observation of the interfacial structure in a multilayer stack is necessary for improving the optical performance. An estimation of the interface width is generally provided by the fit of hard x-ray reflectivity data. Cross-sectional transmission electron microscopy can reveal the microstructure of the multilayers. Kessels [105] has reported that the interface roughness, interlayer and the distribution of component in the multilayer can be accurately estimated based on the analysis of the cross-sectional transmission electron microscopy image.

In this part, we focus on the interfaces of the $Co/Mo_2C/Y$ and $Co/Y/Mo_2C$ tri-layer multilayers. Using transmission electron microscopy and scanning transmission electron microscopy (STEM) as well as energy dispersive spectrometry obtained in the STEM mode, we observe the interface change in both systems. Intensity profile extracted from the bright field image is used to analyze the interface width. We compare the interface behavior of each system annealed at 300 and 600°C.

4.2.2 Experimental details

The preparation of sample cross-section has been described in the Chapter 2. The lamellas of the cross-section of the $Co/Mo_2C/Y$ multilayers were measured. The STEM images were generated by scanning the focused beam. High angle-annular dark field (HAADF) image can be obtained simultaneously with bright field image, which known as Z-contrast image. EDS was performed when working in the STEM mode and used to confirm the constituent of each layer in one period. In-depth intensity profiles along the layers were extracted from the bright field images in a rectangle plot by using Digital Micrograph software to obtain the interface information. The thickness of periods and interfacial widths were estimated through the intensity profile by the rule of 15-85%.

4.2.3 Results and discussion

1) Scanning transmission electron microscopy

Shown in Figure 4.9 are the HAADF images of the $Co/Mo_2C/Y$_as-deposited, 300°C and 600°C, $Co/Y/Mo_2C$_300°C and 600°C annealed samples. All samples show a periodic structure. About Co/Mo_2C/Y multilayer, for the as-deposited sample, we can see a sharp contrast at the interfaces in the Figure 4.9 (a). After annealing at 300°C, the interfaces show no sharp contrast. This means that interdiffusions take place between layers and decrease the Z-contrast. However at 600°C, the contrast at interfaces becomes clear. This suggests a slight increase of Z-contrast between layers. For the Co/Y/Mo_2C_300 and 600°C multilayers, layers present sharp Z-contrast and clear interfaces, shown in Figure 4.9 (d) and (e). There are no significant change of interfaces between 300 and 600°C annealed samples.

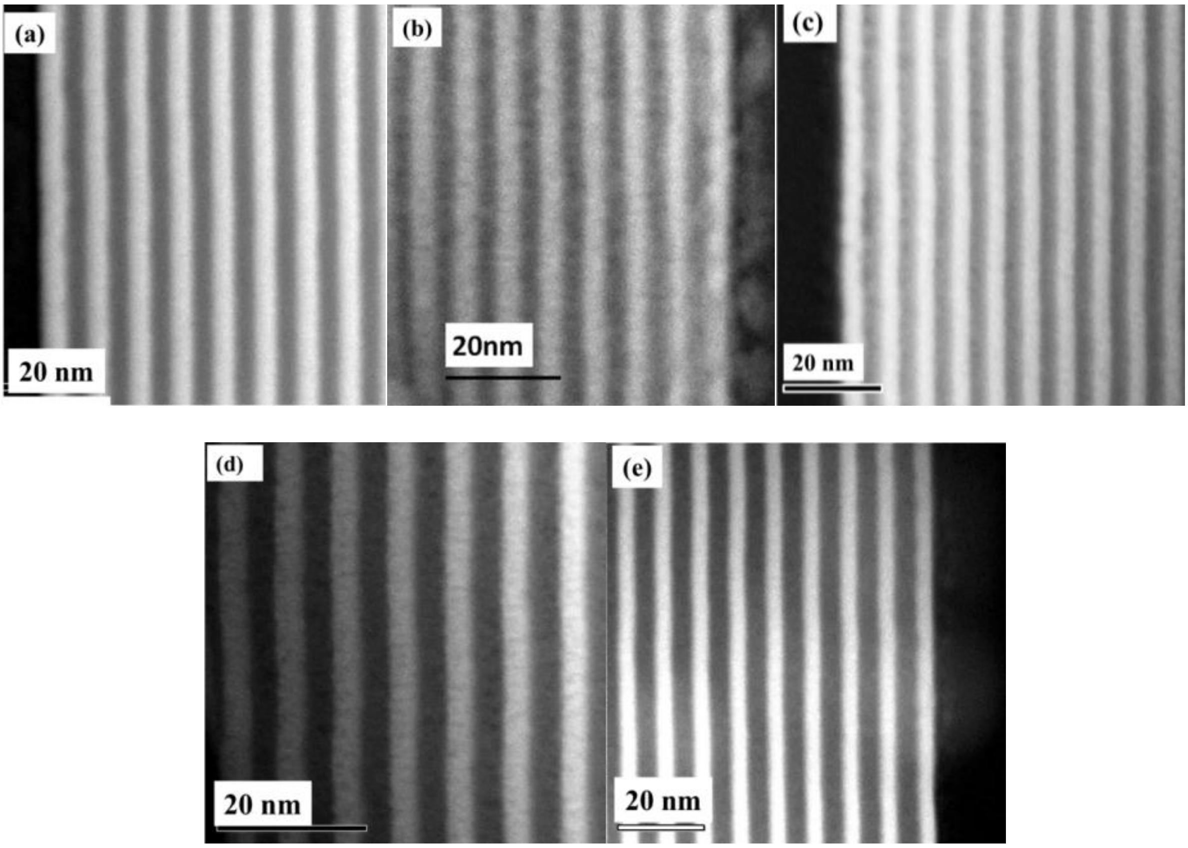

Figure 4.9 HAADF images of the multilayer samples: Co/Mo_2C/Y_as-deposited (a) and Co/Mo_2C/Y_300°C (b), Co/Mo_2C/Y_600°C (c), Co/Y/Mo_2C_300°C (d), Co/Y/Mo_2C_600°C (e).

In the HAADF image, the contrast depends on the average atomic number of the element, the bright regions correspond to the high atomic number element. In our case, the average atomic number of Co, Mo_2C and Y is 27, 30 and 39, respectively. Thus if no interaction between layers take place the bright regions should indicate the Y layers in the stack. In the Co/Mo_2C/Y system the deposition order of layers from the substrate are Co, Mo_2C, Y and Mo_2C, Co, Y for the Co/Y/Mo_2C system. Therefore the first bright regions should correspond to the Co and Mo_2C layers and the dark region should indicate the Y layer. The reason for this reverse contrast is probably due to the interdiffusion with formation of some compounds. We find that the all multilayer stacks only have two layers in one period. This is not in agreement with designed structure tri-layers in one period. This suggests that strong intermixing takes place between two layers of them and changes the average atomic number. In the Section 4.1, we have mentioned that both systems show a slight improvement for fitting the extreme ultraviolet reflectivity data at application wavelength when taking into account interdiffusion and creation of interfacial compound.

2) In-depth intensity profiles

We extract the in-depth intensity profile of multilayers along a few periods from the bright field image of each sample. They are shown in Figure 4.10. The intensity of in-depth intensity profile is related to the density of material and thickness of sample. Variations of peak intensity are observed and caused by a variation of thickness of the cross-sectional lamella samples when thinning them by using ion milling. All the maxima are normalized to unity. Peaks correspond to the bright layer which is the position of Y layers in the stack. The period thickness is determined by calculating the distance between two peaks. In order to minimize the aberration, we take the average value obtained over almost all the periods of stack. Hence, the thickness of one period is listed in Table 4.4. Comparing the fitted period value derived from the hard x-ray reflectivity data; these results show a slight variation.

To obtain the detailed information of each layer in one period and interface between layers, in-depth intensity profile of one period is magnified and shown in Figure 4.10 (b), (d), (f), (h), (j) for all samples. The thickness of bright region can be determined by calculating the full width at half maxima in the intensity profile. The thickness value is also listed in Table 4.4. These values are close to the designed thickness of Y layer. The Mo_2C and Co layers in all samples mixed and thus cannot be discerned. The thickness of these mixed layers is obtained by subtracting the Y layer thickness from the period, see Table 4.4. These values are slightly difference from the fitted values derived from the XRR data.

In-depth intensity profiles of all samples exhibit an asymmetric shape and can be used to obtain the interface width. For the Co/Mo_2C/Y_as-deposited multilayer, the interface width of the Y-on-Mo_2C is determined to be 1.12 nm and slightly smaller than that of Co-on-Y interfaces 1.33 nm. The interface width of both interfaces shows a slight variation upon annealing. For the Co/Y/Mo_2C multilayers, the interface widths of the Mo_2C-on-Y and Co-on-Y interfaces are determined to be 1.11 nm and 0.97 nm at 300°C. At 600°C, both interface widths increase and the value of Y-on-Co interfaces is larger than that of Mo_2C-on-Y interface.

Table 4.4 Structural parameters of the Co/Mo$_2$C/Y and Co/Y/Mo$_2$C multilayers determined from the in-depth intensity profile. The uncertainty of the interface width is about 0.1 nm.

Parameters	Co/Mo$_2$C/Y			Co/Y/Mo$_2$C	
	As-deposited	300°C	600°C	300°C	600°C
Period (±0.20 nm)-intensity profile	7.68	7.48	7.66	7.61	7.65
Period (±0.05 nm)-XRR fitting	7.67	7.48	7.46	7.55	7.37
d_Y	3.89	4.10	4.10	4.09	3.92
$d_{Co+Mo2C}$	3.98	3.38	3.56	3.52	3.73
$\delta_{Y\text{-on-}Mo2C}$	1.12	1.36	1.20	--	--
$\delta_{Co\text{-on-}Y}$	1.33	1.17	1.30	--	--
$\delta_{Mo2C\text{-on-}Y}$	--	--	--	1.11	1.27
$\delta_{Y\text{-on-}Co}$	--	--	--	0.97	1.67

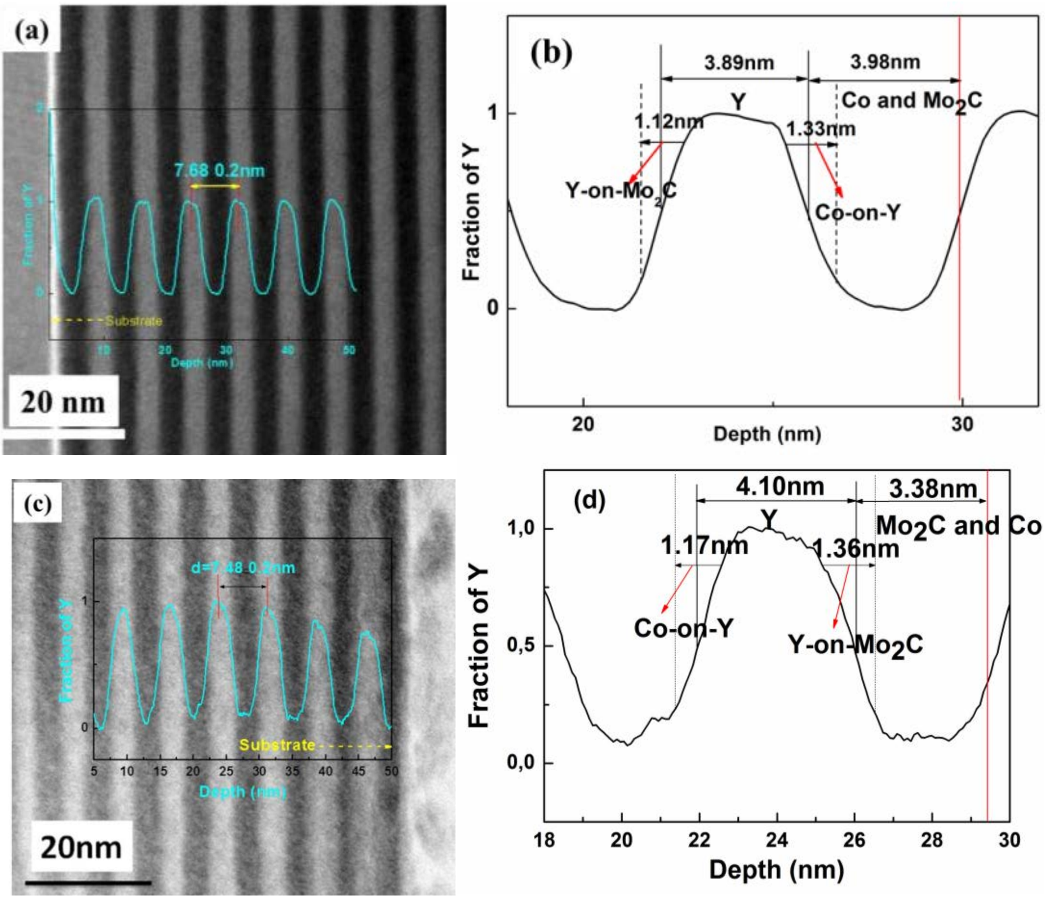

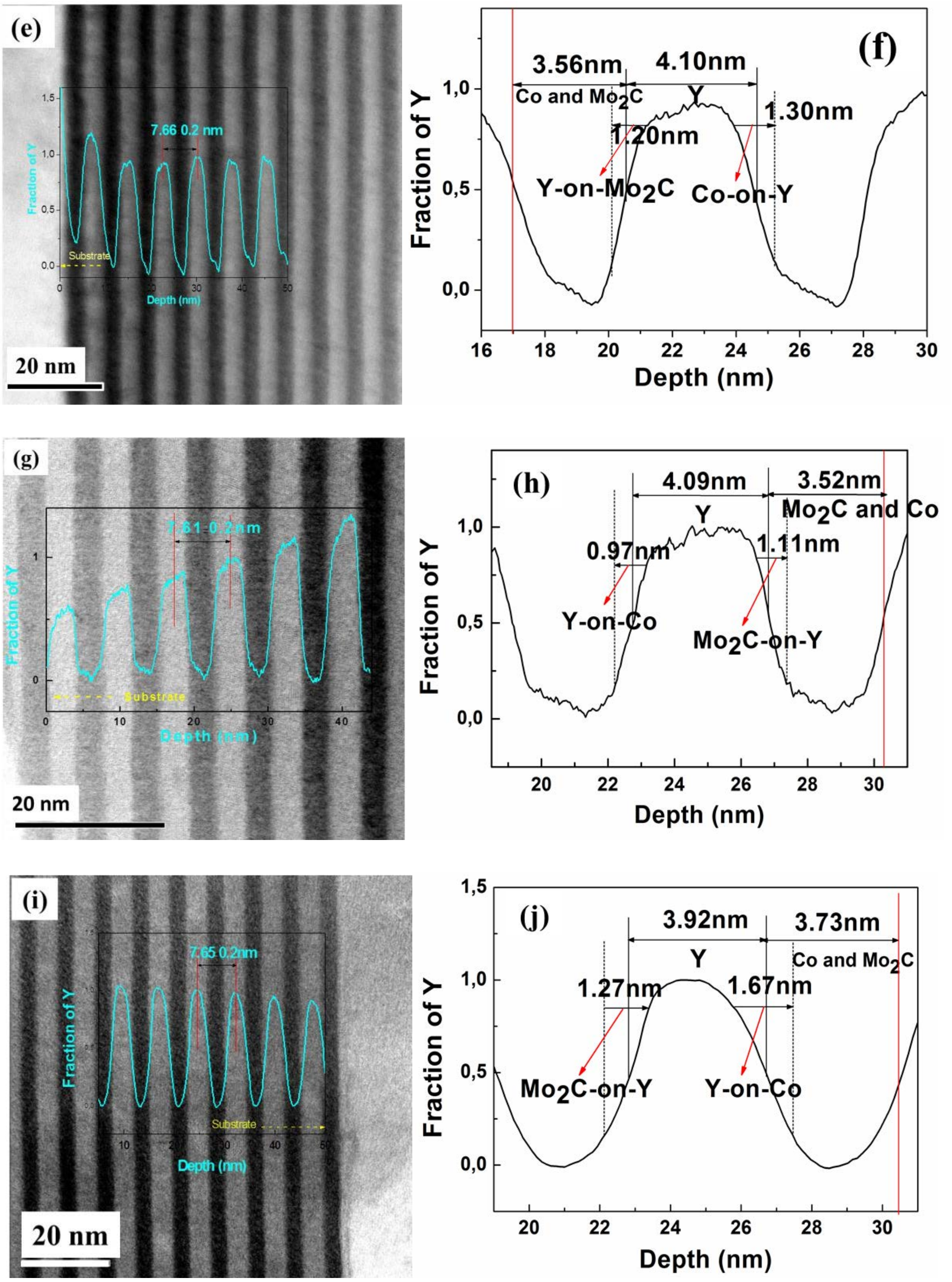

Figure 4.10 Bright field images and in-depth intensity profiles of few periods of the multilayer stacks in the STEM mode. (a), (c), (e) (g) and (i) correspond to the Co/Mo$_2$C/Y_as-deposited, Co/Mo$_2$C/Y_300°C, Co/Mo$_2$C/Y_600°C, Co/Y/Mo$_2$C_300°C, Co/Y/Mo$_2$C_600°C, respectively. The thickness of one period layers and interfacial widths are indicated. (b), (d), (f), (h) and (j) are the detail of in-depth intensity profile.

3) Energy dispersive x-rays spectrometry (EDS)

Figure 4.11(a), (b), (c), (d) and (e) show EDS line-profiles performed in the HAADF-STEM mode of the Co/Mo_2C/Y_as-deposited, Co/Mo_2C/Y_300°C, Co/Mo_2C/Y_600°C, Co/Y/Mo_2C_300°C and Co/Y/Mo_2C_600°C samples, respectively. By combining the HAADF image and the EDS line profile, we find that the Y layers do correspond to the dark regions. The Mo_2C and Co layers correspond to the bright region. About the Co/Mo_2C/Y_as-deposited sample, in Figure 4.11(a), the Mo concentration profile shows a shoulder close to the Co layers and corresponding to the maximum of the Co concentration profile. This suggests that the Co layers do mix with Mo_2C layers. The decreasing part of Mo and Co concentration profiles is related to the increase part of Y concentration profile. This suggests that a part Y layers mixed with Mo_2C and Co layers. The Co/Mo_2C/Y_300°C sample presents the same behavior. For the Co/Mo_2C/Y_600°C sample, in Figure 4.11(c), the shoulder in the Mo concentration profile disappears. Its increasing part corresponds to the maximum of the Co concentration profile. This suggests that interdiffusion between Mo_2C and Co layers is aggravated at 600°C.

For the Co/Y/Mo_2C_300°C sample, in Figure 4.11(d), the decreasing part of the Mo concentration profile corresponds to the maximum of the Co concentration profile and the increasing part of the Y concentration profile. This suggests that the interdiffusion between Mo_2C and Co layers is stronger than that of between Mo_2C and Y layers. The decreasing part of the Co concentration profile corresponds to the increasing part of the Y concentration profile. At 600°C, Figure 4.11(e), the maximum of the Mo concentration profile corresponds to the maximum of the Co concentration profile and minimum of the Y concentration profile. This suggests that the interdiffusion between Mo_2C and Co layers increases at high temperature. A large overlap between the Mo and Y concentration profiles suggests an interdiffusion between the Mo_2C and Y layers. However the interdiffusion between the Mo_2C and Y layers is probably due to the interaction between Y and C atoms at the interfaces.

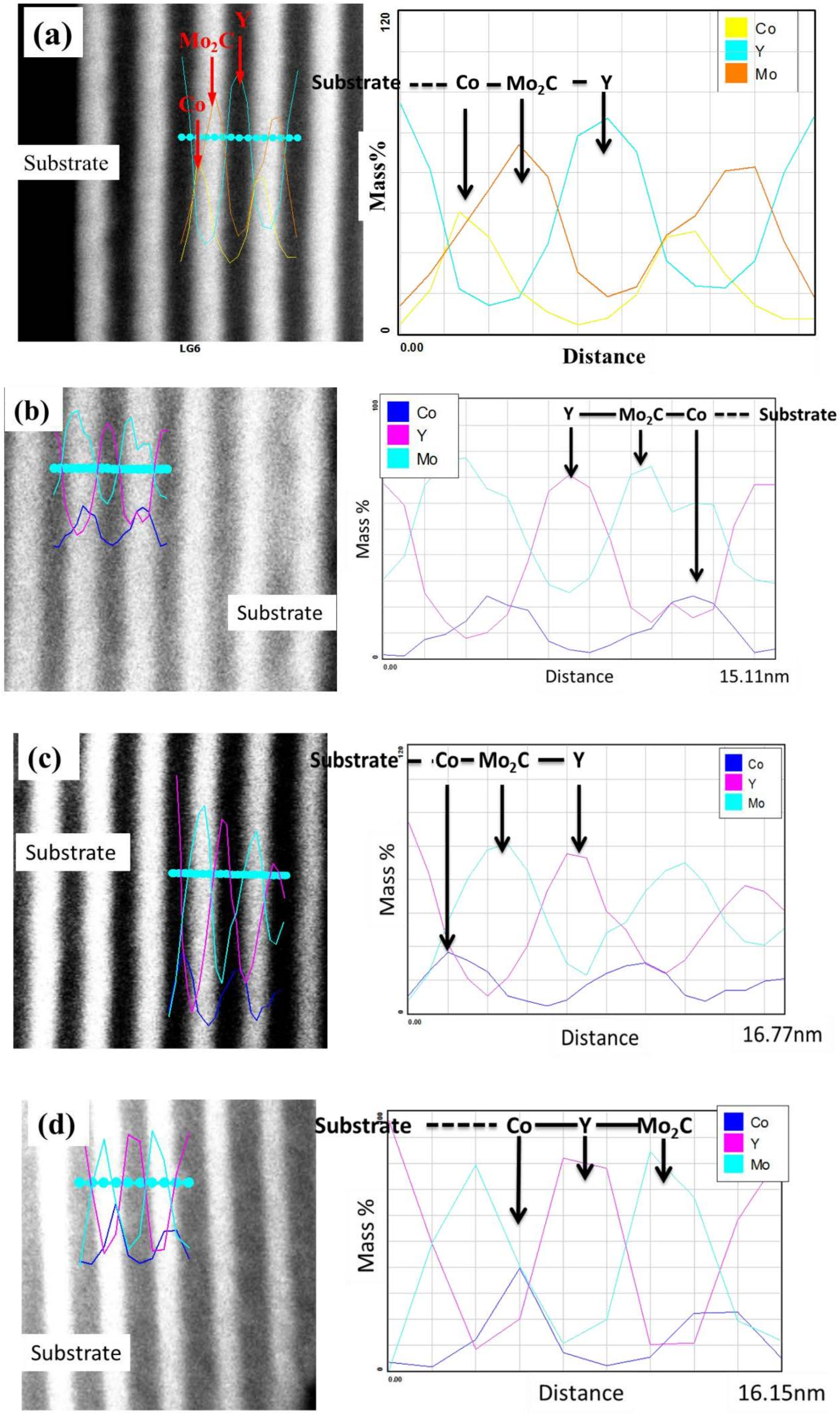
(a)
Y
Mo2C
Co
Substrate
LG6
120
0
0.00
Substrate --- Co — Mo2C — Y
Mass%
Distance
Co
Y
Mo
(b)
Substrate
100
0
0.00
Y — Mo2C — Co --- Substrate
Mass %
Distance
15.11nm
Co
Y
Mo
(c)
Substrate
Substrate — Co — Mo2C — Y
120
0
0.00
Mass %
Distance
16.77nm
Co
Y
Mo
(d)
Substrate
Substrate ----- Co — Y — Mo2C
100
0
0.00
Mass %
Distance
16.15nm
Co
Y
Mo

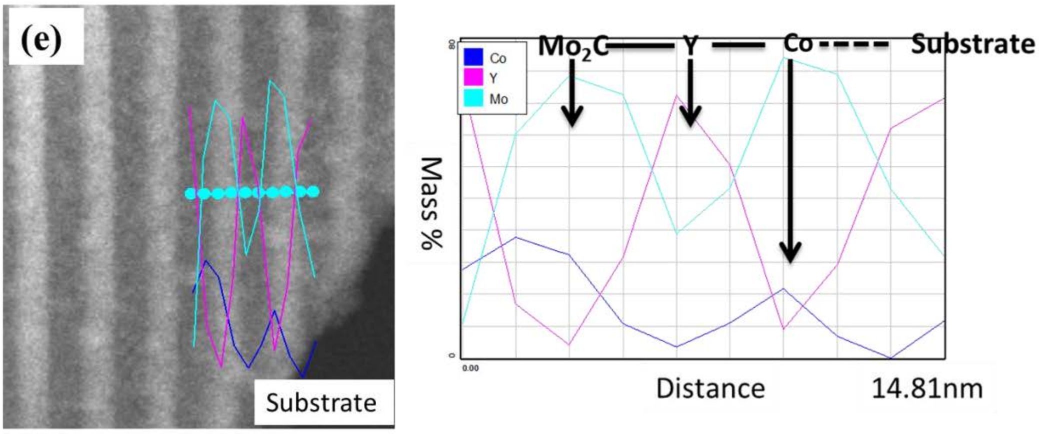

Figure 4.11 HAADF images and EDS line-profiles of the multilayer samples: Co/Mo$_2$C/Y_as-deposited (a), 300°C (b) and 600°C (c), Co/Y/Mo$_2$C_300°C (d) and 600°C (e).

4) High-resolution images and selected-area electron diffraction

Shown in Figure 4.12 are the high-resolution images and selected-area electron diffraction (SAED) of both Co/Mo$_2$C/Y and Co/Y/Mo$_2$C systems. Figure 4.12(a) is related to the Co/Mo$_2$C/Y_as-deposited sample. We find that in the high-resolution image there are some lattice fringes with different orientation which correspond to the crystallized regions in the bright Y layers. This indicates that the Y layers are polycrystalline. Mo$_2$C and Co do not show significant lattice fringes and are amorphous. We observe a diffraction ring and some bright spots in the SAED which probably corresponds to some crystallites. For the Co/Mo$_2$C/Y_300°C annealed sample, Figure 4.12(b), the lattices fringes become clear within the Y layers, but the interfaces are not sharp which means a strong intermixing. Figure 4.12(c) shows image of the Co/Mo$_2$C/Y_600°C annealed sample and its substrate. We find that the interfaces become clearer and shaper than that of the Co/Mo$_2$C/Y_300°C annealed sample and show a wavy shape. Some crystallites grow within the Y layers. Otherwise the substrate-on-layers interface shows an interlayer with a thickness of 2.0 nm. This is probably due to the formation of silicon oxide or intermixing between Si substrate and its nearest Co layer.

For the Co/Y/Mo$_2$C system, high-resolution images and SAED patterns have been recorded. Figure 4.12(d) and (e) correspond to the Co/Y/Mo$_2$C_300 and 600°C annealed samples, respectively. We find that lattice fringes are visible within the Y layers for both samples and at 600°C they are also observed at the interfaces (marked in red box). In Figure 4.12(d), an interlayer with thickness of about 1.15 nm is observed at the substrate-on-layers interface. SAED patterns without substrate corresponding to the Co/Y/Mo$_2$C_300 and 600°C annealed samples are also shown in Figure 4.12(d) and (e), respectively.

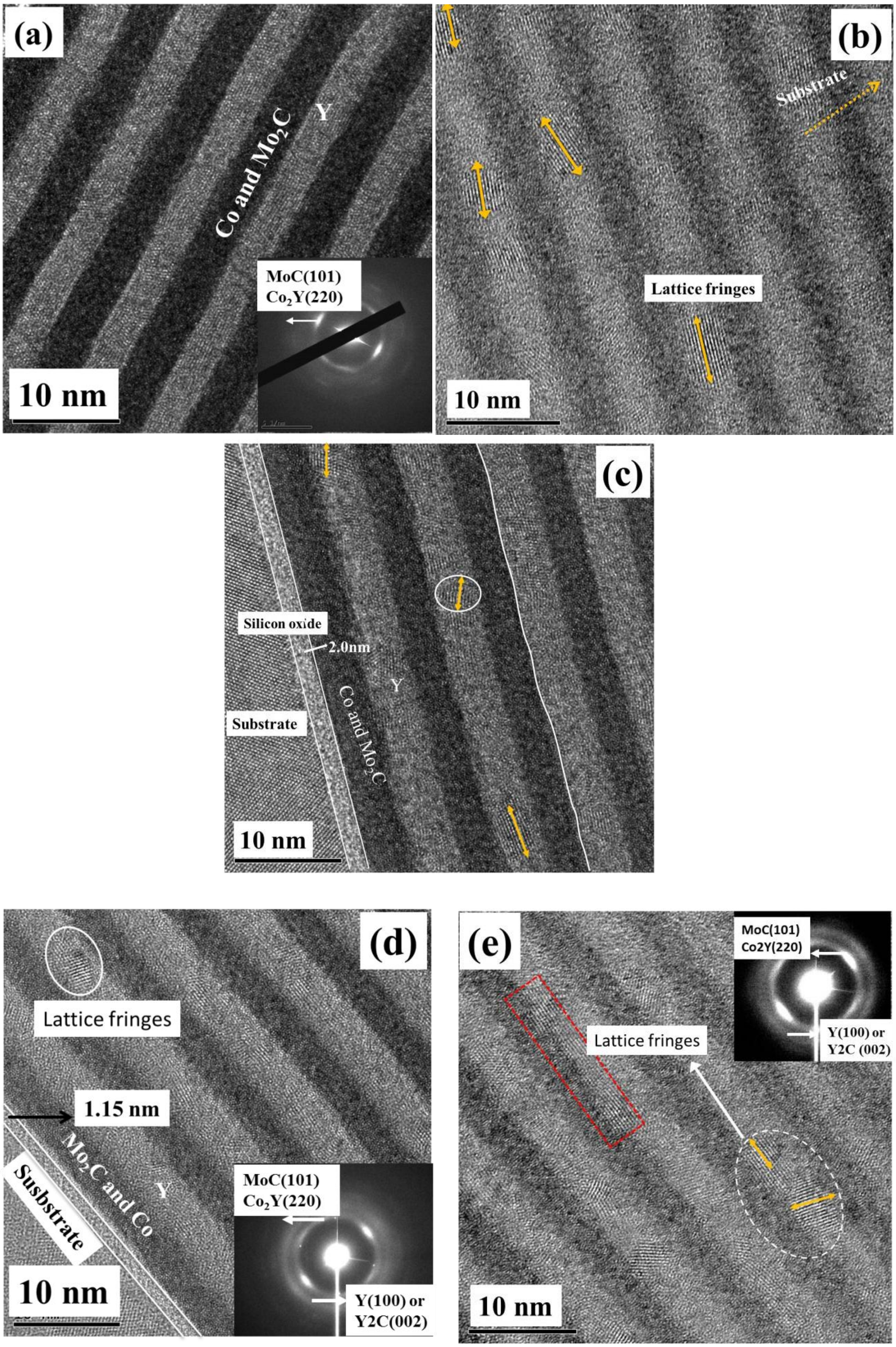

Figure 4.12 High-resolution images and selected-area electron diffraction of the multilayer samples: Co/Mo$_2$C/Y_as-deposited (a), Co/Mo$_2$C/Y_300°C (b), Co/Mo$_2$C/Y_600°C (c), Co/Y/Mo$_2$C_300°C (d) and Co/Y/Mo$_2$C_600°C (e).

A series of diffraction rings are observed for both samples. In both SAED patterns, the first ring (counted from center) is not homogeneous and is accompanied by some bright spots, which are due to the presence of small crystallites. The second ring appears without bright spots. This suggests that the multilayer structure is a combination of amorphous and some crystallized zones. This is accordance with the presence of lattice fringes with different orientations in the layers.

Comparing the high-resolution images of the $Co/Mo_2C/Y$ and $Co/Y/Mo_2C$ systems, we find that the lattice fringes exist in Y layers for both systems. Some crystallites are formed across the Y layers. The lattice spacing in the crystallites is determined to be about 0.3 nm from the high-resolution image, which is consistent with the result of electron diffraction.

To give a clear description of multilayer structure, we present in Figure 4.13 two diffusion pictures based on the preceding observation for both systems after annealing. Figure 4.13(a) represents the diffusion of the $Co/Mo_2C/Y$ multilayer stack. Co and Mo_2C layers are partly mixed and cannot be discerned in one period as the formation of mixture with average atomic number close to that of Co or Mo_2C. Crystallites with different sizes appear in the Y layers. Regarding the $Co/Y/Mo_2C$_600°C multilayer, crystallites appear not only in the Y layers but also at the Mo_2C-on-Y interfaces and the corresponding diffusion picture is shown in Figure 4.13(b). Considering the impossibility to form a Y and Mo compound, these crystallites are probably related with the disorder alloys or compound between Y and C atoms. This explains the proposal of fitting model for $Co/Y/Mo_2C$ multilayer. This demonstrates that the intermixing easily takes place when Mo and C atoms are deposited on the Y layers.

The presence of the crystallites can affect the interdiffusion and the formation of interlayers. From the thermodynamic point of view, the free energy of crystallite decreases with respect to that of amorphous structure and thus this can cause the decrease of driving force for the interdiffusion. This suggests that the interdiffusion between Y and nearest Mo_2C layers is suppressed when Mo and C atoms are deposited on the Y layers. Hence, at 600°C, the value of Mo_2C-on-Y interfaces is smaller than that of Y-on-Co interfaces.

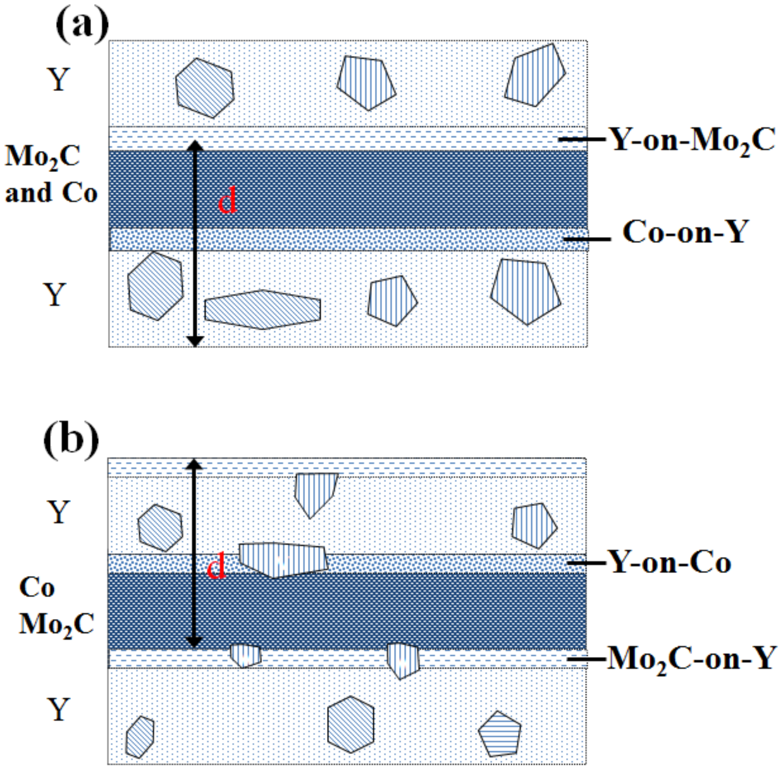

Figure 4.13 Scheme of diffusion of the Co/Mo_2C/Y multilayers (a) and Co/Y/Mo_2C multilayer (b) after annealing.

The interface width obtained from the intensity profile is different from the value derived from the fitting of x-ray reflectivity data. The reason is that the fitting values represent the evaluation of interface width for the whole stack, while the values from the intensity profile only represent the small part from the stack. From the HAADF image, we only see two layers in one period, and Co and Mo_2C layers are not distinguishable. Noting that the average atomic numbers of Co (27) and Mo_2C (30) are close, if Co and Mo_2C layers are mixed they could form some intermixtures having an average atomic number close to the ones of Co or Mo_2C. For example, the average atomic number of Co_3Mo is 30. Consequently, they cannot be recognized. It should be kept in mind that the interdiffusion is observed in the annealed samples. However, the interdiffusion could also be introduced during deposition where re-sputtering can occur. In the case of Co/Mo_2C/Y system, after the deposition of a Co layer, the Mo_2C layer begins to grow on the deposited Co layer. Owing to the bombardment of the energetic atoms, the arrival Mo and C atoms replace or mix with the Co atoms. After annealing, the interdiffusion aggravates. This is demonstrated by the observation of interface width of the Co/Mo_2C/Y_300 and 600°C samples.

The observation of interdiffusion between Co and Y and Mo_2C layers through the TEM techniques also validate the results reported in the Section 4.1, which present no pure Co in both systems after annealing.

4.2.4 Conclusions

The interfacial properties of Co/Mo_2C/Y and Co/Y/Mo_2C systems upon annealing have been studied by using transmission electron microscopy. The HAADF-STEM images show that all samples display two layers in one period, indicating that Co, Mo_2C and Y layers intermix before and after annealing. Co and Mo_2C layers cannot be distinguished in one period. From the high-resolution TEM image, we observe some crystallites in the Y layers within all the samples. Furthermore the Co/Y/Mo_2C sample annealed at 600°C shows some crystallites at the interfaces. The quantitative in-depth intensity profiles of multilayer structure extracted from the bright field images were analyzed to evaluate the interface widths of Co-on-Y, Y-on-Mo_2C, Y-on-Co and Mo_2C-on-Y interfaces. They show different evolutions upon annealing in both systems. TEM and in-depth intensity profiles provide a direct observation of interface width and is good supplementary method for observing interface structure in the multilayer stacks.

Chapter 5 Conclusions and perspectives

In this thesis we focused on the characterization of physico-chemical environment of Co-based multilayers. Two systems, Co/Mo_2C and Co/Mo_2C/Y, have been studied by combining non-destructive and destructive methods to investigate their interface properties. The observation of interface changes of both systems upon annealing is important for improving their optical performance.

We firstly investigated the optical performance and interface properties of Co/Mo_2C multilayers designed to work in the soft x-ray range at grazing incidence angle. The results show that these multilayers can work up to 600°C. Then we measured the reflectivity at the application wavelength of 1.59 nm. The best reflectivity (27%) was obtained for the Co/Mo_2C_300°C sample; the reflectivity was found to decrease to 20% annealed at 600°C.

We performed soft x-ray standing wave enhanced x-ray photoemission spectroscopy to observe the evolution of the first buried interfaces of a B_4C capped Co/Mo_2C multilayer mirror induced by annealing up to 600°C. Samples annealed at 200°C and 600°C have been studied. The results show the good stability of the Mo_2C-on-B_4C interface upon annealing and the good protective action of the B_4C capping layer. The analysis shows no significant increase of the Mo_2C-on-B_4C interface, with only a small oxidation of 0.2 nm of the buried Mo_2C first layer. XES and NMR results show for the as-deposited sample that Co atoms mixed with C atoms coming from the Mo_2C layer. After sample annealed at 300°C and above, we observed that a demixing between Co and C atoms takes place. The calculation of mixing enthalpy, using Miedema's model, confirms phase separation of the Co-C system. However, we should keep in mind that the Co and C atoms separated from their mixed region do not go back their original layers. This means that there are no sharp interfaces between layers after annealing. Co and C atoms are still in their original mixed region but show a short range order after annealing. This can reduce the multilayer optical contrast and explains why the reflectivity decreases after annealing. For this system, there are two interfaces: Co-on-Mo_2C and Mo_2C-on-Co. New work is needed to make clear the effect of both interfaces on the optical performance.

We designed tri-layer Co/Mo_2C/Y systems with an insertion of a third material (Y) into the Co/Mo_2C multilayer. Two systems were designed with different interface orders: Co/Mo_2C/Y and Co/Y/Mo_2C. Both systems show compressed periods after annealing. At application wavelengths, the Co/Mo_2C/Y multilayers show a high reflectivity (27.5%) for as-deposited sample; then the reflectivity gradually decreases upon annealing. However the

Co/Y/Mo_2C multilayers show a poor reflectivity. NMR spectroscopy indicates that there are no pure Co layers left in both systems. But the NMR spectrum of the as-deposited Co/Mo_2C/Y sample is the same as that of the Co_3Mo disordered alloy, indicating alloy is formed at the Mo_2C-on-Co interface. High-resolution transmission electron microscopy shows that only two layers are observed in one period and the Co and Mo_2C layers cannot be recognized because of their close average atomic numbers. There are some crystallites in the Y layers in both annealed systems. Furthermore, we observed some crystallites at the interfaces of the Co/Y/Mo_2C systems. Through analyzing the intensity profile extracted from the bright field images we obtained the detailed description of interface width.

From the study of Co-based multilayers, we find that the interface properties of buried structures can be well investigated by combing some non-destructive methods: XRR, XES and NMR. This is a good example for analyzing buried interfaces within other systems. Furthermore, the x-ray standing wave field generated by a multilayer structure has been preliminary studied. The x-ray photoemission spectroscopy enhanced by XSW has been successfully used to analyze the first buried interfaces. A model for analyzing the internal interfaces within the multilayer stack is developed by using enhanced inflorescence by XSW. The corresponding simulations of the depth distributions of the electric field and the energy loss of the radiation were presented. This method would be a powerful tool for analyzing the samples without damage.

Further experiments are needed to improve the interdiffusion mechanism in the Co-based multilayers. For the Co/Mo_2C multilayers, in order to identify the interdiffusion of Mo and C components into the Co layers and to study the formation of compounds in the stack, this could be realized by preparing a series of samples: Co/Mo and Co/C thin layer with different thickness of Mo an C layers when thickness of Co layers are fixed or preparing disordered alloys, and by performing the NMR spectroscopy, XES and near edge x-ray absorption fine structure spectroscopy (NEXAFS) experiments. Concerning the Co/Mo_2C/Y system, in order to identify the formation of Co_xY_y, Y_xC_y compounds, some reference Co_xY_y and Y_xC_y disordered alloys or Co/Y and Y/C thin layers should be prepared and NMR, XES and NEXAFS used to improve the analysis of the Co/Mo_2C/Y system.

Appendix I: Miedema’s model

The mixing enthalpy of the Co-Mo system, made of two transition metals, can be expressed as:

$$\Delta H = \frac{2Pc_{Mo}f_{Co}^{Mo}V_{Mo\,alloy}^{2/3}\left[-(\phi_{Mo}-\phi_{Co})^2+\frac{Q}{P}\left(n_{ws}^{Mo^{1/3}}-n_{ws}^{Co^{1/3}}\right)^2\right]}{n_{ws}^{Mo^{-1/3}}+n_{ws}^{Co^{-1/3}}} \tag{1.1}$$

where

$$f_{Co}^{Mo} = C_{Co}^{S} \qquad \text{for non-ordered alloys}$$

$$f_{Co}^{Mo} = C_{Co}^{S}\left(1+8\left(C_{Mo}^{S}C_{Co}^{S}\right)^2\right) \qquad \text{for ordered alloys}$$

$$c_{Mo}^{S} = c_{Mo}V_{Mo}^{2/3}\left(c_{Mo}V_{Mo}^{2/3}+c_{Co}V_{Co}^{2/3}\right)$$

$$c_{Co}^{S} = c_{Co}V_{Co}^{2/3}\left(c_{Mo}V_{Mo}^{2/3}+c_{Co}V_{Co}^{2/3}\right)$$

$$P=14.1, \qquad Q/P=9.4\ V^2/(\text{d.u.})^{2/3}$$

Here, c_{Co} and c_{Mo} are the mole fraction ($c_{Co}+c_{Mo}=1$), V_{Co} and V_{Mo} are the atomic volumes of Co and Mo, respectively, ϕ the electronegativity of components Co and Mo and n_{ws} the electron density at the first Wigner-Seitz boundary. The electron densities are usually given in terms of density units (d.u.), 1 d.u.=6.75×10^{22} electron/cm^3. C_{Co}^{S} and C_{Mo}^{S} are the surface densities of Co and Mo atoms, respectively. f_{Co}^{Mo} represents the degree to which an atomic cell of Mo is in contact with dissimilar atomic cell of Co on average within the alloy. When we calculate the atomic volume in the alloy, the atomic volumes of Co and Mo atoms are approximated to be the same one. In equation (1.1), the first term is negative and proportional to the square of difference in the electronegativity parameters and therefore the charge transfer between Co and Mo. This part shows the tendency for compound formation. The second term which is positive stands for the discontinuity in electron density at the Wigner-Seitz boundary of Co and Mo atoms. This part shows the tendency of phase separation.

Another effect, which has to be considered, is the volume change of the constituents Co and Mo that occurs due to charge transfer when the alloy is formed. The charge transfer occurring between dissimilar atomic cells depends on the difference of the electronegative parameters of Co and Mo. An empirical relationship for volume change has been established

$$V_{Mo\,alloy}^{2/3} = V_{Mo\,pure}^{2/3}\cdot\left[1+af_{Co}^{Mo}(\phi_{Mo}-\phi_{Co})\right] \tag{1.2}$$

where a is a constant equal to 0.04 for Mo and 0.1 for Co [106].

Table 1 Values of ϕ, n_{ws} and V for calculating the mixing enthalpy of the Co-Mo system.

Element	ϕ (V)	n_{ws} (d.u.)	V (cm^3/mol)
Co	5.10	7.00	6.7
Mo	4.37	8.46	9.4

For the Mo-C system, the enthalpy change can be expressed as:

$$\Delta H = \frac{2Pc_C f_{Mo}^C \left(c_C V_C^{2/3} + c_{Mo} V_{Mo}^{2/3}\right)\left[-\left(\phi_C - \phi_{Mo}\right)^2 + \frac{Q}{P}\left(n_{ws}^{C\,1/3} - n_{ws}^{Mo\,1/3}\right)^2 - \frac{R}{P}\right]}{n_{ws}^{Mo\,-1/3} + n_{ws}^{C\,-1/3}} + c_C\left[\Delta H\left(C_{element} \rightarrow C_{metal}\right)\right] \quad (1.3)$$

$$c_{Mo}^S = c_{Mo} V_{Mo}^{2/3}\left(c_{Mo} V_{Mo}^{2/3} + c_C V_C^{2/3}\right)$$

$$c_C^S = c_C V_C^{2/3}\left(c_{Mo} V_{Mo}^{2/3} + c_C V_C^{2/3}\right)$$

P=14.1, Q/P=9.4 V^2/(d.u.)$^{2/3}$ R/P=2.1 V^2

Here $\Delta H\left(C_{element} \rightarrow C_{metal}\right)$ stands for the transformation enthalpy of C into a metallic state and the third term in the equation (1.3) represents a hybridization contribution and favors a tendency of phase separation. For carbon, the corresponding transformation energy equals the heat of fusion, 100 kJ/mol. To improve the agreement between predicted and experimental values, the transformation energy has been changed to 180 kJ/mol [107].

As mentioned above, we need to consider the volume change of the C and Mo constituents that occurs due to charge transfer when the alloy is formed. The relation is expressed as:

$$V_{C\,alloy}^{2/3} = V_{C\,pure}^{2/3} \cdot \left[1 + a f_{Mo}^C \left(\phi_C - \phi_{Mo}\right)\right] \quad (1.4)$$

where a is a constant equal to 0.04 for carbon.

It should be noted that in this model we did not calculate Gibbs free energy so entropy is not taken into account.

References

1. D. L. Windt, "IMD - Software for modeling the optical properties of multilayer films," Comput. Phys. **12**, 360–370 (1998).
2. E. Spiller, "Low-Loss Reflection Coatings Using Absorbing Materials," Appl. Phys. Lett. **20**, 365–367 (1972).
3. M. Yamamoto and T. Namioka, "Layer-by-layer design method for soft-x-ray multilayers," Appl. Opt. **31**, 1622–1630 (1992).
4. J. I. Larruquert, "General theory of sub-quarterwave multilayers with highly absorbing materials," J. Opt. Soc. Am. A Opt. Image Sci. Vis. **18**, 2617–2627 (2001).
5. J. I. Larruquert, "Layer-by-layer design method for multilayers with barrier layers: application to Si/Mo multilayers for extreme-ultraviolet lithography," J. Opt. Soc. Am. A Opt. Image Sci. Vis. **21**, 1750–1760 (2004).
6. J. I. Larruquert, "Inreflectance: a new function for the optimization of multilayers with absorbing materials," J. Opt. Soc. Am. A Opt. Image Sci. Vis. **22**, 1607–1614 (2005).
7. J. I. Larruquert, "New layer-by-layer multilayer design method," J. Opt. Soc. Am. A Opt. Image Sci. Vis. **19**, 385–390 (2002).
8. J. I. Larruquert, "Reflectance enhancement in the extreme ultraviolet and soft x rays by means of multilayers with more than two materials," J. Opt. Soc. Am. A Opt. Image Sci. Vis. **19**, 391–397 (2002).
9. J. I. Larruquert, "Reflectance optimization of inhomogeneous coatings with continuous variation of the complex refractive index," J. Opt. Soc. Am. A Opt. Image Sci. Vis. **23**, 99–107 (2006).
10. J. I. Larruquert, "Can multilayers be optimized sequentially when radiation is partially polarized?," J. Opt. Soc. Am. A Opt. Image Sci. Vis. **23**, 1967–1970 (2006).
11. A. V. Vinogradov and B. Y. Zeldovich, "X-ray and far uv multilayer mirrors: principles and possibilities," Appl. Opt. **16**, 89–93 (1977).
12. J.-P. Delaboudinière, G. E. Artzner, J. Brunaud, A. H. Gabriel, J. F. Hochedez, F. Millier, X. Y. Song, B. Au, K. P. Dere, R. A. Howard, R. Kreplin, D. J. Michels, J. D. Moses, J. M. Defise, C. Jamar, P. Rochus, J. P. Chauvineau, J. P. Marioge, R. C. Catura, J. R. Lemen, L. Shing, R. A. Stern, J. B. Gurman, W. M. Neupert, A. Maucherat, F. Clette, P. Cugnon, and E. L. V. Dessel, "EIT: Extreme-ultraviolet Imaging Telescope for the SOHO mission," Sol. Phys. **162**, 291–312 (1995).
13. J. F. Seely, C. M. Brown, D. L. Windt, S. Donguy, and B. Kjornrattanawanich, "Normal-Incidence Efficiencies of Multilayer-Coated Laminar Gratings for the Extreme-Ultraviolet Imaging Spectrometer on the Solar-B Mission," Appl. Opt. **43**, 1463–1471 (2004).
14. A. B. C. Walker, J. F. Lindblom, R. H. O'Neal, R. B. Hoover, and T. W. Barbee, "Astronomical observations with normal incidence multilayer optics: recent results and future prospects," Phys. Scr. **41**, 1053 (1990).
15. "http://www.nasa.gov/mission_pages/iris/multimedia/sun-by-trace.html#.Upid9SfjPh8,".
16. A. B. Walker Jr, J. F. Lindblom, T. W. Barbee Jr, and R. B. Hoover, "Soft X-ray Images of the Solar Corona with a Normal-Incidence Cassegrain Multilayer Telescope," Science **241**, 1781–1787 (1988).
17. S. Bajt, J. B. Alameda, J. Barbee, W. M. Clift, J. A. Folta, B. Kaufmann, and E. A. Spiller, "Improved reflectance and stability of Mo-Si multilayers," Opt. Eng. **41**, 1797–1804 (2002).
18. M. Kado, K. Yamashita, M. Ohtani, K. A. Tanaka, R. Kodama, S. Kitamoto, T. Yamanaka, and S. Nakai, "Development of a Schwarzschild-type x-ray microscope," Opt. Lett. **16**, 109–111 (1991).

19. J. B. Kortright, E. M. Gullikson, and P. E. Denham, "Masked deposition techniques for achieving multilayer period variations required for short-wavelength (68-A) soft-x-ray imaging optics," Appl. Opt. **32**, 6961–6968 (1993).
20. J. Zegenhagen and A. Kazimirov, *The X-Ray Standing Wave Technique: Principles and Applications*, Vol. 7. (2010).
21. M. J. Bedzyk, G. M. Bommarito, and J. S. Schildkraut, "X-ray standing waves at a reflecting mirror surface," Phys. Rev. Lett. **62**, 1376–1379 (1989).
22. S.-H. Yang, B. S. Mun, N. Mannella, S.-K. Kim, J. B. Kortright, J. Underwood, F. Salmassi, E. Arenholz, A. Young, Z. Hussain, M. A. V. Hove, and C. S. Fadley, "Probing buried interfaces with soft x-ray standing wave spectroscopy: application to the Fe/Cr interface," J. Phys. Condens. Matter **14**, L407 (2002).
23. S. Bajt, D. G. Stearns, and P. A. Kearney, "Investigation of the amorphous-to-crystalline transition in Mo/Si multilayers," J. Appl. Phys. **90**, 1017–1025 (2001).
24. A. Kloidt, K. Nolting, U. Kleineberg, B. Schmiedeskamp, U. Heinzmann, P. Müller, and M. Kühne, "Enhancement of the reflectivity of Mo/Si multilayer x-ray mirrors by thermal treatment," Appl. Phys. Lett. **58**, 2601–2603 (1991).
25. H. Takenaka and T. Kawamura, "Thermal stability of Mo/C/Si/C multilayer soft x-ray mirrors," J. Electron Spectrosc. Relat. Phenom. **80**, 381–384 (1996).
26. H.-J. Voorma, E. Louis, N. B. Koster, and F. Bijkerk, "Temperature induced diffusion in Mo/Si multilayer mirrors," J. Appl. Phys. **83**, 4700–4708 (1998).
27. M. H. Modi, G. S. Lodha, M. Nayak, A. K. Sinha, and R. V. Nandedkar, "Determination of layer structure in Mo/Si multilayers using soft X-ray reflectivity," Phys. B-Condens. Matter **325**, 272–280 (2003).
28. R. S. Rosen, D. S. P. Vernon, G. Stearns, M. A. Viliardos, M. E. Kassner, and Y. Cheng, "Silicide layer growth rates in Mo/Si multilayers," Appl. Opt. **32**, 6975–6980 (1993).
29. T. Feigl, H. Lauth, S. Yulin, and N. Kaiser, "Heat resistance of EUV multilayer mirrors for long-time applications," Microelectron. Eng. **57–58**, 3–8 (2001).
30. S. Ogura, M. Niibe, Y. Watanabe, M. Hayashida, and T. Iizuka, "Comparison Among Multilayer Soft X-Ray Mirrors Fabricated By Electron Beam, Dc-, Rf-Magnetron Sputtering And Ion Beam Sputtering Deposition," Proc.SPIE, 140–149 (1988).
31. T. Feigl, S. Yulin, N. Benoit, and N. Kaiser, "EUV multilayer optics," Microelectron. Eng. **83**, 703–706 (2006).
32. P. Jonnard, K. Le Guen, M.-H. Hu, J.-M. André, E. Meltchakov, C. Hecquet, F. Delmotte, and A. Galtayries, "Optical, chemical and depth characterization of Al/SiC periodic multilayers," Proc.SPIE, 73600O-73600O-9 (2009).
33. M.-H. Hu, K. Le Guen, J.-M. André, P. Jonnard, E. Meltchakov, F. Delmotte, and A. Galtayries, "Structural properties of Al/Mo/SiC multilayers with high reflectivity for extreme ultraviolet light," Opt. Express **18**, 20019–20028 (2010).
34. Q. Zhong, Z. Zhang, J. Zhu, Z. Wang, P. Jonnard, K. Le Guen, Y. Yuan, J.-M. André, H. Zhou, and T. Huo, "The thermal stability of Al(1%wtSi)/Zr EUV mirrors," Appl. Phys. -Mater. Sci. Process. **109**, 133–138 (2012).
35. Q. Zhong, Z. Zhang, J. T. Zhu, Z. S. Wang, P. Jonnard, K. Le Guen, Y. Y. Yuan, J.-M. Andre, H. Zhou, and T. Huo, "The thermal stability of Al(1%wtSi)/Zr EUV mirrors," Appl. Phys. -Mater. Sci. Process. **109**, 133–138 (2012).
36. K. Le Guen, M.-H. Hu, J.-M. André, P. Jonnard, S. K. Zhou, H. C. Li, J. T. Zhu, Z. S. Wang, and C. Meny, "Development and Interfacial Characterization of Co/Mg Periodic Multilayers for the EUV Range," J. Phys. Chem. C **114**, 6484–6490 (2010).
37. K. Le Guen, M.-H. Hu, J.-M. André, P. Jonnard, S.-K. Zhou, H.-C. Li, J.-T. Zhu, Z.-S. Wang, N. Mahne, A. Giglia, and S. Nannarone, "Introduction of Zr in nanometric periodic Mg/Co multilayers," Appl. Phys. Mater. Sci. Process. **102**, 69 (2011).

38. R. S. Rosen, M. A. Viliardos, M. E. Kassner, D. G. Stearns, and S. P. Vernon, "Thermal stability of Mo/Si multilayers," SPIE Proc. 212–220 (1992).
39. T. Böttger, D. C. Meyer, P. Paufler, S. Braun, M. Moss, H. Mai, and E. Beyer, "Thermal stability of Mo/Si multilayers with boron carbide interlayers," Thin Solid Films **444**, 165–173 (2003).
40. V. V. Kondratenko, Y. P. Pershin, O. V. Poltseva, A. I. Fedorenko, E. N. Zubarev, S. A. Yulin, 1. V. Kozhevnikov, S. I. Sagitov, V. A. Chirkov, V. E. Levashov, and A. V. Vinogradov, "Thermal stability of soft x-ray Mo-Si and $MoSi_2$-Si multilayer mirrors," Appl. Opt. **32**, 1811–1816 (1993).
41. S. L. Nyabero, R. W. E. van de Kruijs, A. E. Yakshin, E. Zoethout, and F. Bijkerk, "Thermally induced interface chemistry in Mo/B_4C/Si/B_4C multilayered films," J. Appl. Phys. **112**, 054317–054317–5 (2012).
42. D. G. Stearns, M. B. Stearns, Y. Cheng, J. H. Stith, and N. M. Ceglio, "Thermally induced structural modification of Mo-Si multilayers," J. Appl. Phys. **67**, 2415–2427 (1990).
43. S. Yulin, T. Feigl, T. Kuhlmann, N. Kaiser, A. I. Fedorenko, V. V. Kondratenko, O. V. Poltseva, V. A. Sevryukova, A. Y. Zolotaryov, and E. N. Zubarev, "Interlayer transition zones in Mo/Si superlattices," J. Appl. Phys. **92**, 1216–1220 (2002).
44. A. Patelli, J. Ravagnan, V. Rigato, G. Salmaso, D. Silvestrini, E. Bontempi, and L. E. Depero, "Structure and interface properties of Mo/B_4C/Si multilayers deposited by rf-magnetron sputtering," Appl. Surf. Sci. **238**, 262–268 (2004).
45. I. Nedelcu, R. W. E. van de Kruijs, A. E. Yakshin, and F. Bijkerk, "Microstructure of Mo/Si multilayers with B_4C diffusion barrier layers," Appl. Opt. **48**, 155–160 (2009).
46. S. Braun, H. Mai, M. Moss, R. Scholz, and A. Leson, "Mo/Si Multilayers with Different Barrier Layers for Applications as Extreme Ultraviolet Mirrors," J. Appl. Phys. **41**, 4074 (2002).
47. J. I. Larruquert, "Reflectance enhancement in the extreme ultraviolet and soft x rays by means of multilayers with more than two materials," J. Opt. Soc. Am. A **19**, 391–397 (2002).
48. K. Le Guen, M.-H. Hu, J.-M. André, S. K. Zhou, H. C. Li, J. T. Zhu, Z. S. Wang, C. Meny, A. Galtayries, and P. Jonnard, "Observation of an asymmetrical effect when introducing Zr in Mg/Co multilayers," Appl. Phys. Lett. **98**, 251909–251909–3 (2011).
49. E. Meltchakov, A. Ziani, F. Auchere, X. Zhang, M. Roulliay, S. De Rossi, C. Bourassin-Bouchet, A. Jérome, F. Bridou, F. Varniere, and F. Delmotte, "EUV reflectivity and stability of tri-component Al-based multilayers," Proceeding SPIE 816819–816819 (2011).
50. J. Gautier, F. Delmotte, M. Roulliay, F. Bridou, M.-F. Ravet, and A. Jérome, "Study of normal incidence of three-component multilayer mirrors in the range 20-40 nm," Appl. Opt. **44**, 384–390 (2005).
51. J. Bosgra, E. Zoethout, A. M. J. van der Eerden, J. Verhoeven, R. W. E. van de Kruijs, A. E. Yakshin, and F. Bijkerk, "Structural properties of subnanometer thick Y layers in extreme ultraviolet multilayer mirrors," Appl. Opt. **51**, 8541–8548 (2012).
52. C. Montcalm, B. T. Sullivan, M. Ranger, J. M. Slaughter, P. A. Kearney, C. M. Falco, and M. Chaker, "Mo/Y multilayer mirrors for the 8-12 nm wavelength region," Opt. Lett. **19**, 1004–1006 (1994).
53. P. Gupta, T. P. Tenka, S. Rai, M. Nayak, and G. S. Lodha, "Interface smoothing of soft x-ray Mo/Y multilayer mirror by thermal treatment," J. Phys. Appl. Phys. **40**, 6684–6689 (2007)
54. P. Jonnard, H. Maury, K. Le Guen, J.-M. André, N. Mahne, A. Giglia, S. Nannarone, and F. Bridou, "Effect of B4C diffusion barriers on the thermal stability of Sc/Si periodic multilayers," Surf. Sci. **604**, 1015–1021 (2010).
55. M. Wormington, C. Panaccione, K. M. Matney, and D. K. Bowen, "Characterization of structures from X-ray scattering data using genetic algorithms," Philos. Trans. R. Soc. Lond. Ser. Math. Phys. Eng. Sci. **357**, 2827–2848 (1999).

56. S. Nannarone, F. Borgatti, A. DeLuisa, B. P. Doyle, G. C. Gazzadi, A. Giglia, P. Finetti, N. Mahne, L. Pasquali, M. Pedio, G. Selvaggi, G. Naletto, M. G. Pelizzo, and G. Tondello, "The BEAR Beamline at Elettra," AIP Conf. Proc. **705**, 450–453 (2004).

57.http://www2.lbl.gov/Science-Articles/Archive/sb/Oct-2004/1-ALS-What-Lies Beneath.html

58. J.-M. André, A. Avila, R. Barchewitz, R. Benbalagh, R. Delaunay, D. Druart, P. Jonnard, and H. Ringuenet, "MONOX: a characterization tool for the X-UV range," Eur. Phys. J. Appl. Phys. **31**, 147–152 (2005).

59. D. Drouin, A. R. Couture, D. Joly, X. Tastet, V. Aimez, and R. Gauvin, "CASINO V2.42: a fast and easy-to-use modeling tool for scanning electron microscopy and microanalysis users," Scanning **29**, 92–101 (2007).

60. C. Bonnelle, F. Vergand, P. Jonnard, J.-M. André, P. F. Staub, P. Avila, P. Chargelègue, M.-F. Fontaine, D. Laporte, P. Paquier, A. Ringuenet, and B. Rodriguez, "Instrument for research on interfaces and surfaces," Rev. Sci. Instrum. **65**, 3466–3471 (1994).

61. H. H. Johann, "Die Erzeugung lichtstarker Röntgenspektren mit Hilfe von Konkavkristallen," Z. Für Phys. **69**, 185–206 (1931).

62. T. Feigl, S. Yulin, N. Kaiser, and R. Thielsch, "Magnetron sputtered EUV mirrors with high thermal stability," Proc. SPIE, **3997**, 420–430 (2000).

63. F. Choueikani, F. Bridou, B. Lagarde, E. Meltchakov, F. Polack, P. Mercere, and F. Delmotte, "X-ray properties and interface study of B_4C/Mo and B_4C/Mo_2C periodic multilayers," Appl. Phys. A **111**, 191–198 (2013).

64. G. K. Johnson, W. N. Hubbard, and E. K. Storms, "The enthalpies of formation of Mo_2C(c) and Mo_3C_2(c) by fluorine bomb calorimetry," J. Chem. Thermodyn. **9**, 1021–1026 (1977).

65. A. K. Petford-Long, Amanda K, M. B. Stearns, C.-H. Chang, S. R. Nutt, D. G. Stearns, N. M. Ceglio, and A. M. Hawryluk, "High resolution electron microscopy study of x-ray multilayer structures," J. Appl. Phys. **61**, 1422 –1428 (1987).

66. M.-H. Hu, K. Le Guen, J.-M. André, S. K. Zhou, H. C. Li, J. T. Zhu, Z. S. Wang, C. Meny, N. Mahne, A. Giglia, S. Nannarone, I. Estève, M. Walls, and P. Jonnard, "Investigation of the thermal stability of Mg/Co periodic multilayers for EUV applications," Appl. Phys. A **106**, 737–745 (2011).

67. "http://henke.lbl.gov/optical_constants/," http://henke.lbl.gov/optical_constants/.

68. G. A. Valkovskiy, M. V. Baidakova, P. N. Brunkov, S. G. Konnikov, M. A. Yagovkina, and J. M. Zadiranov, "Study of roughness in multilayer Mo-Si mirrors," Phys. Status Solidi - Appl. Mater. Sci. **208**, 2623–2628 (2011).

69. M. Nayak, G. S. Lodha, and R. V. Nandedkar, "X-ray reflectivity investigation of interlayer at interfaces of multilayer structures: application to Mo/Si multilayers," Bull. Mater. Sci. **29**, 693–700 (2006).

70. M. K. Tiwari and K. J. S. Sawhney, "Structural characterization of thin layered materials using x-ray standing wave enhanced elastic and inelastic scattering measurements," J. Phys. Condens. Matter **22**, 175003 (2010).

71. J.-M. André, K. Le Guen, and P. Jonnard, "Oscillating dipole model for the X-ray standing wave enhanced fluorescence in periodic multilayers," Spectrochim. Acta Part B At. Spectrosc. **85**, 55–61 (2013).

72. http://forge.epn-campus.eu/projects/ppm.

73. D. de Boer, "Glancing-incidence x-ray fluorescence of layered materials," Phys. Rev. B **44**, 498–511 (1991).

74."http://www.elettra.trieste.it/images/Documents/BEAR/files/guide_fluorescence_detector.pdf,".

75. S. Döring, F. Schönbohm, D. Weier, F. Lehmkühler, U. Berges, M. Tolan, C. S. Fadley, and C. Westphal, "Standing-wave excited photoemission experiments on Si/$MoSi_2$ multilayer

mirrors in the soft x-ray regime: An analytical modeling approach," J. Appl. Phys. **106**, 124906 (2009).

76. N. Mahne, A. Giglia, L. Sponza, A. Verna, and S. Nannarone, "Soft-X study of buried interfaces in stratified media," seventh international conference on thin film physics and applicatons, international society for optics and photonics, 79951S–79951S–9 (2010).

77. N. Mahne, A. Giglia, S. Nannarone, J. Bertoli, V. Mattarello, and V. Rigato, "Quantitative modelization of particle emission from excited solids: application to spectroscopic diagnostics of buried interfaces in multilayeR," Proc. SPIE 65860V-65860V-10 (2007).

78. P. Reinke and P. Oelhafen, "The molybdenum–carbon interface: formation and electronic structure of the carbide layer," Surf. Sci. **468**, 203–215 (2000).

79. L. G. Jacobsohn, R. K. Schulze, M. E. H. Maia da Costa, and M. Nastasi, "X-ray photoelectron spectroscopy investigation of boron carbide films deposited by sputtering," Surf. Sci. **572**, 418–424 (2004).

80. S. S. Perry and G. A. Somorjai, "Reaction layer formation and fracture at chemically vapor deposited diamond/metal interfaces," J. Vac. Sci. Technol. Vac. Surf. Films **12**, 1513–1518 (1994).

81. V. I. T. A. de Rooij-Lohmann, A. E. Yakshin, R. W. E. van de Kruijs, E. Zoethout, A. W. Kleyn, E. G. Keim, M. Gorgoi, F. Schäfers, H. H. Brongersma, and F. Bijkerk, "Enhanced diffusion upon amorphous-to-nanocrystalline phase transition in Mo/B_4C/Si layered systems," J. Appl. Phys. **108**, 014314–014314–5 (2010).

82. H. L. Bai, E. Y. Jiang, C. D. Wang, and R. Y. Tian, "Enhancement of the reflectivity of soft-x-ray Co/C multilayers at grazing incidence by thermal treatment," J. Phys. Condens. Matter **8**, 8763 (1996).

83. F. J. A. den Broeder, D. Kuiper, A. P. van de Mosselaer, and W. Hoving, "Perpendicular Magnetic Anisotropy of Co-Au Multilayers Induced by Interface Sharpening," Phys. Rev. Lett. **60**, 2769–2772 (1988).

84. S. Luby and E. Majkova, "Tailoring of multilayer interfaces by pulsed laser irradiation," Appl. Surf. Sci. **248**, 316–322 (2005).

85. H. L. Bai, E. Y. Jing, and C. D. Wang, "Interdiffusion in Co/C soft X-ray multilayer mirrors," Thin Solid Films **286**, 176–183 (1996).

86. H. L. Bai, E. Y. Jiang, and C. D. Wang, "Interdiffusion in CoN/CN soft X-ray multilayer mirrors," Thin Solid Films **304**, 278–285 (1997).

87. K. Le Guen, M.-H. Hu, J.-M. André, P. Jonnard, Z. Wang, J. Zhu, A. Galtayries, C. Mény, E. Meltchakov, C. Hecquet, and F. Delmotte, "Characterization of EUV periodic multilayers," X-Ray Spectrom. **40**, 338–342 (2011).

88. V. R. Galakhov and S. N. Shamin, "Ultrasoft X-ray spectroscopy with variation of the electron excitation energy as a method for analyzing thin films and solid/solid interfaces," Bull. Russ. Acad. Sci. Phys. **73**, 896–898 (2009).

89. S. Hosokawa, H. Sato, Y. Wang, E. Ohata, and A. Fukushima, "Soft X-ray emission study of nano-structured carbon," J. Electron Spectrosc. Relat. Phenom. **137–140**, 235–237 (2004).

90. M. Malinowska, C. Mény, E. Jedryka, and P. Panissod, "The anisotropic first-neighbour contribution to the hyperfine field in hexagonal-close-packed Co: a nuclear magnetic resonance study of diluted alloys and multilayers," J. Phys. Condens. Matter **10**, 4919–4928 (1998).

91. S. Zoll, A. Dinia, J. P. Jay, C. Mény, G. Z. Pan, A. Michel, L. El Chahal, V. Pierron-Bohnes, P. Panissod, and H. A. M. Van den Berg, "Influence of the growth technique on the coupling and magnetoresistance of Co/Ru sandwiches," Phys. Rev. B **57**, 4842–4848 (1998).

92. A. Giglia, S. Mukherjee, N. Mahne, S. Nannarone, P. Jonnard, K. Le Guen, Y.-Y. Yuan, J.-M. André, Z.-S. Wang, H.-C. Li, and J.-T. Zhu, "Thermal effects on Co/Mo_2C multilayer

mirrors studied by soft x-ray standing wave enhanced photoemission spectroscopy," Proc. SPIE, 87770I-87770I-10 (2013).
93. K. Ishida and T. Nishizawa, "The C-Co (Carbon-Cobalt) system," J. Phase Equilibria **12**, 417–424 (1991).
94. C. P. Heijwegen and G. D. Rieck, "Determination of the phase diagram of the Mo-Co system using diffusion couples," J. Common Met. **34**, 309–314 (1974).
95. K. P. Gupta, "The Co-Mo-W system (Cobalt-Molybdenum-Tungsten)," J. Phase Equilibria **23**, 274–275 (2002).
96. J. M. Newsam, A. J. Jacobson, L. E. McCandlish, and R. S. Polizzotti, "The structures of the η-carbides Ni_6Mo_6C, Co_6Mo_6C, and $Co_6Mo_6C_2$," J. Solid State Chem. **75**, 296–304 (1988).
97. N. Das, J. Mittra, B. S. Murty, S. K. Pabi, U. D. Kulkarni, and G. K. Dey, "Miedema model based methodology to predict amorphous-forming-composition range in binary and ternary systems," J. Alloys Compd. **550**, 483–495 (2013).
98. H.-L. Bai, E.-Y. Jiang, R.-Y. Tian, and C.-D. Wang, "Aging effect of Co/C soft X-ray multilayer mirrors," Chin. Sci. Bull. **42**, 454–457 (1997).
99. C. C. Tripathi, M. Kumar, and D. Kumar, "Atom beam sputtered Mo_2C films as a diffusion barrier for copper metallization," Appl. Surf. Sci. **255**, 3518–3522 (2009).
100. C. Montcalm, B. T. Sullivan, S. Duguay, M. Ranger, W. Steffens, H. Pépin, and M. Chaker, "In situ reflectance measurements of soft-x-ray/extreme-ultraviolet Mo/Y multilayer mirrors," Opt. Lett. **20**, 1450–1452 (1995).
101. C. Meny, E. Jedryka, and P. Panissod, "Satellite structure of ^{59}Co NMR spectra in some Co alloys," J. Phys. Condens. Matter **5**, 1547–1556 (1993).
102. Y. G. Chen and B. X. Liu, "Amorphous films formed by solid-state reaction in an immiscible Y–Mo system and their structural relaxation," Appl. Phys. Lett. **68**, 3096 (1996).
103. B. Kjornrattanawanich and S. Bajt, "Structural Characterization and Lifetime Stability of Mo/Y Extreme-Ultraviolet Multilayer Mirrors," Appl. Opt. **43**, 5955–5962 (2004).
104. B. X. Liu and Z. J. Zhang, "Interface-generated vitrification in the Y - Mo system with a small positive heat of mixing," J. Phys. Condens. Matter **8**, L165–L171 (1996).
105. M. J. H. Kessels, F. Bijkerk, F. D. Tichelaar, and J. Verhoeven, "Determination of in-depth density profiles of multilayer structures," J. Appl. Phys. **97**, 093513–093513–8 (2005).
106. A. R. Miedema, P. F. de Châtel, and F. R. de Boer, "Cohesion in alloys - fundamentals of a semi-empirical model," Phys. BC **100**, 1–28 (1980).
107. A. K. Niessen and A. R. Miedema, "The “Macroscopic Atom” Model: An Easy Tool to Predict Thermodynamic Quantities - Springer," Thermochem. Alloys **286**, 29–54 (1989).

Appendix Π: other publications

Publications as co-author:

[1]. Qi Zhong, Zhong Zhang, Wenbin Li, Jingtao Zhu, Zhanshan Wang, Philippe Jonnard, Karine Le Guen, Yanyan Yuan, Jean-Michel André, Hongjun Zhou, and Tonglin Huo. Al/Zr multilayer mirror and its thermal stability for EUV application. Journal of Physics: conference series **425**,152010 (2013).

[2]. Qi Zhong, Wenbin Li, Zhong Zhang, Jingtao Zhu, Qiushi Huang, Haochuan Li, Zhanshan Wang, Philippe Jonnard, Karine Le Guen, Yanyan Yuan, Jean-Michel André, Hongjun Zhou, and Tonglin Huo. Opical performance, structure and thermal stability of Al(1wt.-%Si)/Zr and Al/Zr multilayers designed for the 17-19nm range. Chinese Optics Letters, **11**, S10603 (2013).

[3]. Qi Zhong, Zhong Zhang, Jingtao Zhu, Zhanshan Wang, Philippe Jonnard, Karine Le Guen, Yanyan Yuan, Jean-Michel André, Hongjun Zhou, and Tonglin Huo. The thermal stability of Al(1%wtSi)/Zr EUV mirrors. Applied Physics A-Materials Science & Processing. **1,** 133-138 (2012).

We also participated in the study of Al/Zr systems. This system was mainly studied by the Tongji University of Shanghai collaborating with our team. The Al-based systems were developed to work at the near normal incidence in the range of 17-19 nm. Al can be a good spacer in the multilayer structure owing to its low absorption. Al/Zr multilayer has shown promising optical performance in the EUV region. We studied the optical properties and thermal stability of two kinds of Al/Zr (Al(1%wtSi)/Zr and Al(pure)/Zr) multilayers with the same period number. Al(1%wtSi) layers were deposited by using the Al target with 1% weight ratio of Si. They were prepared by using DC magnetron sputtering. We used the non-destructive, XRR, XRD, EUV, XES and destructive, TEM characterization techniques to investigate optical performance and thermal stability of both systems. All these techniques were also employed in the characterization of Co-based multilayer.

The Al/Zr (Al(1%wtSi)/Zr and Al(pure)/Zr) multilayers showed different optical and structural performances because of the presence of silicon in the Al layers. The thermal stability of the two systems annealed up to 500°C was investigated. They show the first significant structural changes after annealing at 250°C. The interlayers were transformed from symmetrical to asymmetrical, where the Zr-on-Al interlayers are thicker than the Al-on-Zr interlayers. In order to verify the reaction temperature of the transformation in two systems, a detailed annealed procedure was performed. The results show that at low temperature the interfaces consist of amorphous Al-Zr alloy, then at 295°C for Al(pure)/Zr and 298°C for Al(1wt.-%Si)/Zr, they transform to polycrystalline Al-Zr alloy. This can decrease the surface roughness and smooth the interfaces. Above 300°C, the interdiffusion becomes larger, which can enlarge the differences between Zr-on-Al and Al-on-Zr interlayers.

Based on these analyses, it is demonstrated that the doping of Si into the Al layers can smooth the interfaces, disfavor the crystallization of Al layer and consequently results in an increase of reflectivity of the (Al(1%wtSi)/Zr multilayer with respect to the (Al(pure)/Zr multilayer.

11th International Conference on Synchrotron Radiation Instrumentation (SRI 2012) IOP Publishing
Journal of Physics: Conference Series **425** (2013) 152010 doi:10.1088/1742-6596/425/15/152010

Al/Zr multilayer mirror and its thermal stability for EUV application

Qi Zhong,[1] Zhong Zhang,[1] ,Wenbin Li, [1] Jingtao Zhu,[1] Zhanshan Wang,[1, *] Philippe Jonnard,[2] Karine Le Guen,[2] Yanyan Yuan,[2] Jean-Michel André,[2] Hongjun Zhou,[3] and Tonglin Huo[3]

[1] MOE Key Laboratory of Advanced Micro-Structured Materials, Institute of Precision Optical Engineering, Department of Physics, Tongji University, Shanghai 200092, China

[2] Laboratoire de Chimie Physique – Matière Rayonnement, UPMC Univ Paris 06, CNRS UMR 7614, 11 rue Pierre et Marie Curie, F-75231 Paris cedex 05, France

[3] National Synchrotron Radiation Laboratory, University of Science and Technology of China, Hefei 230029, China

E-mail: *wangzs@tongji.edu.cn

Abstract. Two kinds of Al/Zr (Al(1%wtSi)/Zr and Al(Pure)/Zr) multilayers in the region of 17-19nm were deposited on fluorine doped tin oxide coated glass by using direct–current magnetron sputtering technology. Based on the fitting data of grazing incident X–ray reflection and near–normal incident (EUV) reflectance, the interfacial roughness in the Al(1%wtSi)/Zr is lower than that in Al(Pure)/Zr because of the presence of silicon in Al. For the further characterization of Al(1%wtSi)/Zr multilayers, six samples deposited on Si substrates were annealed from 100 °C to 500 °C temperature in a vacuum furnace for 1 h. Based on the results of EUV and X-ray diffraction, the Al(1%wtSi)/Zr multilayer has a stable structure up to 200 °C, and keeps almost the similar EUV reflectivity as the non-annealed sample. After 300 °C, the amorphous of Al-Zr alloy is transformed to polycrystalline in the interface, which could be the reason for the decrease of EUV reflectivity. The polycrystalline Al-Zr compound does not destroy the multilayer completely even up to 500 °C.

1. Introduction

With the research of reflective multilayer coatings in the extreme ultraviolet (EUV) spectral region in the practical applications [1-2], the Al–based [3–6] systems are widely researched in the recent years to meet the practical requirements. Owing to the low absorption below the Al L-edge near 17 nm, the Al can be a good spacer layer in the multilayer combination. However, there are two problems the Al-based multilayer: the inhomogeneous crystallization of Al and the interdiffusion [3]. Recently, Al/Zr multilayer has shown very promising performance in the EUV region [4-6]. From the analysis of Al(1.0%wtSi)/Zr periodic multilayer with a large number of periods in our previous paper [5], we found that the interfacial roughness is not constant throughout the sample, the roughness being smaller in the first 40 periods and then increasing in the upper layers in a large number of periods of the Al(1.0%wtSi)/Zr periodic multilayer. However, the optical performance of Al(1.0%wtSi)/Zr with 40 periods was limited by the variable interfacial structure. In the extreme ultraviolet (EUV) spectral regions, the solar corona is rich with line emission from a variety of ions, formed at plasma temperatures of up to several million degrees. Therefore for the solar satellite instruments, beside the high reflectivity, the thermal stability of multilayer is another crucial problem for the practical application [1-2]. However, the thermal stability of Al(1%wtSi)/Zr multilayer has not been evaluated yet.

In this paper, we describe the performance of the Al(1%wtSi)/Zr multilayers for the purpose of coating the multilayer on normal-incidence telescopes tuned to specific emission lines (i.e. Fe-IX (λ=17.1 nm), Fe-XI (λ=18.0 nm) and Fe-XII (λ=19.3 nm)) in the wavelength range of λ~17-19nm. The experimental process is described in the Sec.2. In Sec.3–1, two different multilayer types (Al(1%wtSi)/Zr and Al(Pure)/Zr) with different periods (N=40, 60) are presented. The grazing incident X–ray reflection (GIXR) and near–normal incident EUV reflectance are used to investigate the structure properties of the multilayers. To fully estimate the Al(1%wtSi)/Zr multilayer, the effect of the thermal stability is discussed in the Sec.3–2. We conclude in Sec.4 with comments regarding the performance for the Al/Zr system.

2. Experimental methods

All samples were fabricated by direct–current magnetron sputtering technology [5-7] with the base pressure 8.0×10^{-5}Pa. The sputtering targets with diameter of 100 mm were zirconium (99.5%), aluminum (99.999%, Al(Pure)) and silicon doped in aluminum (Al(1%wtSi)). Under a 0.18 Pa argon (99.9999% purity) pressure, the samples deposited on fluorine doped tin oxide coated glass (FTO) substrates are Al(1%wtSi)/Zr (N=40, 60) and Al(Pure)/Zr (N=40, 60). While six Al(1%wtSi)/Zr multilayers were consisted of 40 bi-layers, deposited on Si polished wafers. The thicknesses of the samples on FTO are around 9.1 nm, and gamma values are 0.35, which were designed to have a high reflectivity at near 18 nm region at 5° incident angle by synchrotron radiation. While the thickness of the sample on Si wafers are around 9.3 nm, and gamma values are 0.34.

For characterizing the structure of the samples, the GIXR and XRD measurements were performed using a Cu Kα source (λ=0.154 nm). The EUV reflectivity measurements were made at a 5 ° incident angle, using the reflectometer at the Spectral Radiation Standard and Metrology Beamline and Station (beamline U26) at the National Synchrotron Radiation Laboratory in Hefei, China.

3. Results and discussions

3.1 Al (1%wtSi)/Zr and Al (Pure)/Zr multilayers

In order to estimate the influence of Si doping in the Al layers [3], we firstly compare two systems of Al (1%wtSi)/Zr and Al (Pure)/Zr with the same period numbers (40 and 60). Fig.1(a) shows the x-ray reflectivity obtained by GIXR and the best-fitted curves with four layer model [6] used the Bede Refs software (genetic algorithm) [8] for the Al (1%wtSi)/Zr and Al (Pure)/Zr samples with 40 periods. The calculated root-mean-square (rms) roughness was about 0.95 nm for the Al(1%wtSi) layers and was about 0.4 nm for the Zr layers. Both rms of Al-on-Zr, Zr-on-Al interlayers were 0.5 nm. While with the similar rms for the Al-on-Zr, Zr-on-Al interlayers and Zr layers in the Al (Pure)/Zr multilayers, only the rms of Al (Pure) layer was larger than that of Al(1%wtSi) layer in 0.2 nm. For the 60 periods, the

11th International Conference on Synchrotron Radiation Instrumentation (SRI 2012) IOP Publishing
Journal of Physics: Conference Series **425** (2013) 152010 doi:10.1088/1742-6596/425/15/152010

situation is similar, which the Al(Pure) layer has larger roughness. The measured and simulated EUV reflectivity curves are shown in Fig.1(b). With the same fitting models in GIXR, the reflectance of periods 40 and 60 are only 37.9 % at 17.8 nm and 33.2 % at 18.2 nm, while the values in Al(1%wtSi)/Zr system are 41.2 % at 17.8 nm and 37.8 % at 18.0 nm, respectively. The lower reflectance of Al(Pure)/Zr multilayers indicate the higher interfacial roughness in this multilayer systems, consistent with the fitting data in the GIXR. From the above analyses, it can be seen that the Si doping in Al layers can influence the reflectivity for the two system, where the Al (1%wtSi)/Zr multilayers have higher values than those of Al (Pure)/Zr. Therefore, we decide to focus on Al (1%wtSi)/Zr system to characterize its thermal stability.

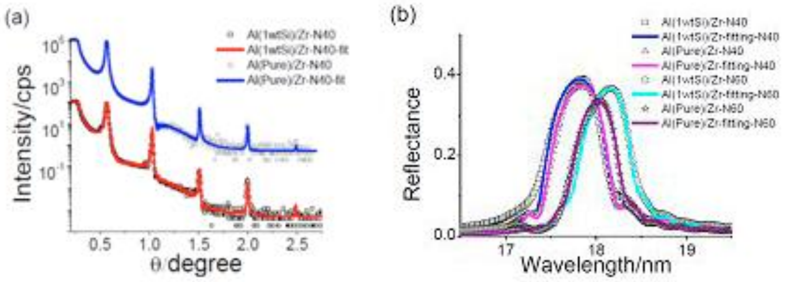

Fig.1 (a) The curves of fitting data with 40 periods for Al (1%wtSi)/Zr (red solid line) and Al (Pure)/Zr (blue line and symbol) are presented, the experimental measurements (black open points) are also shown in it; (b) (Color online) Measured and simulated reflectance versus wavelength of the multilayers at 5° incident angle by synchrotron radiation.

3.2 The thermal stability of Al (1%wtSi)/Zr multilayer

In the previous section, we found that the Al(1%wtSi)/Zr multilayer had better optical performance in the region of 17-19 nm. Except for the higher reflectance, the thermal stability of the multilayers should also be concerned in the practical applications. Therefore, the five multilayer samples, except for room temperature (RT) sample, were annealed at temperatures of 100, 200, 300, 400 and 500 °C in a vacuum furnace for 1 h, respectively. After annealing at different temperatures, the samples were cooled to room temperature naturally in a vacuum furnace with a base pressure of 3×10^{-4} Pa. In Fig.2(a), the measured EUV reflectivity curves are shown. The measured reflectivity (40.4%) is lower that the value calculated theoretically (70.9%) because of different impact factors [6]. With the increasing annealing temperature, the reflectivity increases to 41.7 % at 100 °C, and then down to 16.2 % at 500 °C. Before 300 °C, the peak positions of different annealing samples maintains at 18.5 nm. From 300 °C, the peak position moves to 18.3 nm, and apparently shifted to 17.9 nm at 500 °C.

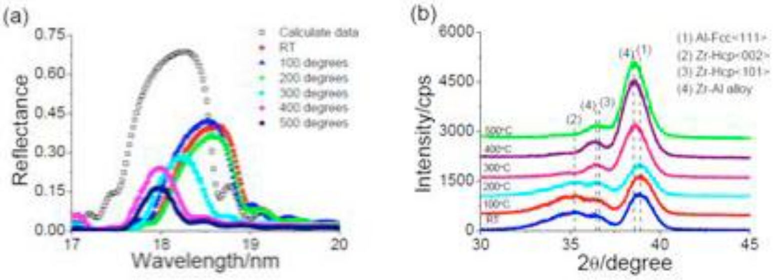

Fig.2 (a) (Color lines) Measured reflectivity versus wavelength of the multilayers at 5° incident angle by synchrotron radiation. b: Diffraction curves of the samples of Al(1%wtSi)/Zr (color lines) with different annealed temperatures (RT, 100 °C, 200 °C, 300 °C, 400 °C and 500 °C).

As shown in Fig. 2 (b), different XRD patterns are observed for different annealed samples. Before 300 °C, there are three main peaks: 38.7 ° (Al<111>), 35.3 ° (Zr<002>), 36.5 ° (Zr<101>) in the XRD pattern of the samples (RT, 100 °C, 200 °C). Based on the results of EUV measurements for 100 °C sample, we found that the crystallization of Zr could influence EUV reflectivity and decrease the interfacial roughness. From 300 °C, all main peaks are changed. When the temperature is at 500 °C, the peak positions of both Al<111> and Zr<101> are decreased 0.2 °, which show that a new polycrystalline Al-Zr alloy compound may be formed at the interface. The Zr<002> peak still has a small contribution around 35.3 ° in the curves. Thus, we can conclude the Zr material still exists at 500 °C. The phases of polycrystalline Al-Zr alloy could be about the similar positions as Al<111> and Zr<101>, which shift the peak positions in the Fig.2 (b). Based on our previous paper [6], the interlayers of RT sample consisted of an amorphous Al-Zr alloy in the multilayer. Considering the results in the XRD (Fig. 2 (b)), the multilayer consist of a similar multilayer structure before 300 °C, which cannot influence the main peaks in the XRD patterns. While from 300°C, the amorphous Al-Zr alloy may be transformed to polycrystalline Al-Zr alloy. That is why all the peaks show the different peak positions in the XRD patterns. This structural change of the multilayer between 200 and 300 °C should be the main reason for the decrease of EUV reflectivity (Fig. 2 (a)). It can be concluded that the new polycrystalline Al-Zr compounds increases the interfacial roughness and degrades the optical contrast of the multilayer structure.

4. Conclusion

The two systems of the Al(1%wtSi)/Zr and Al(Pure)/Zr multilayers in the 17-19 nm are presented. According to the analyses of the GIXR and EUV, the Si doping in Al layer has a great influence on the roughness of Al layer and increases the reflectivity of the Al(1%wtSi)/Zr multilayer in both periods (N=40, 60). To further evaluate performance of Al(1%wtSi)/Zr multilayer, we deposited six samples to detect the thermal stability in different annealing temperatures. Based on the analyses of EUV, the multilayer samples annealed up to 100 °C, show higher peak reflectivity than the RT sample. The reflectivity does not decrease apparently before 300 °C. However from 300 °C, the interfacial structure of Al-Zr alloy was transformed from amorphous to the polycrystalline, which increases the interdiffusion between the Al and Zr layers and decreases the EUV reflectivity. At 500 °C, the new formed compounds Al-Zr alloy in the interfaces cannot destroyed the periodic structure of the Al(1%wtSi)/Zr multilayer completely. Therefore, in our experiment, we can concluded that the Al(1%wtSi)/Zr multilayer has a good optical performance and stable structure up to 200 °C, which is considered to be very valuable for further practical applications.

Acknowledgments

This work is supported by National Basic Research Program of China (No. 2011CB922203), National Natural Science Foundation of China (No.10825521, 11061130549).

References

11th International Conference on Synchrotron Radiation Instrumentation (SRI 2012) IOP Publishing
Journal of Physics: Conference Series **425** (2013) 152010 doi:10.1088/1742-6596/425/15/152010

[1] J. Corso, P. Zuppella, P. Nicolosi, D. L. Windt, E. Gullikson and M. G. Pelizzo, 2011 *Opt. Express* **19** 13963

[2] S. Bajt, J. B. Alameda, T. W. Barbee Jr.,W. M. Clift, J. A. Folta, B. Kaufmann and E. A. Spiller, 2002 *Opt. Eng.* **41** 1797

[3] E. Meltchakov, C. Hecquet, M. Roulliay, S. D. Rossi, Y. Menesguen, A. Jérome, F. Bridou, F. Varniere, M.-F. Ravet-Krill and F. Delmottel, 2010 *Appl. Phys. A* **98** 111

[4] D.L. Voronov, E.H. Anderson, R. Cambie, S. Cabrini, S.D. Dhuey, L.I. Goray, E.M. Gullikson, F. Salmassi, T. Warwick, V.V. Yashchuk and H.A. Padmore, 2011 *Opt. Express* **19** 6320

[5] Qi Zhong, Wenbin Li, Zhong Zhang, Jingtao Zhu, Qiushi Huang, Chuanchun Yang, Zhanshan Wang, P. Jonnard, K. Le Guen, J.-M. André, Hongjun Zhou and Tonglin Huo, 2012 *Opt. Express* **20** 10692

[6] Qi Zhong, Zhong Zhang, Jingtao Zhu, Zhanshan Wang, P. Jonnard, K. Le Guen and J.-M. André, 2012 *Appl. Sur. Sci.* **259** 371

[7] Wang Fengli, Wang Zhanshan, Zhang Zhong, Wu Wenjuan, Wang Hongchang, Zhang Shumin, Qin Shuji and Chen Lingyan, 2005 *Opt. Precision Eng.* **13** 28 (In Chinese)

[8] M. Wormington, C. Panaccione, K. Matney and D. Bowen, 1999 *Phil. Trans. R. Soc. Lond. A* **357** 2827

COL 11(Suppl.), S10603(2013) CHINESE OPTICS LETTERS June 30, 2013

Optical performance, structure and thermal stability of Al(1wt.-%Si)/Zr and Al(pure)/Zr multilayers designed for the 17–19 nm range

Qi Zhong (钟 奇)[1], Wenbin Li (李文斌)[1], Zhong Zhang (张 众)[1], Jingtao Zhu (朱京涛)[1], Qiushi Huang (黄秋实)[1], Haochuan Li (李浩川)[1], Zhanshan Wang (王占山)[1*], Philippe Jonnard[2], Karine Le Guen[2], Yanyan Yuan[2], Jean-Michel André[2], Hongjun Zhou (周红军)[3], and Tonglin Huo (霍同林)[3]

[1] *Department Institute of Precision Optical Engineering, Department of Physics,*
Tongji University, Shanghai 200092, China

[2] *Laboratoire de Chimie Physique-Matière Rayonnement, UPMC Univ. Paris 06, CNRS UMR 7614,*
11 rue Pierre et Marie Curie, F-75231 Paris cedex 05, France

[3] *National Synchrotron Radiation Laboratory, University of Science and Technology of China,*
Hefei 230029, China

* *Corresponding author: wangzs@tongji.edu.cn*

Received December 6, 2012; accepted December 29, 2012; posted online June 7, 2013

We report on the optical performance, structure and thermal stability of periodic multilayer films containing Zr and Al(1wt.-%Si) or Al(pure) layers designed for the use as extreme ultraviolet (EUV) high reflective mirrors in the range of 17–19 nm. The comparison of Al/Zr (Al(1wt.-%Si)/Zr and Al(pure)/Zr) multilayers fabricated by direct-current magnetron sputtering shows that the optical and structural performances of two systems have much difference because of Si doped in Al. From the results of grazing incidence X-ray reflection (GIXR), X-ray diffraction (XRD), and EUV, the Si can disfavor the crystallization of Al and smooth the interface, consequently increase the reflectance of EUV in the Al(1wt.-%Si)/Zr systems. For the thermal stability of two systems, the first significant structural changes appear at 250 °C. The interlayers are transformed from symmetrical to asymmetrical, where the Zr-on-Al interlayers are thicker than Al-on-Zr interlayers. At 295 °C for Al(pure)/Zr and 298 °C for Al(1wt.-%Si)/Zr, the interfaces consist of amorphous Al-Zr alloy transform to polycrystalline Al-Zr alloy which can decrease the surface roughness and smooth the interfaces. Above 300 °C, the interdiffusion becomes larger, which can enlarge the differences between Zr-on-Al and Al-on-Zr interlayers. Based on the analyses, the Si doped in Al cannot only influence the optical and structural performances of Al/Zr systems, but also impact the reaction temperatures in the annealing process.

OCIS codes: 310.4165, 310. 6860, 310.6870.
doi: *10.3788/COL201311.S10603.*

With the research of reflective multilayer coatings in the extreme ultraviolet (EUV) spectral region in the practical application, preference is often given to the Mo/Si multilayers owing to its most advanced technological levels. This kind of multilayers have been already used in the Solar-B/EIS instrument, which could detect specific coronal or transition-region emission lines in two wavelength regions (17–21 and 25–29 nm)[1,2]. Owing to the large absorption of Si at longer wavelength region below Si L-edge, Al-based[3−5] systems have been investigated to meet the practical requirements.

Because of the low absorption below the Al L-edge near 17 nm, the Al can be a good spacer layer in the new multilayer combination. In Al-based systems, Al/Zr multilayers has the highest theoretical reflectance which makes it especially attractive for the EUV applications, such as blazed multilayer grating structure[4,6] and high reflective multilayer coatings[7]. In our previous works[7−9], the optical, structural performances and thermal stability of Al(1-%wt.Si)/Zr multilayers had been presented in details. We found four factors (the inhomogeneous crystallization of aluminum, contamination of the multilayer, surface oxidized layer, and interdiffusion between Al and Zr layers) could decreased the theoretical reflectance of Al(1.-%wt.Si)/Zr multilayer with 40 periods from 70.9% to 41.2% at 5° incident angle in the experiment. The thermal stability of six Al(1wt.-%Si)/Zr multilayers, except the room temperature (RT) samples, annealed at different temperatures (10, 200, 300, 400, and 500 °C) were characterized by a series of complementary measurements including grazing incidence X-ray reflection (GIXR), X-ray diffraction (XRD), X-ray emission spectroscopy (XES), and near-normal incident EUV reflection. Based on the simulation of GIXR and EUV, the symmetrical and asymmetrical interlayer models could be well matched with the multilayer structure blow and above 300 °C. At 200 °C, the degradation of the multilayer structure did not occure. The symmetrical interlayers still presented in the multilayers. However from 300 °C, the interface consisting of amorphous Al-Zr alloy had been transformed to the polycrystalline Al-Zr alloy, which decreased the EUV reflectance. And the Zr-on-Al interlayers become thicker than Al-on-Zr interlayers. Up to 500 °C, the multilayers structure still existed, where the reflectance contained at 17%. But the comparison of optical, structural performances, and thermal stability of the Al(1wt.-%Si)/Zr and Al(pure)/Zr systems in the wavelength region of 17–19 nm, especially for the influence of Si doped in Al, were not discussed in details[7].

In this letter, we report on the comparison of optical, structural performances and thermal stability of the Al(1wt.-%Si)/Zr and Al(Pure)/Zr systems for the purpose of investigating the difference between two systems and the performances of presence of Si in Al layers.

All samples were fabricated by direct current magnetron sputtering technology[7−9], under the base pressure of 8.0×10^{-5} Pa. The targets of Zr(99.5%) and Al(1wt.-%Si) or Al(pure, 99.999%) with diameter of 100 mm were used. The sputter gas was Ar with purity of 99.999%, and the gas pressure was held constantly at 1.35 ± 0.02 mTorr (0.180 Pa). The periodic thicknesses of Al(1wt.-%Si)/Zr and Al(pure)/Zr multilayers are 9.56 and 9.35 nm, respectively, while their gamma value (the ratio of Zr thickness to period) is 0.33. To compared the optical and structural performances between Al(1wt.-%Si)/Zr and Al(pure)/Zr multilayers, the samples were fabricated in which the period numbers of Al(1wt.-%Si)/Zr and Al(pure)/Zr are both held at 40 on FTO substrate. To evaluate the thermal stability of Al(1wt.-%Si)/Zr and Al(pure)/Zr systems, nine multilayer samples for each systems, except for RT sample, were deposited on the Si wafers, annealed at temperatures of 200, 250, 280, 285, 290, 295, 298, 300, 305, and 310 °C in a vacuum furnace for 1 h, respectively. After annealing the samples were cooled to RT naturally in the furnace with a base pressure of 4.5×10^{-4} Pa.

The GIXR and XRD measurements were carried out to test the changes in the multilayers, using an X-ray diffractometer working at the Cu Kα line (0.154 nm). The fitting calculations of GIXR curves were performed with Bede Refs software (genetic algorithm) to determine individual layer thickness and interface roughness[7,9,10].

The surface roughness was measured with a Veeco, Multi-Mode SPM scanning probe microscope, operated in atiomic force microscopy (AFM) mode. For estimating the interfacial microstructure and periodic structure of Al(1wt.-%Si)/Zr system, the scanning transmission electron microscope (TEM, FEI Tecnai G2 F20) was used on the specimen prepared by focused ion beam (FIB) etching using in the Materials Analysis Technology Ltd.

The reflectance of EUV was made at a 5° incident angle, using the reflectometer on the Spectral Radiation Standard and Metrology Beamline and Station (beamline U26) at the National Synchrotron Radiation Laboratory in Hefei, China. An Al filter was inserted into the incident light beam to remove the high order radiation.

In order to estimate the influence of Si doped in the Al layers[3], we firstly compare optical and structural performances of two systems (Al(1wt.-%Si)/Zr and Al (pure)/Zr) with 40 periods. Figure 1(a) shows the X-ray reflectance obtained by GIXR for the Al(1wt.-%Si)/Zr and Al(pure)/Zr samples. From the fitting data (not shown in the Fig. 1(a)), the calculated root-mean-square (RMS) roughness of Al(1wt.-%Si) and Zr layers are 1.0 and 0.4 nm, respectively. And the RMS of Al-on-Zr and Zr-on-Al interlayers are same, which value contains at 0.5 nm. While with the similar RMS for the Al-on-Zr, Zr-on-Al interlayers and Zr layers in the Al(1wt.-%Si)/Zr multilayers, only the RMS of Al(pure) layer was larger than that of Al(1wt.-%Si) layer in 0.2 nm. Therefore, the EUV reflectance measurements are needed to further characterize the two systems. The measured EUV reflectance curves are shown in Fig. 1(b). The peak reflectance of Al(1wt.-%Si)/Zr and Al(pure)/Zr are 41.2% at 17.8 nm and 37.9% at 17.8 nm, respectively. The higher reflectance of Al(1wt.-%Si)/Zr multilayers indicate, the better interface structure and the lower roughness in the multilayers, which consistent with the results in the GIXR analyses. Based on the measurements, we can assume that the Si doped in Al can influence the reflectance of the two systems, which Al(1wt.-%Si)/Zr multilayers have higher value than that of Al(pure)/Zr.

To identify the reason of different interfacial structures, the XRD measurements are required as shown in Fig. 2. Three phases (Fcc Al ⟨111⟩, Hcp Zr ⟨002⟩ and ⟨101⟩) are presented in both multilayers. The Al(pure) layer has an intact crystallization, but the crystallization of Al(1wt.-%Si) layer can be worse due to the material Si. Considering the scherrer formula[11], the crystal sizes of Al⟨111⟩ of Al(1wt.-%Si)/Zr (6.2 nm) is smaller than that of Al(pure)/Zr (6.3 nm). In particular, the surface and interfacial roughness are mainly influenced by the crystallization of Al[4]. Based on the results, we can conclude that a small proportion of Si in Al layers has a strong effect on the reflectance and structural performances of Al/Zr multilayers, where Al(1wt.-%Si)/Zr multilayers have higher reflectance and smoother interfacial roughness than that of Al(pure)/Zr.

To further evaluate the performances of Si doped in Al in the annealing process, the samples were deposited on the Si wafers. Based on the thermal stability of Al(1wt.-%Si)/Zr[9], the transformation from symmetrical

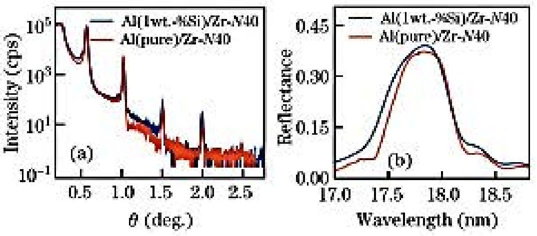

Fig. 1. (Color online) (a) Curves of fitting data with 40 periods for Al(1wt.-%Si)/Zr (blue solid line) and Al(pure)/Zr (red line) are presented; (b) measured reflectance versus wavelength of the multilayers at 5° incident angle by synchrotron radiation.

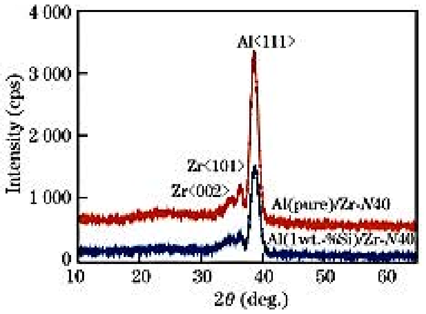

Fig. 2. (Color online) In tensity versus 2θ for XRD, the samples of Al(1wt.-%Si)/Zr (blue line) and Al(pure)/Zr (red line) with 40 periods are shown.

to asymmetrical interlayers appeared during the temperature from 200 to 300 °C. In order to verify the reaction temperatures of the transformation in two systems, eleven multilayer samples for each systems, except for RT sample, were annealed at temperatures of 200, 250, 280, 285, 290, 295, 298, 300, 305, and 310 °C in a vacuum furnace for 1 h. In Fig. 3, the periodic length of each multilayer sample is presented, where the values are normalized by those under the RT conditions. For Al(1wt.-%Si)/Zr multilayers (Fig. 3(a)), the periodic length of the multilayer first slightly decreases with the annealing temperature. At 200 °C, the relative change in the periodic length of the multilayer annealed is about 0.2%. From 250 °C, it sharply decreases to 0.5%, and from 290 to 310 °C, the changes contain at 0.8% of the initial value. For Al(pure)/Zr multilayers (Fig. 3(b)), the relative change is similar to the situation in Al(1wt.-%Si)/Zr multilayers. At 200 °C, the change is also about 0.2%, but above 250 °C, the slope of the changing trend is higher than that in the Al(1wt.-%Si)/Zr multilayers. The change is about 0.6% at 250 °C, and drops to 1.3% at 310 °C. Based on relative changes of periodic length in the GIXR measurements, the structural performances of Al(1wt.-%Si)/Zr is much better than that of Al(pure)/Zr. Because of large interdiffusion in both Al(1wt.-%Si)/Zr and Al(pure)/Zr multilayers at 250 °C, more and more amorphous Al-Zr alloy grows into Al and Zr layers, which can disturb the original balance in the interface boundary in the RT samples. That is to say, Zr diffuses and reacts more rapidly with Al than Al diffuses and reacts with Zr[12]. Therefore, the interfaces transform from symmetrical to asymmetrical in both multilayers. Thus, it is reasonable to suppose that the first reaction temperature is at 250 °C.

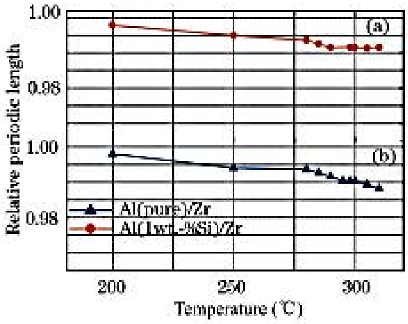

Fig. 3. (Color online) Relative periodic lengths of the Al/Zr multilayer samples (color curves) as a function of annealing temperature from RT to 310 °C. The periodic length is normalized to those of the samples before annealing.

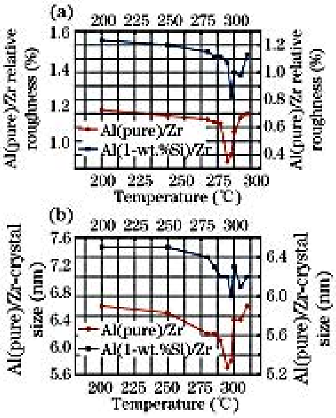

Fig. 4. (Color online) (a) Relative surface roughness of the Al(1wt.-%Si)/Zr (blue curve) and Al(pure)/Zr multilayers (red curve) as a function of annealing temperatures from 200 to 310 °C. The surface roughness is normalized by those of the samples before annealing. (b) The crystal sizes of all annealing samples in two systems are derived from the XRD measurements.

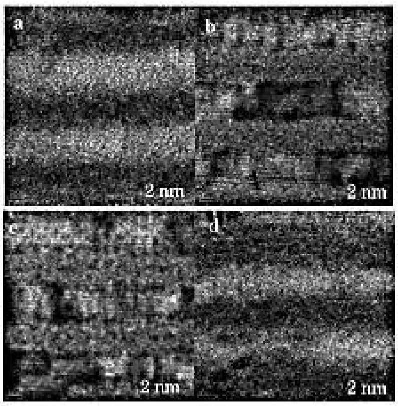

Fig. 5. (Color online) High magnification transmission electron micrographs used to observed the cross-section of five Al(1wt.-%Si)/Zr multilayers (Al layer-lighter, Zr layer-darker). The micrographs of the specimens at (a) RT, (b) 295, (c) 298, and (d) 300 °C.

The surface roughnesses of the Al(1wt.-%Si)/Zr and Al(pure)/Zr multilayers prior to and following annealing are characterized with AFM, measured over a 5× 5 (μm) area. In order to eliminate the effect of the roughness before annealing, the relative surface roughnesses of different annealing samples are used. To compare the two systems in Fig. 4(a), we can find that the changing trends first slightly decrease below 250 °C. Above 250 °C, the changes become obviously, which has the lowest point at 295 and 298 °C for Al(1wt.-%Si)/Zr and Al(pure)/Zr, respectively. With the lower surface roughness and different changing trends prior to and following those temperatures, we can assume that there is a reaction between Al and Zr layers. And the crystallization of Al is the main impact factor for the surface roughness. To estimate the relations between the crystallization of Al and surface roughness, the crystal sizes of Al⟨111⟩ from XRD measurements are presented in Fig. 4(b). From the curves, the changing trends is similar to the relative changes in the AFM in both systems, which also have the lowest point at 295 and 298 °C for Al(1wt.-%Si)/Zr and Al(pure)/Zr, respectively. Therefore, we can conclude that the surface roughness in both systems is influenced by the crystallization of Al. Because of the Si doped in Al, the reaction at the lowest points in the corresponding curves are different in Al(1wt.-%Si)/Zr and Al(pure)/Zr multilayers.

To verify the results of GIXR, AFM, and XRD in the annealing process, TEM observations were carried out. Because the similar changing trends between Al(1wt.-%Si)/Zr and Al(pure)/Zr multilayers, four specimens (RT, 295, 298, and 300 °C for Al(1wt.-%Si)/Zr systems) were made and analyzed on TEM (Fig. 5). In the RT samples (Fig. 5(a)), there is clearly an amorphous Al-Zr intermixed layer at each interface. The both thicknesses of interlayers are 1.5 nm. At 295 °C (Fig. 5(b)), the Zr-on-Al interlayers are thicker than Al-on-Zr interlayers, where the thicknesses are 1.9 and 1.7 nm, respectively. When annealed at 298 °C (Fig. 5(c)), the interlayers become much obvious. The interfaces consisting of amorphous Al-Zr alloy are transformed to polycrystalline Al-Zr alloy. The thicknesses of two interlayers still contain at 1.9 and 1.7 nm, respectively. While the surface and interfacial roughness becomes much lower and consistent with the results in the XRD. Up to 300 °C (Fig. 5(d)), the interdiffusion becomes larger. The thickness of Zr-on-Al interlayer (2.4 nm) is much thicker than that (2.0 nm) of Al-on-Zr interlayer.

In conclusion, we report on two systems, Al(1wt.-%Si)/Zr and Al(pure)/Zr multilayers, designed for the EUV region. The EUV reflectance reveals significantly, while the performances of the Al(1wt.-%Si)/Zr multilayer is much better than Al (pure)/Zr. The reflectance of Al(1wt.-%Si)/Zr multilayers are 41.2% at 17.8 nm for multilayers with 40 periods, which are higher than the value (37.9% at 17.8 nm) of Al(pure)/Zr multilayers. The presence of Si can disfavor the crystallization of Al and smooth the interfacial structure. To further detect the influence of Si doped in Al during the annealing process, the thermal stability of Al(1wt.-%Si)/Zr and Al(pure)/Zr multilayers are characterized by GXIR, AFM, XRD, and TEM. At 250 °C, the width of Zr-on-Al interlayer is thicker than that of Al-on-Zr interlayer, which presents the first structural modification in the multilayers. At 295 °C for Al(pure)/Zr and 298 °C for Al(1wt.-%Si)/Zr, the crystal size of Al(111) has the lowest value, and the changing trend of the crystal size is consistent with the situation in AFM measurements. At those temperatures, the reactions appear between the Al and Zr layers in two systems, where the interface consists of amorphous Al-Zr alloy transforms to polycrystalline Al-Zr alloy. Therefore, in our experiment, it can be concluded that Si doped in Al, even in a small proportion, cannot only change the interfacial structure and increase the EUV reflectance, but also influence the reaction temperature in the multilayers, which is considered to be useful for further practical experimental applications.

This work was supported by National Natural Science Foundation of China under Grant No. 11027507.

References

1. A. J. Corso, P. Zuppella, P. Nicolosi, D. L. Windt, E. Gullikson, and M. G. Pelizzo, Opt. Express **19**, 13963 (2011).
2. S. Bajt, J. B. Alameda, T. W. Barbee, Jr.,W. M. Clift, J. A. Folta, B. Kaufmann, and E. A. Spiller, Opt. Eng. **41**, 1797 (2002).
3. E. Meltchakov, C. Hecquet, M. Roulliay, S. D. Rossi, Y. Menesguen, A. Jérome, F. Bridou, F. Varniere, M.-F. Ravet-Krill, and F. Delmottel, Appl. Phys. A **98**, 111 (2010).
4. D. L. Voronov, E. H. Anderson, R. Cambie, S. Cabrini, S. D. Dhuey, L. I. Goray, E. M. Gullikson, F. Salmassi, T. Warwick, V. V. Yashchuk, and H. A. Padmore, Opt. Express **19**, 6320 (2011).
5. P. Jonnard, K. Le Guen, M.-H. Hu, J.-M. André, E. Meltchakov, C. Hecquet, F. Delmotte, and A. Galtayries, Proc. SPIE **7360**, 73600O (1997).
6. D. L. Voronov, E. H. Anderson, R. Cambie, E. M. Gullikson, F. Salmassi, T. Warwick, V. V. Yashchuk, and H. A. Padmore, Proc. SPIE **8139**, 81390B (2011).
7. Q. Zhong, W. Li, Z. Zhang, J. Zhu, Q. Huang, C. Yang, Z. Wang, P. Jonnard, K. Le Guen, J.-M. André, H. Zhou, and T. Huo, Opt. Express **20**, 10692 (2012).
8. Q. Zhong, Z. Zhang, J. Zhu, Z. Wang, P. Jonnard, K. Le Guen, and J.-M. André, Appl. Sur. Sci. **259**, 371 (2012).
9. Q. Zhong, Z. Zhang, J. Zhu, Z. Wang, P. Jonnard, K. Le Guen, Y. Yuan, J.-M. André, H. Zhou, and T. Huo, Appl. Phys. A **109**, 133 (2012).
10. M. Wormington, C. Panaccione, K. Matney, and D. Bowen, Phil. Trans. R. Soc. Lond. A **357**, 2827 (1999).
11. S. Naseer, F. U. Khan, N. U. Rehman, A. Qayyum, F. Rahman, and M. Zakaullah, Eur. Phys. J. Appl. Phys. **49**, 21001 (2010).
12. K. J. Blobaum, T. P. Weihs, T. W. Barbee, Jr., and M. A. Wall, UCRL J C–118965 (1995).

Appl Phys A (2012) 109:133–138
DOI 10.1007/s00339-012-7085-1

Applied Physics A
Materials Science & Processing

The thermal stability of Al(1%wtSi)/Zr EUV mirrors

Qi Zhong · Zhong Zhang · Jingtao Zhu ·
Zhanshan Wang · Philippe Jonnard · Karine Le Guen ·
Yanyan Yuan · Jean-Michel André · Hongjun Zhou ·
Tonglin Huo

Received: 1 July 2012 / Accepted: 17 July 2012 / Published online: 3 August 2012

Abstract Six Al(1%wtSi)/Zr multilayers are deposited on Si substrates by using the direct-current magnetron sputtering system, and annealed from 100 °C to 500 °C temperature in a vacuum furnace for 1 h. To evaluate the thermal stability of Al(1%wtSi)/Zr multilayers, the multilayers were characterized by grazing incidence X-ray reflectance, X-ray diffraction, X-ray emission spectroscopy, and near-normal incident extreme ultraviolet (EUV) reflection. The symmetric and asymmetric interlayer models are used to present the interfacial structure before and after 300 °C. The Al(1%wtSi)/Zr multilayer annealed up to 200 °C maintains the initial symmetric multilayer structure, and keeps almost the similar EUV reflectivity as the nonannealed sample. From 300 °C, interdiffusion is much greater at the Zr/Al interface compared with the Al/Zr interface. And the interfacial phases of Al-Zr alloy transform from amorphous to polycrystalline, which induces the deterioration of multilayer structure and the decrease of EUV reflectivity. However, up to 500 °C, the polycrystalline Al-Zr compound does not destroy the multilayer completely.

1 Introduction

Al-based multilayers for extreme ultra violet (EUV) and soft X-ray optics have been researched for a few years [1–9]. For the Al/Zr multilayer, the highest reflectivity in the Al-based multilayer makes it especially attractive for the EUV applications [1, 6–9]. In our recent papers [6, 7], the Al(1%wtSi)/Zr multilayer has shown very promising optical and structural performance in the wavelength range of $\lambda \sim 17$–19 nm. Based on the analysis of Al(1.0%wtSi)/Zr multilayers with the different number of periods, we could determine that the interfacial roughness was small for the first 40 periods toward the substrate, but increased with the period number larger than 40. However, the optical performance of Al(1.0%wtSi)/Zr with 40 periods was hampered by the variable interfacial structure. Its experimental peak reflectivity was 41.2 % at 5° incidence angle, which was much lower than corresponding theoretical value of 70.9 %. X-ray diffraction (XRD) and X-ray photoelectron spectroscopy (XPS) revealed that the large differences between the theoretical and experimental reflectivity were due to four impact factors: inhomogeneous crystallization of aluminum, contamination of the multilayer, surface oxidized layer, and interdiffusion between Al and Zr layers. In addition to high reflectivity, some practical applications, for example, the solar satellite instruments in space [10–12], require thermal stability of coatings at elevated temperatures larger than 100 °C. However, the thermal stability of Al(1%wtSi)/Zr multilayer has not been evaluated yet.

In this paper, we describe the thermal stability of the Al(1%wtSi)/Zr multilayers deposited on Si substrates for the purpose of coating the multilayer on normal-incidence telescopes tuned to specific emission lines (i.e., Fe-IX ($\lambda = 17.1$ nm), Fe-XI ($\lambda = 18.0$ nm), and Fe-XII ($\lambda = 19.3$ nm)) in the wavelength range of $\lambda \sim 17$–19 nm. The optical and

---

Q. Zhong · Z. Zhang (✉) · J. Zhu · Z. Wang
MOE Key Laboratory of Advanced Micro-Structured Materials, Institute of Precision Optical Engineering, Department of Physics, Tongji University, Shanghai 200092, China
e-mail: zhangzhongcc@tongji.edu.cn
Fax: +86-021-65984652

P. Jonnard · K. Le Guen · Y. Yuan · J.-M. André
Laboratoire de Chimie Physique—Matière Rayonnement, UPMC Univ Paris 06, CNRS UMR 7614, 11 rue Pierre et Marie Curie, 75231 Paris cedex 05, France

H. Zhou · T. Huo
National Synchrotron Radiation Laboratory, University of Science and Technology of China, Hefei 230029, China

Table 1 Periodic length, 1st Bragg peak reflectivity and gamma value of the Al(1%wtSi)/Zr multilayer samples derived from the GIXR measurements

Sample No.		1	2	3	4	5	6
Annealing temperature (°C)		RT	100	200	300	400	500
Periodic length (D, nm)	Before annealing	9.32	9.33	9.35	9.32	9.30	9.32
	After annealing	–	9.31	9.32	9.24	9.14	9.14
1st Bragg peak reflectivity (%)	Before annealing	66.0	66.5	67.0	65.8	67.5	66.0
	After annealing	–	67.0	58.9	47.0	40.4	26.6
Gamma, d_{Zr}/D	Before annealing	0.352	0.349	0.350	0.350	0.352	0.350
	After annealing	–	0.344	0.336	0.325	0.296	0.263

structural performances of the room temperature (RT) multilayer sample and annealed samples were characterized by grazing incidence X-ray reflectance (GIXR) and near-normal incident EUV reflection quantitatively. Also, the qualitative structural changes were investigated by X-ray emission spectroscopy (XES) and XRD.

2 Experimental methods

Six Al(1%wtSi)/Zr multilayer samples consisting of 40 bilayers, with the periodic thickness of 9.32 nm, are designed to have a near normal incidence reflectivity around 18.5 nm. They were prepared by using the direct-current magnetron sputtering system [6, 7, 13, 14]. Before deposition, the base pressure was 8.0×10^{-5} Pa, and the samples were deposited on Si polished wafers under a 0.18 Pa argon (99.9999 % purity) pressure. The sputtering targets with diameter of 100 mm were zirconium (99.5 %) and silicon doped in aluminum (Al(1%wtSi)).

To evaluate the thermal stability of Al(1%wtSi)/Zr multilayers, the five multilayer samples, shown as Nos. 2–6 in Table 1, except for RT sample No. 1, were annealed at temperatures of 100, 200, 300, 400, and 500 °C in a vacuum furnace for 1 h, respectively. After annealing, the samples were cooled to room temperature naturally in the furnace with a base pressure of 3.0×10^{-4} Pa.

The GIXR measurements shown in Table 1 were carried out to test the changes in the multilayers before and after annealing, using an X-ray diffractometer working at the Cu K_α line (0.154 nm). The fitting calculations of GIXR curves were performed with Bede Refs software (genetic algorithm) to determine individual layer thickness and interface roughness [15].

The XRD measurements provide identification of crystalline phases present in the modified layer along with structural changes during the annealing temperatures. The electron-induced XES measurements were performed by using a high spectral resolution wavelength dispersive spectrometer. We have analyzed the Al K_β emission (3p–1s transition) that describes the occupied valence states having a Al 3p character. These states are very sensitive to the chemical state of the Al atoms. The excitation of the Al/Zr samples was done by using electrons having a 8 keV energy, except the RT sample analyzed with 6 keV electrons. In these conditions the whole stack is analyzed.

The EUV reflectivity measurements were made at a 5° incident angle, using the reflectometer at the Spectral Radiation Standard and Metrology Beamline and Station (beamline U26) at the National Synchrotron Radiation Laboratory in Hefei, China.

3 Results and discussion

In the previous paper, we found that the Al(1%wtSi)/Zr multilayer had a variable interfacial structure based on the analyses of transmission electron microscope images [6]. Owing to the large interdiffusion between Al and Zr layers, the four layer model could better represent the variable multilayer structure than the two layer model for 40 periods [7].

Therefore, to estimate the initial structure of the multilayers, we carried out the four layer model with a 2.4 nm $ZrO_{1.5}$ capping layer on the samples. We first use the four layer symmetric model to fit the GIXR measurements shown in Fig. 1(a). The thickness and composition of the interlayers (Al-on-Zr and Zr-on-Al) are the same in the model. The fitting data matches well with the experiments for the sample before annealing at 300 °C, while the quality of fit is not good for the sample from 300 °C annealing, especially for the regions between the Bragg peaks. So we try to fit the experimental results assuming the four layer asymmetric model (Fig. 1(b)). In the model of two different thickness interlayers, the thickness of Zr-on-Al at the Zr/Al interface is larger than that of Al-on-Zr at the Al/Zr interface, because Zr diffuses and reacts more rapidly with Al than Al diffuses and reacts with Zr after 300 °C [16]. However, the situation of fitting data in asymmetric interlayer model is opposite to

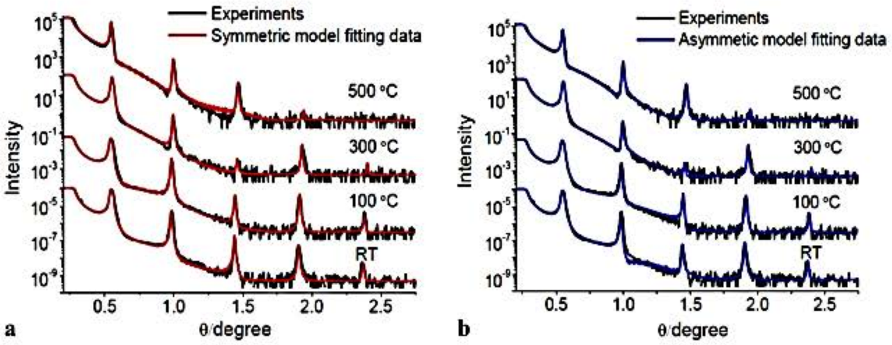

Fig. 1 Comparison between the GIXR experimental and fitted curves with the symmetric interlayer model (**a**) and the asymmetric interlayer model (**b**) for the RT, 100, 300, 500 °C samples

Table 2 Parameters deduced from the fit of four sample curves using different models derived from Fig. 1

Sample Al(1%wtSi)/Zr	Layers	Thickness /nm	Roughness /nm
Symmetric interlayer model			
RT	Al-on-Zr	1.5	0.5
	Zr	1.78	1.4
	Zr-on-Al	1.5	0.6
	Al(1%wtSi)	4.6	0.95
Annealed 100 °C	Al-on-Zr	1.5	0.45
	Zr	1.7	0.6
	Zr-on-Al	1.5	0.5
	Al(1%wtSi)	4.6	0.84
Asymmetric interlayer model			
Annealed 300 °C	Al-on-Zr	2.0	0.89
	Zr	1.0	0.63
	Zr-on-Al	2.5	0.9
	Al(1%wtSi)	3.75	0.96
Annealed 500 °C	Al-on-Zr	2.2	2.17
	Zr	0.2	0.1
	Zr-on-Al	3.3	1.1
	Al(1%wtSi)	3.45	1.01

that of symmetric interlayer model. The fitting data is good for measurements after annealed at 300 °C, but the quality of fitted data is not very satisfactory for the region between the 2nd and 3rd Bragg peaks before annealed at 300 °C. Those two situations in different models may be due to different formation of Al-Zr alloy and interlayers at Al/Zr and Zr/Al interfaces during the annealing process. Therefore, we use the symmetric interlayer model and asymmetric interlayer model to present the multilayer structure before and from 300 °C, respectively. The estimated thicknesses and roughness of the Al, Zr layers and interlayers are listed in Table 2. With the symmetric interlayer model, the most noticeable feature is the decrease of the interfacial roughness and the increase of the 1st Bragg reflectivity at 100 °C annealing temperature. For the asymmetric interlayer model, the roughness of all layers, expect for Zr layer, increases with the temperature. If we remove the Zr layer at 500 °C, the fitting line cannot match the regions between the different Bragg peaks in the measurement (the fitting curve is not shown in Fig. 1). Therefore, we can assume the Zr material still exists in the multilayer at high temperature, even if its content is very small. This may be caused by the thickness of the Al layer decreasing more rapidly than the Zr layer, and Zr diffuses and reacts more rapidly with Al than Al diffuses and reacts with Zr [16]. However, the periodic structure at 500 °C is not destroyed completely by the interdiffusion between the Al and Zr layers.

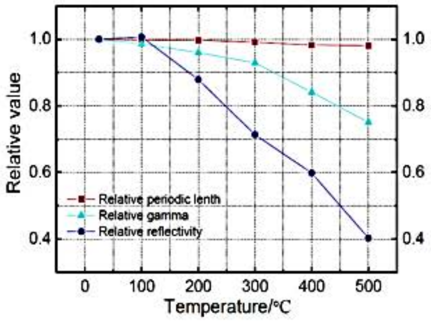

Fig. 2 Relative periodic length, relative gamma value and relative 1st Bragg of peak reflectivity of the Al/Zr multilayer samples (*color curve*) as a function of annealing temperature. The periodic lengths (*red curve*), gamma values (*light blue curve*) and the peak reflectivities (*dark blue curve*) were normalized by those of the samples before annealing

To evaluate the thermal stability of the Al(1%wtSi)/Zr multilayers, the changes in the periodic length, gamma and the 1st Bragg peak reflectivity of the annealed multilayer samples are derived from GIXR measurements (Fig. 1). Gamma is the ratio of the Zr thickness to the period. In Fig. 2, the periodic length, gamma and the 1st order Bragg peak reflectivity of each multilayer sample are normalized by those at the RT conditions. The periodic length of the multilayer slightly decreases with the annealing temperature. The relative change in the periodic length of the mul-

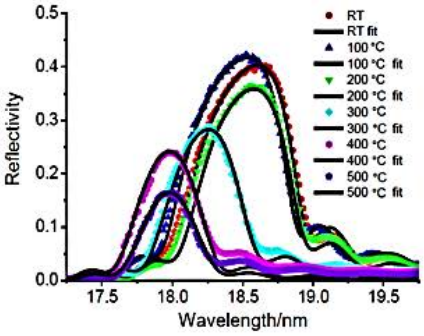

Fig. 3 Measured reflectivity versus wavelength of the multilayers at 5° incident angle by synchrotron radiation. The *fitting lines* use the models in Table 2

tilayer annealed at 200 °C is about 0.3 %. From 300 °C, it increases to 0.9 %, and up to 500 °C the change is about 1.9 %. For the 1st order Bragg peak reflectivity, it first increases at 100 °C and decreases remarkably to 500 °C to 41 % of the initial value. Regarding the gamma value, it also shows a decreasing trend during the annealing process. The relative gamma value has an obvious turning point at 300 °C, consistent with the different GIXR simulation models in Table 2.

In order to verify the GIXR results shown in Table 2 and Fig. 2, the multilayers are tested and fitted in the wavelength region of 17 nm–19 nm. The measurements are shown in Fig. 3. They are best fitted by using the same parameters and models mentioned from the GIXR fitting data. The measured EUV reflectivity curves of the samples change with annealing temperature. The reflectivity of the RT sample is 40.4 %, increased to 41.7 % at 100 °C, and then down to 16.2 % at 500 °C, values which are consistent with the changes of 1st order Bragg peak reflectivity in GIXR. Before 300 °C, the peak positions of different annealing samples are around 18.5 nm. At 300 °C, the peak position moves to 18.3 nm, but after 300 °C it is largely shifted, down to 17.9 nm at 500 °C. Because the similar thickness of different samples before annealing, the different peak positions before 300 °C are due to the different thicknesses of initial samples, but from 300 °C mainly caused by the annealing process.

To identify the annealing effect for the multilayer structures, the XES and XRD measurements are carried out. Figure 4 shows Al K_β emission bands of different Al(1%wtSi)/Zr multilayer samples with the two reference samples: Al pure metal and $ZrAl_3$ powder (99.95 % purity). The emission band of Al(1.0%wtSi) is identical to that of pure Al, because the low Si concentration does not disturb the Al electronic structure in the Al(1.0%wtSi) material [2, 17]. There exists various compounds in the Al-Zr diagram but only $ZrAl_3$ is commercially available. The spectra of the samples non-annealed and annealed at 100 and 200 °C are the same. The samples from 300 °C also show the same spectra. Thus, we only present the RT and 500 °C sample spectra in Fig. 4. It is observed that the spectra of the multilayers are different from the one of Al, which should be observed if no interaction takes place between the Al and Zr layers. Indeed, with respect to the metal, both multilayers present a narrower spectrum with a maximum shifted toward the low photon energies. The multilayer spectra are closer to the aluminide spectrum giving evidence of the existence of some interfacial compound resulting from an interdiffusion between the Al and Zr layers. However, we cannot assert that the $ZrAl_3$ compound is present in the multilayer because we do not know the spectra from the other aluminides: Zr_3Al, Zr_2Al, Zr_5Al_3, Zr_3Al_2, Zr_4Al_3, Zr_5Al_4, ZrAl, Zr_2Al_3, and $ZrAl_2$. We see that the spectra of the non-annealed and annealed at 200 °C samples are closer to the pure Al spectrum than spectra of the multilayers annealed between 300 and 500 °C. This shows that the content of pure Al is higher in the low temperature samples and that after a critical annealing temperature between 200 and 300 °C this content decreases as probably the interfacial composition.

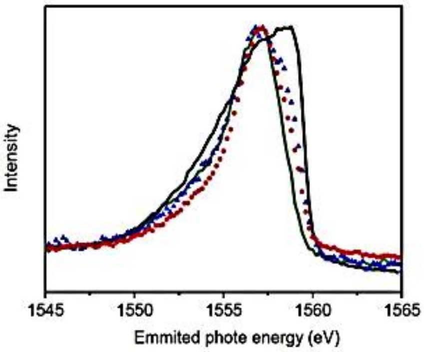

Fig. 4 Al K_β emission bands of Al(1%wtSi)/Zr annealed non-annealed (*blue triangles*) and annealed at 500 °C (*red dots*) and comparison to the reference spectra of pure Al (*black curve*) and $ZrAl_3$ (*green curve*)

As shown in Fig. 5, different XRD patterns are observed for different annealed samples. Considering the Scherrer formula [7], the crystal orientations, peak positions (2-theta) and grain sizes of the samples are presented in Table 3. Before 300 °C, The XRD pattern of the samples (RT, 100 °C, 200 °C) contains three main peaks: 38.7° (Al⟨111⟩), 35.3° (Zr⟨002⟩), and 36.5° (Zr⟨101⟩). For the Al⟨111⟩ during the annealing temperature from RT to 200 °C, the crystal size increases from 6.1 to 6.2 nm. Because of the large crystal size, the interfacial roughness could also increase [1, 7]. However, for the Zr planes, the crystal size of Zr⟨101⟩ just decreases with the annealing temperature, but that of Zr⟨002⟩ first increases at 100 °C, and then decrease when annealed at 200 °C. Based on the analysis of EUV and GIXR measurements for 100 °C sample, we found that the crystallization of Zr could decrease the interfacial roughness

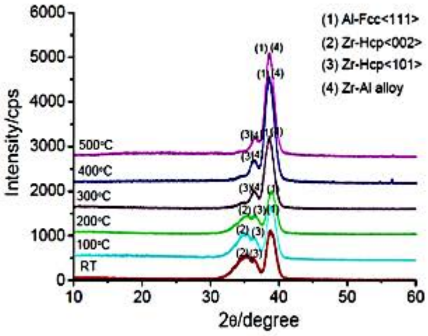

Fig. 5 Diffraction curves of the samples of Al(1%wtSi)/Zr (*color lines*) with different annealed temperatures (RT, 100 °C, 200 °C, 300 °C, 400 °C, and 500 °C)

Table 3 Crystal orientations, 2-theta and grain sizes of different annealing temperature samples as derived from Fig. 5

Sample	Crystal orientation	2Theta (°)	Crystal size /nm
RT	Al⟨111⟩	38.7	6.1
	Zr⟨002⟩	35.3	4.2
	Zr⟨101⟩	36.5	8.7
100 °C	Al⟨111⟩	38.7	6.2
	Zr⟨002⟩	35.3	4.4
	Zr⟨101⟩	36.5	7.7
200 °C	Al⟨111⟩	38.7	6.2
	Zr⟨002⟩	35.3	4.3
	Zr⟨101⟩	36.5	7.1
300 °C	Al⟨111⟩/Al-Zr alloy	38.6	6.4
	Zr⟨101⟩/Al-Zr alloy	36.4	9.3
400 °C	Al⟨111⟩/Al-Zr alloy	38.5	6.4
	Zr⟨101⟩/Al-Zr alloy	36.3	9.5
500 °C	Al⟨111⟩/Al-Zr alloy	38.5	6.5
	Zr⟨101⟩/Al-Zr alloy	36.3	9.7

and increase the EUV reflectivity in the multilayer. From 300 °C, all main peaks are changed. The Zr⟨002⟩ peak almost disappears in the patterns, but still has a small contribution at 35.3°. Thus, we can conclude the Zr material still exists at 500 °C. The peak positions of Al⟨111⟩ and Zr⟨101⟩ are shifted by 0.2° at 500 °C meaning that there is a new polycrystalline Al-Zr alloy compound formed at the interface. The phases of polycrystalline Al-Zr alloy could be about the similar positions as Al⟨111⟩ and Zr⟨101⟩, which shift the peak positions in Fig. 5. In our previous paper [7], we found that the interlayers of RT sample consisted of an amorphous Al-Zr alloy in the multilayer. Considering the results in the XES (Fig. 4), it seems that up to 200 °C the multilayer consist of alternating layers of polycrystalline Al and Zr layers and interfacial amorphous layers of Al-Zr alloy. The amorphous Al-Zr alloy grows into Al and Zr layers with the increasing annealing temperature. However, from 300 °C, the amorphous Al-Zr alloy is transformed to polycrystalline Al-Zr alloy. This structural change of the multilayer between 200 and 300 °C should be the main reason for the deterioration of the multilayer structure in GIXR measurements (Table 2 and Fig. 2) and the decrease of EUV reflectivity (Fig. 3). It can be concluded that the new polycrystalline Al-Zr compounds degrades the optical contrast of the multilayer structure, and increases the interfacial roughness.

4 Conclusion

To evaluate the thermal stability of Al(1%wtSi)/Zr multilayer, we deposited six samples, and annealed them in a vacuum furnace for 1 h. Based on the analyses of GIXR and EUV, the symmetric and asymmetric interlayer models can be best fitted the multilayer structure before and after 300 °C. The multilayer samples annealed up to 100 °C, show higher peak reflectivities both in GIXR and EUV reflectivity than the RT sample. The degradation of the multilayer structure does not occur before 300 °C. However, from 300 °C, the amorphous Al-Zr alloy has transformed to the polycrystalline Al-Zr alloy in the interface, which decreases the EUV reflectivity and increases the interdiffusion between the Al and Zr layers. The periodic structure of the Al(1%wtSi)/Zr multilayer annealed at 500 °C is not destroyed completely by the new formed compounds in the interfaces. Therefore, in our experiment, it can be concluded that the Al(1%wtSi)/Zr multilayer has a stable structure and performance up to 200 °C, which is considered to be useful for further practical experimental applications.

Acknowledgements This work is supported by National Basic Research Program of China (No. 2011CB922203) and National Natural Science Foundation of China (Nos. 10825521, 11061130549).

References

1. D.L. Windt, J.A. Bellotti, Appl. Opt. **48**, 4932 (2009)
2. P. Jonnard, K. Le Guen, M.-H. Hu, J.-M. André, E. Meltchakov, C. Hecquet, F. Delmotte, A. Galtayries, Proc. SPIE **7360**, 73600O (2009)
3. E. Meltchakov, C. Hecquet, M. Roulliay, S.D. Rossi, Y. Menesguen, A. Jérome, F. Bridou, F. Varniere, M.-F. Ravet-Krill, F. Delmottel, Appl. Phys. A **98**, 111 (2010)
4. M.-H. Hu, K. Le Guen, J.-M. André, P. Jonnard, E. Meltchakov, F. Delmotte, A. Galtayries, Opt. Express **18**, 20019 (2010)
5. E. Meltchakov, A. Ziani, F. Auchere, X. Zhang, M. Roulliay, S. De Rossi, Ch. Bourassin-Bouchet, A. Jérome, F. Bridou, F. Varniere, F. Delmotte, Proc. SPIE **8168**, 816819 (2011)

---

6. Q. Zhong, W. Li, Z. Zhang, J. Zhu, Q. Huang, C. Yang, Z. Wang, P. Jonnard, K. Le Guen, J.-M. André, H. Zhou, T. Huo, Opt. Express **20**, 10692 (2012)
7. Q. Zhong, Z. Zhang, J. Zhu, Z. Wang, P. Jonnard, K. Le Guen, J.-M. André, Appl. Sur. Sci. (2012) (submit). http://hal.archives-ouvertes.fr/hal-00697730
8. D.L. Voronov, E.H. Anderson, R. Cambie, S. Cabrini, S.D. Dhuey, L.I. Goray, E.M. Gullikson, F. Salmassi, T. Warwick, V.V. Yashchuk, H.A. Padmore, Opt. Express **19**, 6320 (2011)
9. D.L. Voronov, E.H. Anderson, R. Cambie, E.M. Gullikson, F. Salmassi, T. Warwick, V.V. Yashchuk, H.A. Padmore, Proc. SPIE **8139**, 81390B (2011)
10. D.L. Windt, S. Donguy, J. Seely, B. Kjornrattanawanich, E.M. Gullikson, C.C. Walton, L. Golub, E. DeLuca, Proc. SPIE **5168**, 1 (2004)
11. D.L. Windt, S. Donguy, J. Seely, B. Kjornrattanawanich, Appl. Opt. **43**, 1835 (2004)
12. M.F. Ravet, F. Bridou, X. Zhang-Song, A. Jerome, F. Delmotte, R. Mercier, M. Bougnet, P. Bouyries, J.P. DelaboudiniËre, Proc. SPIE **5250**, 99 (2004)
13. F. Wang, Z. Wang, Z. Zhang, W. Wu, H. Wang, S. Zhang, S. Qin, L. Chen, Opt. Precis. Eng. **13**, 28 (2005) (in Chinese)
14. Y. Xu, Z. Wang, J. Xu, Z. Zhang, H. Wang, J. Zhu, F. Wang, B. Wang, S. Qin, L. Chen, Opt. Precis. Eng. **15**, 1838 (2007)
15. M. Wormington, C. Panaccione, K. Matney, D. Bowen, Philos. Trans. R. Soc. Lond. A **357**, 2827 (1999)
16. K.J. Blobaum, T.P. Weihs, T.W. Barbee Jr., M.A. Wall, UCRL J C-118965 (1995)
17. P. Jonnard, K. Le Guen, R. Gauvin, J.-F. Le Berre, Microsc. Microanal. **15**, 36 (2009)

Caracterisation de l'environnement physico-chimique de miroirs multicouches à base de cobalt travaillant dans les domaines des rayons X mous et de l'extrême ultraviolet

Résumé:

Dans ce travail, nous nous concentrons sur la caractérisation de l'environnement physico-chimique des éléments présents dans des multicouches à base de cobalt qui travaillent dans les domaines des rayons X mous et extrême ultra-violet (EUV). L'observation des modifications des interface des deux systèmes Co/Mo_2C et Co/Mo_2C/Y lors du recuit est important pour l'amélioration de leurs performance optique. Ils ont été étudiés en combinant des méthodes non destructives, spectroscopie d'émission des rayons X, résonance magnétique nucléaire, réflectométrie de rayons X et des méthodes destructrices, spectrrométrie de masse d'ions secondaires par temps de vol et la Microscopie électronique en transmission pour étudier leurs propriétés interfaciales. Ce travail vise non seulement à la conception et la fabrication de nouveaux éléments optiques pour faire face au développement des sources et des applications dans les demaines des rayons X mous et l'EUV, mais aussi à développer une méthodologie combinant des simulations et des expérimentations consacrée à l'analyse des interfaces dans structures multicouches afin d'améliorer leur propriétés optiques.

Mots clés : multicouches à base de cobalt, Optique des rayons X et extrême ultraviolet, Réflectométrie des rayons X (XRR), Spectroscopie d'Emission-X (XES), interfaces, diffusion, Spectroscopie de Résonance Magnétique Nucléaire (RMN), Spectrrométrie de Masse d'Ions Secondaires par Temps de Vol (ToF-SIMS), Microscopie Electronique en Transmission (TEM).

Characterization of physico-chemical environment of Co-based multilayers mirrors working in the soft x-ray and EUV ranges

Abstract:

In this work, we focus on the characterization of physico-chemical environment of the element present in Co-based multilayers working in the soft x-ray and EUV ranges. The observation of interface changes of both systems Co/Mo_2C and Co/Mo_2C/Y upon annealing is important for improving their optical performance. They were studied by combining non-destructive methods, x-ray emission spectroscopy, nuclear magnetic resonance spectroscopy, x-ray reflectometry and destructive methods, time-of-flight secondary ions mass spectroscopy and transmission electron microscopy to investigate their interface properties. This work aims not only at designing and fabricating new optical elements to face the development of sources and applications in the EUV and soft x-ray ranges, but also at developing a methodology combining simulations and experiments devoted to the interface analysis in these multilayer structures in order to improve their optical properties.

Keywords: Co-based multilayer, x-rays and EUV optics, X-ray Reflectometry (XRR), X-ray Emission Spectroscopy(XES), interfaces, diffusion, Nuclear Magnetic Resonance spectroscopy (NMR), Time-of-Flight Secondary Ion Mass Spectroscopy (ToF-SIMS), Transmission electron spectroscopy (TEM).